2026 | Faculty of Engineering Technology

Doctoral dissertation submitted to obtain the degree of
Doctor of Engineering Technology, to be defended by

Geelen Stef

DOCTORAL DISSERTATION

Improving Radiological Monitoring Using Drones

Promoter: Prof. Dr Schroeyers Wouter | UHasselt

Co-promoter: Prof. Dr Camps Johan | UHasselt & SCK CEN

2026 | Faculty of Engineering Technology.

UHASSELT
KNOWLEDGE IN ACTION

Doctoral dissertation submitted to obtain the degree of
Doctor of Engineering Technology, to be defended by

Geelen Stef

DOCTORAL DISSERTATION

Improving Radiological Monitoring Using Drones

Promoter: Prof. Dr Schroeyers Wouter | UHasselt

Co-promoter: Prof. Dr Camps Johan | UHasselt & SCK CEN

2026

Uitgevoerd in samenwerking met SCK CEN

The PhD researcher and the UHasselt supervisor hereby formally declare that the research conducted for the purpose of this PhD thesis was executed in accordance with the principles of good scientific conduct, as stipulated in the UHasselt Integrity charter, the UHasselt charter supervisor – PhD Researcher, the UHasselt Integrity Policy and the UHasselt guidelines for the use of (generative) AI in research.

The author asserts that this PhD thesis is made Open Access immediately upon submission. The full text is publicly available without restrictions.

Dankwoord

Mijn promotoren en mentoren, prof. dr. Wouter Schroeyers, prof. dr. Johan Camps, dr. Tim Vidmar en dr. Geert Olyslaegers, zijn in deze thesis van onschatbare waarde geweest. Ze hebben mijn methodes keer op keer nagekeken en zijn mij zonder probleem blijven begeleiden zelfs nadat mijn contract was afgelopen. Ze hebben me altijd bijgestaan met hun expertise en ik hoop dat ik er iets van heb mogen overnemen. Dus dank u wel voor jullie steun en jullie vertrouwen. Ik wil Geert ook nog specifiek bedanken als piloot, want zonder hem waren veel van deze metingen minder goed of zelfs niet gelukt.

Mijn collega's op het SCK CEN en Universiteit Hasselt waren ontzettend belangrijk. Ze zorgden 's avonds voor de nodige afleiding en hebben mij meermaals geholpen op momenten dat ik vast kwam te zitten, zowel mentaal als praktisch. Jens-Peter en Stijn, merci voor de fijne momenten, de hulp bij metingen in het veld en de whiteboard brainstorms. Lowie, Mattias en Linde, merci voor de leuke momenten en om het bureau op UHasselt zo fijn te maken. Johan Paridaens, bedankt voor alle hulp en het gebruik van de RadDetecTIF, dit heeft veel geholpen in deze thesis. Hasan, thank you for your help and support with Penelope. Fabrizio, thank you for the improvements to my code and the ideas for the directional detector. I enjoyed our brief but fruitful cooperation.

De mensen bij SABCA hebben mij ook enorm geholpen bij de creatie van de prototypes van de detectorsystemen. Hun kennis en skills zijn van groot belang geweest in het realiseren van de projecten. Dank u voor alle meetcampagnes en de onvergetelijke momenten. Daarnaast wil ik de mensen van de civiele bescherming ook bedanken voor de terbeschikkingstelling van hun drones en hulp bij de meetcampagnes.

Ik ben beginnen werken bij Mirion Technologies Olen na mijn doctoraatscontract en dit was tegelijkertijd de beste en slechtste beslissing die ik heb gemaakt. De combinatie van werken met het schrijven van een thesis kan ik elke doctoraatsstudent afraden. Maar als je het toch wil doen raad ik zo goede collega's als die van mij aan. Ze hebben mij gesteund en zijn enorm flexibel geweest.

Als laatste wil ik zeker ook mijn familie bedanken. Ze hebben mij enorm gesteund over het hele traject. Ze hebben mij ook telkens weer gemotiveerd om door te blijven gaan. Zonder hun had deze thesis waarschijnlijk niet afgeraakt. Mijn mama en papa moeten ook nog speciaal worden bedankt. Ze stonden telkens klaar voor mij in alle situaties en hebben mij, met heel veel geduld, geholpen dit traject tot een goed einde te brengen.

Content

List with Figures

List with Tables

List with Abbreviations

Abbreviation	Meaning
AC	Alternating Current
AGL	Above Ground Level
ALARA	As Low As Reasonably Achievable
AMSL	Above Mean Sea Level
BGO	Scintillation detector material: Bismuth Germanium Oxide
bMCA	Brightspec Multi Channel Analyzer
BR1	Belgian Reactor 1
BUDDAWAK	Belgian Unmanned aerial systems for Decommissioning, Detection and AWAreness of radioactive risK
BVLOS	Beyond Visual Line Of Sight
CBRN	Chemical, Biological, Radiological and Nuclear
CeBr	Scintillation detector material: Cerium Bromide
CPE	Charged Particle Equilibrium
CsI	Scintillation detector material: Caesium Iodide
CZT	Semiconductor detector material Cadmium Zinc Telluride
DC	Direct Current
DR	Dose Rate
FANC	Federaal Agentschap voor Nucleaire Controle
FDNPP	Fukushima Daiichi Nuclear Power Plant
FEP	Full Energy Peak
FL160	Flight Level 16000 feet
FW	Fixed-wing
GMT	Greenwich Mean Time
GNSS	Global Navigation Satellite System
GPS	Global Positioning System
HPGe	Semiconductor detector material: High Purity Germanium
IAEA	International Atomic Energy Agency
ICRP	International Commission on Radiological Protection
ICRU	International Commission on Radiation Units and Measurements
IDE	Integrated Development Environment
LaBr	Scintillation detector material: Lanthanum Bromide
LIDAR	Laser Imaging Detection And Ranging
LUC	Light UAS operator certificate
MC	Monte Carlo

MCA	Multi Channel Analyzer
MTOW	Maximum Take Off Weight
NaI	Scintillation detector material: Sodium Iodide
NIST	National Institute of Standards and Technology
NORM	Naturally Occurring Radioactive Materials
PENELOPE	Penetration and ENErgy LOss of Positrons and Electrons
PMT	Photo Multiplier Tube
PPE	Personal Protective Equipment
PVT	Scintillation detector material: Poly Vinyl Toluene
QGIS	Quantum Geographic Information System
RadDetecTIF	Radiation Detection & Transmission In Flight
SCK CEN	Studie Centrum voor Kernenergie, Centre d'Etude de l'énergie Nucléaire
SDK	Software Development Kit
SiPM	Silicon Photo Multiplier
SORA	Specific Operation Risk Assessment
UAV	Unmanned Aerial Vehicle
UGV	Unmanned Ground Vehicle
UHasselt	Universiteit Hasselt
UMTRAP	Uranium Mill Tailings Remedial Action Project
UTC	Coordinated Universal Time
VLOS	Visual Line Of Sight
VSC	Vlaams Supercomputer Centrum

1 Introduction

The overall target of this thesis is to investigate how drones can be used as a tool in radiological and nuclear monitoring through computer simulations, controlled measurement scenarios as well as measurements in the field.

Unmanned aerial systems (UAS) or Unmanned aerial vehicles (UAV, commonly known as drones) are becoming increasingly more common in civil domains, industry and emergency scenarios. They can be used in combination with different payloads to allow the use of a variety of use cases. In agriculture UAVs can be used to spray insecticide or monitor crop-growth [1], [2]. In the entertainment sector they are used for videography and photography. One of the most impressive UAVs for videography is used in Formula-1 racing and can reach speeds of 350 km/h [3]. For emergency situations drones can play a key part. They can quickly create an overview of a situation and can relay that information live to the first responders. Using normal cameras, thermal cameras, night vision cameras or spotlights already have their place in search and rescue and putting out fires by the civil protection or fire fighters [4]. Inspection of structures, such as windmills or power pylons, is also done with UAVs [5]. This is a significantly cheaper and safer choice than using a helicopter.

Transportation using drones or UAVs is a relatively new field as it requires multiple drones to operate autonomously. An added difficulty is that they have to fly over urban areas which adds to the risk of damaging property or injuring persons. Corporations such as Amazon are already using UAVs as delivery method in the United States [6]. In medical transportation UAVs can be used to transport medical equipment, organs or radioactive sources for nuclear medicine, however, this requires strict regulations [7].

In CBRN emergencies (Chemical, Biological, Radiological and Nuclear emergencies) UAVs can be an additional tool for first responders. UAVs allow first responders to remain safe while obtaining a first overview of the site. In radiological and nuclear scenarios specifically, it is possible to measure the radiation without direct sampling because of the emitted radiation. This will also be the main focus of this thesis. Currently, aerial monitoring for radiological and nuclear emergencies are mostly done with small planes and helicopters [8-12]. UAVs can improve aerial monitoring as they can fly at lower heights which improves the efficiency and spatial resolution significantly.

Airborne spectroscopy measurement is a known tool for mapping large areas. It is often done with a helicopter or a small plane carrying detector systems that are relatively large compared to the standard systems that are used in laboratory environments. However, these crewed airborne measurements are limited due to minimum altitude restrictions and the possible contaminations in case of airborne sources. This is especially problematic in emergency situations, as there is limited information about the source and exposure pathways [13]. UAVs can supplement the measurements performed by first responders and emergency personnel as

they do not risk exposure to persons and are able to safely operate at lower altitudes.

The technical requirements for radiological monitoring using UAVs are strongly dependent on the type of UAV, the type of radiation and the type of source. The type of UAV is limiting the size and weight of the detector system. It also determines the speed and altitude of the flight, although this is also heavily dependent on the area and potential obstacles. The types of radiation influence the potential detector systems we can use. The possibility of contamination is linked to the type of source as well as the type of radionuclide. Noble gasses, for example, will have little to no danger of contamination. However, radioactive sources like a radiological plume ,with a radionuclide that is not a noble gas, can easily contaminate the surfaces of the detector and UAV. For radioactive sources like a radioactive liquid or ground contamination, the possibility of contamination is significantly lower. For lost point sources that remain intact, contamination is even impossible.

The type of detector also plays an important role in radiological monitoring. Dose rate detectors and spectroscopy detectors require different approaches in their design and requirements in regard to communication. Furthermore, there are different types of systems in both categories that have both advantages and limitations. For example, HPGe (High Purity Germanium) detectors have an excellent resolution, however, to reach this resolution the detector requires cooling with liquid nitrogen or electric cooling which increases the weight of the payload. Additionally, steps to reduce vibration and shocks have to be taken as this will impact the detector system negatively.

The two paragraphs above are meant to give an initial overview of the different parameters that have to be accounted for when using UAVs for radiological monitoring. This thesis research comprises the development of different drone-detector systems and using these systems in different test and realistic environments tackling the challenges in radiological gamma ray monitoring using drones or UAVs. The systems discussed in this thesis are tested in realistic environments with the aim to obtain a robust system that can operate in a variety of conditions.

The introduction of this thesis encompasses four main sub-chapters: (1) UAV Types and Characteristics, (2) Radioactivity and Radiation, (3) Detector Types and Characteristics and (4) Research Plan. The first sub-chapter, 'UAV types and characteristics', will elaborate on the different configurations encountered when working with UAVs as well as how they operate. The second sub-chapter, 'Radioactivity and Radiation', gives an overview of the origin and interactions of radiation focussing on parameters and concepts that are relevant for drone-based dosimetry and spectroscopy. The third sub-chapter, 'detector types and characteristics', will handle relevant detector materials and measurement techniques for use in drones ranging from Geiger Muller tubes to scintillator detectors. Each of these sub-chapter will contain literature to review the current state-of-the-art regarding radiation monitoring using drones. The final sub-

chapter, 'Research plan', contains a detailed description of the research plan including the overall problem statement, research questions and research objectives that are resolved throughout this thesis.

1.1 UAV types and characteristics

1.1.1 UAV Types

Unmanned aerial vehicles or drones come in a variety of shapes and designs. They can be divided into three groups, unmanned helicopters, multicopter UAVs and fixed-wing UAVs. Each of them has specific use cases as is mentioned in the following paragraphs [11], [12].

1.1.1.1 Unmanned Helicopters

Remote controlled helicopters often have a gas-powered engine. This allows them to fly longer and carry a heavier payload. They can hover over points of interest and are able to reach difficult areas with ease. However, they are expensive and require significant training to operate. Flight times of an unmanned helicopter are dependent on their fuel tank but are typically in the range of 1 to 2 hours [14]. Safety measures, such as parachutes, are also more difficult to implement due to the central rotor placement [11], [12]. Figure 1 shows an unmanned helicopter.

Figure 1: APID one unmanned helicopter used by Van der Veeke et al. [15], [16].

1.1.1.2 Multicopter UAVs

Multicopter UAVs or drones have four or more rotors that are symmetrically placed, in most cases the UAV will have a multiple of four rotors. They are mainly powered by batteries and are relatively easy to operate. Their most common use

cases are videography and photography, but by changing the payload they can be used in different fields of study or situations. Their size is often limited which also limits the maximum weight of the payload. Typical flight times of multicopter drones without a payload reach from 30 minutes up to 1 hour. They are agile and, if their size permits, are able to fly indoors [11], [12]. An example of a quadcopter can be found in Figure 2.

Figure 2: F550 DJI Flamewheel multicopter UAV with a payload containing a Geiger counter. Courtesy of Geert Olyslaegers.

1.1.1.3 Fixed-wing UAVs

Fixed-wing UAVs are similar to small rotary planes. Their training is mostly similar to that of unmanned helicopters, although they are longer and more complex. They can achieve significantly longer flight times of 10 hours or more. This is also dependent on their size, engine and fuel tank. A downside of fixed-wing UAVs is their space requirement for take-off and landing. Most systems require a catapult or runway to reach their required take-off speed. They also require ample space to land which is mostly done by classical landing gear or by parachute with added safety features. Fixed-wing UAVs can reach significantly higher speeds as multicopter UAVs or unmanned helicopters, making them ideal to survey large areas. However, their minimum speed is also an important factor as it determines the best spatial resolution achievable [11], [12], [17], [18]. Figure 3 shows an example of a fixed-wing UAV.

Figure 3: Penguin C fixed-wing UAV placed on a pneumatic catapult. Courtesy of SABCA.

A subdivision of fixed-wing UAVs are the vertical take-off and landing (VTOL) UAVs. As the name suggests they take-off vertically, hereafter, they reposition their rotors perpendicular to the ground. To land the procedure is reversed. The required space for take-off and landing is reduced, which is an important advantage for emergency scenarios with limited space, such as urban areas [12].

1.1.2 UAV Legislation

As of 2021, Belgium has adopted the UAV legislation of the European Union. UAV flights are categorised in three categories, open, specific and certified. The general rules for the open category are:

- The maximum flight height is 120 m above ground level (AGL).
- The pilot must maintain visual line of sight (VLOS).
- It is forbidden to fly in a no-fly zone.
- It is forbidden to fly over crowds.

For drones with a weight of 250 grams or above it is necessary that the pilot holds an EU drone license and registers him- or herself with the authorities to obtain an operator number. The open category is subdivided into subcategories A1, A2 and A3. Each subcategory has its specific rules, which are directly linked to the type of drone, the type of flight (rural, urban, …) and the flight plan (height, situation, …). As of January 1st 2024 it is also mandatory for newly manufactured drones to have a C-label stating the subcategory the drone is allowed to fly in. Additionally, it might be necessary to broadcast the remote ID of the drone in some categories, this is to identify the UAV and its pilot and digitally verify the aircraft in flight has the necessary authorisations.

The specific category is for flights operations that fall beyond the scope of the open category and requires the pilot to apply for a derogation from the aviation authorities (for Belgium; DGLV, DGCA or 'Directorate General for Civil Aviation). An example can be a flight over a nuclear site, which is technically a no-fly zone, or a flight beyond visual line of sight (BVLOS).

To fly in the specific category, you must either make a declaration if your operations meet the conditions of the standard scenarios, or obtain an operating permit based on your operational risk assessment (SORA or PDRA) or obtain a light UAS operator certificate (LUC).

If UAS operations pose too high a risk to be carried out in the specific category (either due to the type of operation or based on the results of the operational risk assessment), they have to be included in the certified category (e.g. air taxis).

The flights carried out in this thesis are in the open and the specific category. Figure 4 shows a snapshot of the no-fly zones of Belgium, these zones are time dependent and can change due to circumstances or exceptions. For our flights that include risk reduction measures, a permit under a standard scenario was requested. This simplified the process of obtaining permission for the specific flight [19-21].

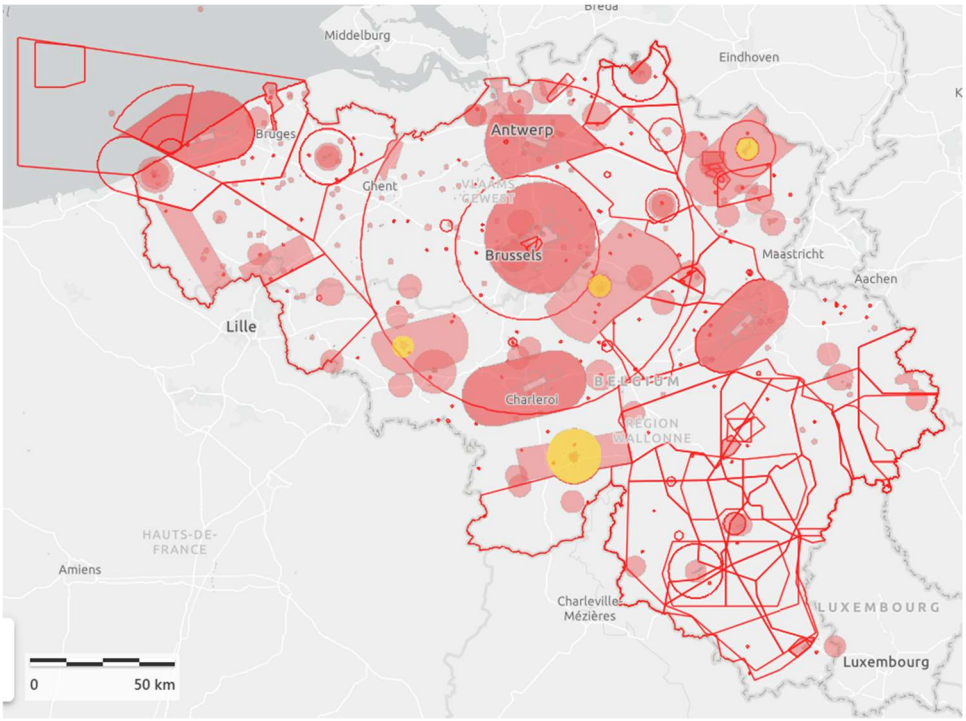

Figure 4: Map of the geozones in Belgium coming from the website of Skeyes [21].

The measurement campaigns done in case of a radiological or nuclear emergency, pose many operational risks. Aside from the possibility of contamination, turbulence due to the radiological plume or possible fires might compromise the flight stability of the UAV. Depending on the situation and environmental conditions loss of signal or loss of GPS signals is a danger that has to be taken into consideration. Lastly, multiple systems might be in the air at the same time, adding possible risks to collisions. These risks should be mitigated as much as possible, although not all of them are easy to control.

1.2 Radioactivity and Radiation

Radionuclides are atoms that have an unstable nucleus. Through the emission of different types of radiation, the nucleus will try to achieve a more stable state. The main types of decay that facilitate such a change are alpha, beta-minus and beta-plus radiation. They will alter the number of protons and neutrons to achieve a more stable configuration.

An alpha particle has the configuration of a helium nucleus, i.e. two protons and two neutrons. Due to their relatively high mass, they can cause significant damage to tissue. However, they are easily stopped by a couple of centimetres of air or by dead skin. Beta-minus particles, which are essentially electrons, can easily reach several meters in air but can be stopped by a couple of mm of aluminium. Beta-plus particles, positrons, are mostly stopped by various interactions such as Coulomb collisions, excitations and ionisations. Once energy is sufficiently low the recombination with an electron causes both particles to annihilate and produce two 511 keV gamma rays. This will be explained further in chapter 1.2.1.

However, after decaying, most nuclei will still contain an excess of energy. In most cases that energy is released in the form of gamma rays. The specific gamma rays emitted by a radionuclide inside a sample can be used to identify it by measuring the specific gamma ray energies that are emitted. These energies can then be used to compare with gamma energies of known radionuclides to identify the unknown sample, this is similar to comparing fingerprints to identify a person. Most gamma rays have energies between 30 keV and 4 MeV.

X-rays are similar to gamma rays with one key difference. They do not originate in the nucleus of the atom but are the residual energy of electrons. Electrons release energy through two pathways, bremsstrahlung and characteristic X-rays. Bremsstrahlung is caused by electrons that are experiencing a deceleration inside a medium which results in a very broad continuous energy distribution. Characteristic X-rays on the other hand are created by bound electrons around a nucleus that jump from a high energy shell to a lower energy shell with a vacancy. The excess of energy that is released is specific for the element and the shells. The X-rays produced by an element can be used to identify it and differentiate it from other elements. Most X-ray energies have energies between 0 and 150 keV. Both gamma rays and X-rays are electromagnetic waves. They have wavelengths of less than 1 nm and are classified as ionizing radiation [22-24].

In this thesis we will be focussing mainly on gamma rays and x-rays. They have the largest range and can be detected over larger distances. Detection of other types of radiation, alpha- or beta-radiation, would require different equipment.

1.2.1 Interactions with Matter

Gamma rays have three main interaction types with matter: photoelectric absorption, Compton scattering and pair production. Other interactions like Rayleigh scattering are not explained in depth as they have an insignificant effect in detector design. Photoelectric effect is mainly present in the lower energy ranges. Compton scattering is present over the complete energy range. And pair production is only a valid interaction pathway from energies higher as 1022 keV. A more detailed explanation of each interaction type will be discussed in the following pages. In this thesis, we are mainly measuring over distances in air, therefore, interactions with air will be of interest to us. Additionally, the interactions with detector materials are important since the choice of material will significantly alter the detectors capabilities, however, this will be discussed in depth in chapter 1.3.

The linear mass attenuation coefficient is dependent on the material and energy of the gamma- or X-rays and is used to calculate how many of the incoming rays are interacting with the material over the distance they travel through. The linear attenuation coefficients for gamma rays in dry air at sea level is shown in Figure 5 [25]. For example, when gamma rays of 1 MeV would travel through 50 m of dry air at sea level, 32 % of the initial gamma rays would be stopped over that distance. This can also be used to calculate the half-value thickness for gamma rays of specific energies. The half-value thickness is the thickness a material would need to stop half of all incoming gamma rays. For 10 keV, 100 keV and 1 MeV gamma rays the half-value thicknesses are, respectively, 1.1 m, 37.3 m, and 90.5 m.

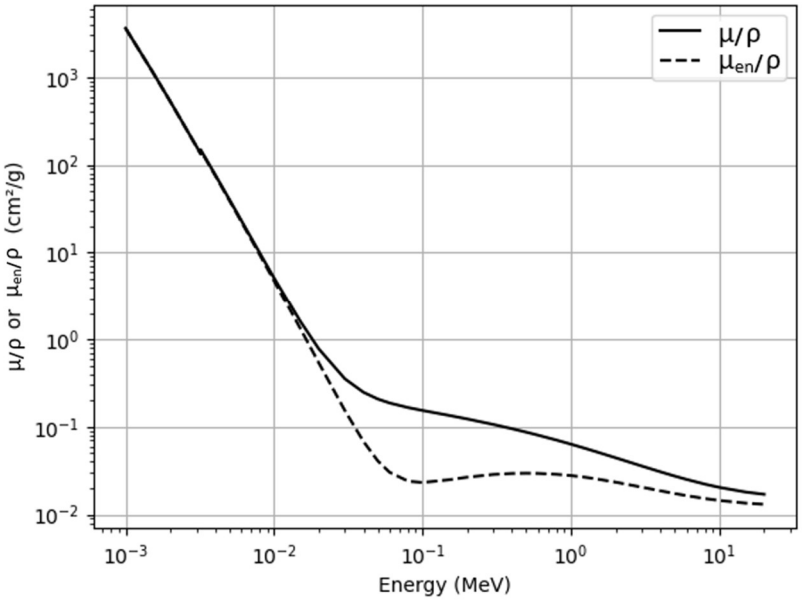

Figure 5: Mass attenuation coefficients for dry air near sea level. The full line represents the mass attenuation coefficient and the dashed line represents the energy absorption coefficient. Data is taken from the National Institute of Standards and Technology [25].

The first interaction type of gamma rays with matter, photoelectric absorption, causes a gamma ray to be absorbed by a bound electron which is then ejected from its shell. Because of the created vacancy it is possible that X-rays are produced after such an event, this is shown in Figure 6. The ejected electron will have an energy equal to that of the gamma ray minus the binding energy of the electron.

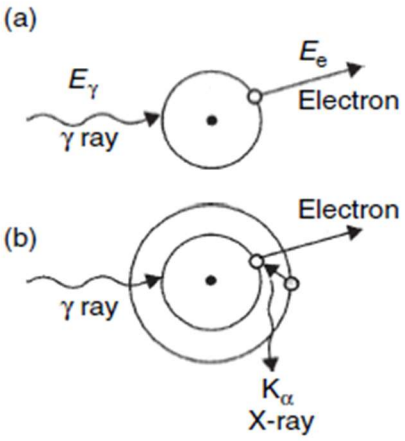

Figure 6: a) Schematic of photoelectric absorption together with the ejection of the electron that absorbed the gamma ray energy. b) After the ejection of an electron, the created vacancy will be filled by an electron from a higher shell. The change in shell causes the electron to emit an x-ray that contains the excess of energy [23].

The second type of interaction is Compton scattering. As the name suggests this is a type of interaction that scatters the gamma ray in a different direction. Compton scattering requires an electron to which part of the energy of the gamma ray is transferred. In doing so the electron is recoiled and the gamma ray has an adapted direction and energy, as can be seen in Figure 7.

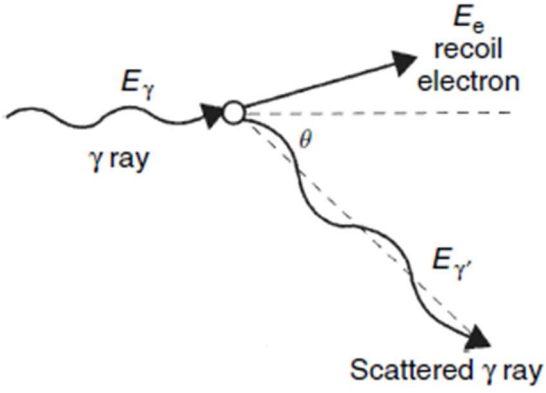

Figure 7: Schematic of Compton scattering. The initial gamma ray y changes direction due to scattering with an electron. This results in a scattered gamma ray y' [23].

Depending on the angle between the initial and the scattered gamma ray the energy transferred to the electron, E_e, is varying following Equation 1 [22-24].

$$E_e = E_\gamma \left[1 - \frac{1}{\left(1 + \frac{E_\gamma (1 - cos\ (\theta)\ )}{m_0 c^2} \right)} \right] \qquad (1)$$

Herein, E_γ is the initial gamma energy (*eV*), θ is the angle between the initial gamma ray direction and the altered gamma ray direction, m_0 is the rest mass of the electron (*eV/c²*) and c is the speed of light in vacuum (*m/s*) [22-24].

The third type of interaction is pair production. Pair production is only possible at gamma energies above 1022 keV. The interaction happens in proximity to a particle and creates an electron-positron pair, with the positron being the anti-particle of an electron. The proximity of a particle is necessary due to the conservation of momentum. The probability of the process occurring is dependent on the mass of the particle in proximity. Therefore, the probability will be higher in proximity of a nucleus as it would be in proximity of an electron. The reason for the energy restriction is due to the rest mass of the electron and the positron, they each have 511 keV/c² which in total gives us 1022 keV/c². Any additional energy is divided over both particles. The positron annihilates with an electron which creates two gamma rays with an energy of 511 keV, the complete process is shown in Figure 8. Because neither the positron or the electron will be at complete rest at the moment of annihilation, the measured peak at 511 keV might appear wider due to doppler broadening which causes one of the 511 keV peaks to be slightly lower in energy and the other one slightly higher in energy. However, their sum will still be 1022 keV [22-24].

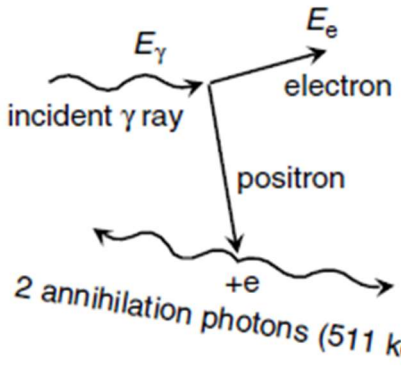

Figure 8: Schematic of pair production from a gamma ray with an energy over 1022 keV. The created positron creates two annihilation photons of 511 keV when combined with an electron [23].

Other interactions, such as Rayleigh scattering and (gamma, n) nuclear reactions, are less relevant for this thesis and will not be discussed further.

1.2.2 Dose Rate

The effects of radiation on humans are complex and depend on the type of radiation, the energy and the irradiated body parts. To estimate the effects of radiation on the human body, units for the amount of radiation absorbed by the human body are defined. Absorbed dose is used to define the amount of energy transferred to a certain mass when exposed to ionizing radiation and is expressed in J/kg. It is dependent on the energy of the particles, the fluence rate and type of tissue. A practical way of calculating the absorbed dose is done using air Kerma, K_{air}. Air Kerma is the amount of kinetic energy released to air per unit of mass of the air. Equating air Kerma and absorbed dose can only happen under charged particle equilibrium (CPE). CPE is warranted when the number of charged particles with specific energies entering the volume of interest equals the number of charged particles with the same energies exiting the volume. When we calculate the air kerma rate we can easily convert it to any operational quantity that is required [24], [26-29].

Dose rates can be defined in numerous ways. Each dose rate definition has its specific use case but has the same units, J/(kg.s). Therefore, it is important to select the correct type to report dose rates in an emergency scenario. The International Commission on Radiation Units and Measurements (ICRU) and its subdivision the International Commission on Radiological Protection (ICRP) have created definitions and conversion lists for the different ways dose rates can be expressed and reported. Figure 9 shows how the ICRU divided the different dose definitions and dose parameters into three different groups. For the use of dose rates in UAV measurements we will focus on the operational quantities as they can easily be calculated from the physical quantities and if necessary, can be converted into the required protection quantities. Furthermore, the operational quantities measured by a detector system can be calibrated and based on the detector response [24], [27-29].

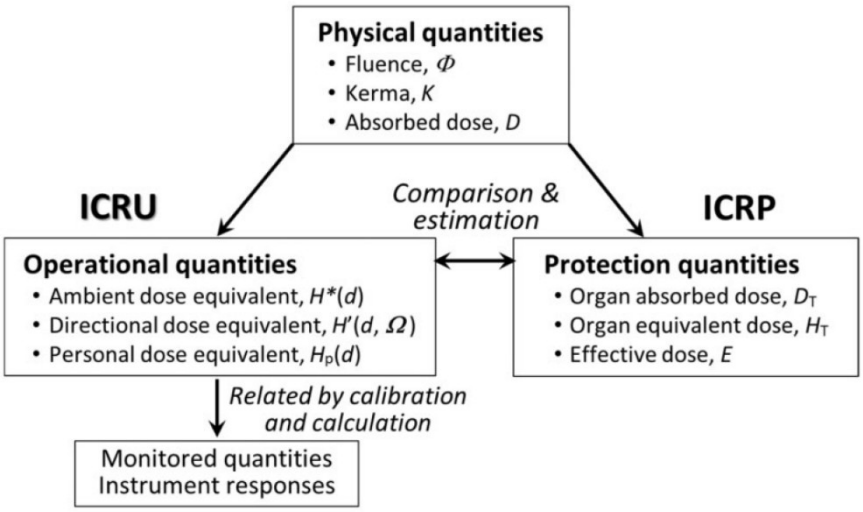

Figure 9: Schematic overview of radiation quantities from the ICRU and ICRP. They are divided into physical, operational and protection quantities depending on their use and definition [27-29].

One of the more common types to report dose rate in UAV measurements is the ambient dose equivalent rate, denoted as H*(10) [27], [28], [30-32]. The standard 6150AD-b dose rate detector measures H*(10) and is part of the SCK CEN's emergency equipment. As this system is seen as a standard device, the ambient dose equivalent rate H*(10) is chosen as dose rate definition. The ambient dose equivalent rate is for nearly all energies a conservative estimate of the radiation dose. For this reason, it is also often used in radiation protection for quantifying external irradiation of persons [27], [28]. There are several other dose rate definitions, like air Kerma, that can easily be converted into other standard values. However, it is important to clearly state the chosen definition as it can cause significant changes in the dose rate value. The definition of the ambient dose equivalent rate is defined by the ICRP as follows: *"The ambient dose equivalent, H*(d), at a point in a radiation field is the dose equivalent that would be produced by the corresponding expanded and aligned field in the ICRU sphere at a depth, d (mm), on the radius opposing the direction of the aligned field. The recommended value of d is 10 mm for penetrating radiation and 0.07 mm for low-penetrating radiation"* [27-29].

As we mainly work with gamma energies of 30 keV up to 3 MeV, the case of penetrating radiation is most fitting. The ICRU sphere is made from a fictive tissue equivalent material with a diameter of 30 cm. The fictive tissue equivalent material contains 76.2% oxygen, 11.1% carbon, 10.1% hydrogen and 2.6% nitrogen [29].

Figure 9 shows the complexity of the different dose rate units and definitions. Dose rate measurements are one of the initial parameters on which decisions are

based involving safety and cordoning off the environment for radiological and nuclear scenarios. Therefore, it is adamant that the communication towards the first responders in case of a nuclear or radiological scenario is clear. The types of scenarios can go from simple lost point sources to nuclear incidents involving multiple sources and several contamination and irradiation pathways. Chapter 1.2.3 gives an overview of these scenarios and the different dangers they contain. The dose rate values have to be available in a moment's notice in case of a nuclear or radiological emergency. Therefore, ground or Telerad stations are placed throughout Belgium and specifically near nuclear sites. There are different types of stations, but most have dose rate detectors as well as spectroscopy detectors that measure environmental radioactivity in air, ground or even water. They are continuously monitored and data can be retrieved when necessary.

1.2.2.1 Dose Rates from Spectra

There are mainly two types of radiation detectors. The first type, dose rate detectors, convert the measured radiation directly into dose rate values such as ambient dose equivalent rates. The second type, spectroscopy detectors, do not only measure the intensity of the radiation, but also measure the energy of the incident radiation. The number of photons that is measured is expressed as counts or counts per second. The energy of the photons is expressed in eV. When the number of counts is shown in function of the energy we obtain a spectrum. From spectra we can identify the radionuclide that emitted the measured photons. However, converting a spectrum to dose rate requires special attention.

Dose rates are less complex in comparison to spectra. Dose rate values are available from ground stations and can be presented and easily understood by the first responders. However, identification and quantification are not possible with dose rate detectors alone as the energy resolution is not available or usable for identification. Spectroscopy detectors have the capability to identify and even quantify the radiation source. However, the obtained data is more complex and not easily comprehensible for all first responders. To achieve the advantage of dose rate readings together with the possibility of identifying and quantifying the radiation source we can implement a stripping algorithm. Stripping links the counts in an energy window in the spectrum to their respective theoretical dose rates. This way we obtain a weighing factor for the number of counts in a specific energy window. In post processing we can calculate the measured dose rate using the weighing factors of the energy windows. The calculation of the weighing factors for stripping is explained in Grasty et al., Camp et al., Tsuda et al., and Dombrowski [33-36] for different detector materials and geometries. Figure 10 shows a typical graph of the weighing factors in function of the energy and is taken from Grasty et al.. It also shows the spacing in energy windows is short at lower energies and larger at higher energies, this is required to achieve a reliable curve since the variations are more pronounced at lower energies [33]. A more detailed explanation with formulas can be found in chapter 2.2.2.2.

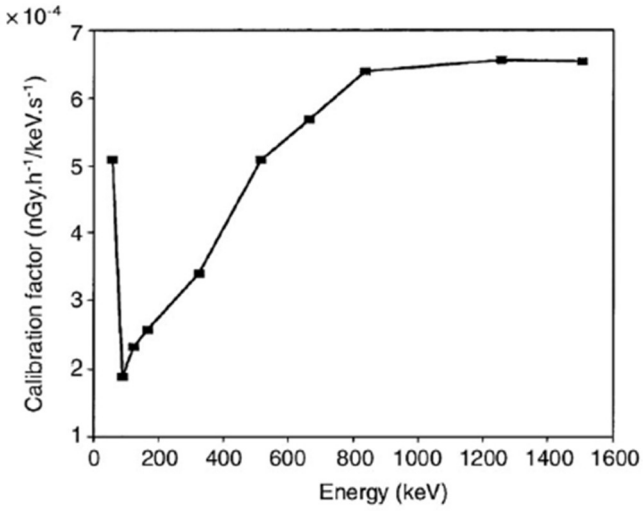

Figure 10: Example from Grasty et al. showing the typical shape of the weighing factors in function of energy used to perform stripping on a spectrum [33].

Nevertheless, to achieve reliable weighing factors, it is best to use mono-energetic sources in the calibration of the detector. Mono-energetic sources have a limited contribution to counts in other energy windows, making them independent from the other weighing factors. However, mono-energetic sources for all energy windows are not always available, therefore it is useful to develop a digital model of the detector in a Monte Carlo simulation. By using a verified Monte Carlo model, we can simulate the effects of mono-energetic sources as is demonstrated in Casanovas et al. [37]. The use of Monte Carlo simulations for stripping has its limitations as the model that is used might not be an actual representation of reality.

1.2.3 CBRN Scenarios

CBRN (Chemical, Biological, Nuclear and Radiological) threats can have many potential scenarios and can be either accidental or deliberate. Due to their big impact, it is important to achieve a fast risk assessment to assess safety for both the public and the first responders. In this thesis we will only discuss radiological and nuclear scenarios. Radiological and nuclear events can be classified into three types of events. The first type is a nuclear event with atmospheric release, this can be either accidental, deliberate sabotage, a nuclear warhead or an improvised nuclear device. The second type is a radiological dispersion device (RDD), this can be an explosive (also known as a 'dirty bomb') or a non-explosive RDD (e.g. contamination of a public water or food supply). The last type is a radiological exposure device (RED) that is either a sealed or a non-sealed radioactive source [38].

Possible exposure pathways are irradiation, internal contamination and external contamination. Irradiation covers external exposure to radiation such as cloud

shine and ground shine. Cloud and ground shine refer to the radiation coming from respectively a radiological plume or cloud and the contaminated ground after wet or dry deposition. Internal contamination happens when radioactive sources are inhaled, ingested or enter the body through a wound. External contamination is the contamination of the skin and clothes of a person with a radioactive source [38].

Table 1: Exposure pathways for typical radiological and nuclear scenarios.

Radiological and nuclear scenarios	Exposure pathways
Explosive RDD	Cloud shine, ground shine, inhalation, ingestion, external contamination and internal contamination through wounds caused by the explosion
Non-explosive RDD	Cloud shine, ground shine, inhalation, ingestion and external contamination
RED	Irradiation
Atmospheric release	Inhalation, ingestion, external contamination and irradiation through cloud or ground shine

Each event type requires a different approach. For example, in case of an explosive RDD it is important to consider a secondary explosive RDD that might be targeted towards the first responders. UAVs and UGVs (Unmanned Ground Vehicles) can play an important role in such cases as they can be controlled from a safe distance without risking the safety of the first responders. In each radiological or nuclear event there are potential exposure pathways for both the public and the first responders: direct exposure from a source, cloud shine, ground shine, inhalation and ingestion. Each pathway has its specific risks and safety measures like air filters and protection suits. Table 1 gives the different exposure pathways linked to the scenarios above.

As every scenario requires a specific approach, the equipment for each scenario also changes. For unknown sources, dose rate detectors will not be able to identify the source, while for evacuations an initial dose rate estimate is significantly more useful as spectral information. This also means that the systems can be optimized for each scenario. However, to test these systems outside of a controlled environment we have to create non-emergency scenarios to prove their accuracy and capabilities.

Alpha and beta radiation require different precautions as for gamma or x-ray sources. Alpha and beta radiation are especially harmful when consumed or inhaled. To evade these types of radiation entering the body, PPE (Personal Protective Equipment) like protective suits, gloves and full facemasks with specialized filters are used by first responders. Identification of the radionuclide in question is rather difficult in the field. The alpha and beta particles will interact

with the air making spectroscopy in the field difficult as it influences their energy. To identify these types of radiation, samples and swaps are taken. These samples can be air, ground, water or any other form of material. Hereafter, the samples can be measured in laboratories under controlled conditions, allowing identification to be done [39]. Alpha and beta spectroscopy will not be handled further in this thesis, however, the topic would certainly be interesting for future research.

Measurements done by helicopter or aeroplane are a frequently used tool for measuring contaminations in large areas in the aftermath of radiological or nuclear events. The minimum number of people required for these measurements is one pilot and one detector operator. Both helicopters and aeroplanes have a minimum flight altitude resulting in a larger source-detector distance which causes issues regarding efficiency. The detector systems used in combination with helicopters or aeroplanes are often bigger and heavier to overcome this issue [8], [13].

Current events in Ukraine, more specifically the nuclear powerplant in Zaporizhzhia, and the attack on the nuclear installations in the middle east add urgency to the readiness of systems that can track radiological plumes and delignate hotspots. When these emergencies occur, rapid and independent verification will be necessary.

Well-known examples of nuclear events with atmospheric releases are the meltdowns in Fukushima Daiichi and Chernobyl. Both cases were accidental but their effects are still a point of concern today. On March 11th 2011 an earthquake caused a tsunami near the coastline of Japan. A combination of the power loss due to the earthquake and the flood caused by the tsunami, caused the Fukushima Daiichi nuclear powerplant to lose cooling power. As a consequence, several units developed a breach in containment resulting in significant releases of different isotopes such as Caesium-134, Caesium-137, Iodine-131, Krypton-85 and Xenon-133. The Caesium and Iodine isotopes contaminated the surrounding food and drinking water which required the government to put restrictions on their consumption. The noble gasses Krypton and Xenon were released, creating a radioactive plume causing cloud shine. The Japanese government increased the dose limit for the public from 1 mSv/year to 20 mSv/year for certain areas around the exclusion zone. Even with this adaptation it forced people to move from their homes. Once the environment is sufficiently decontaminated, the dose limit should be brought back to the 1 mSv/year [40].

Several characterization and remediation efforts have been done to the affected area. Sanada et al. [14] performed six measurements with an unmanned helicopter, R-MAX G1 by Yamaha, to map the dose rate distribution in the area around the FDNPP (Fukushima Daiichi Nuclear Power Plant) in the first four years after the accident. Figure 11 shows the flight lines of their study and the black dots represent the ground measurements done around the site. The dose rates measured by the unmanned helicopter were calibrated on six points. The results of the unmanned helicopter were then compared to ground measurements. All six flights produced a nearly identical dose rate as the ground measurements. Slight

variations in the measurements were attributed to variations in the field of view of the aerial and ground measurements. An important sidenote with this research is that it is assumed that the contamination is homogenous. This is rarely the case but due to the large field of view of the aerial measurements, heterogenous contaminations will be averaged out. The unmanned helicopter can easily repeat earlier flightpaths, can reach difficult to reach areas and can rapidly characterise the radiation distribution over a large area. It has a maximum flight endurance of 90 minutes and a maximum communication distance of 3 km. The flight height in this experiment was between 50 and 100 m with an approximate speed of 8.0 m/s. The spacing between flight lines was set to 80 m and the total surface, 52 km², was characterised over one month. One key advantage of the unmanned helicopter is its reduced flight height. In Belgium, crewed helicopters have to maintain a minimum above ground level (AGL) height of approximately 150 m [14], [41] due to safety concerns while the unmanned helicopters have a maximum flight height of 120 m [19], [20], [42].

The rules regarding minimum AGL for both crewed and unmanned helicopters are also dependent on the surroundings, the situation and requests for derogations with the governmental institutes concerned with the oversight of these flights. Similar studies were done around the Chernobyl exclusion zone as can be seen in Conner et al. [17], [18]. Although these examples focus on characterisation after a radiological or nuclear event, it is certainly possible to develop a similar system that can be used during such an event. The first responders require the characterisation as soon as possible, hence, a system that is active during the emergency will prove to be useful in delineating safe zones. However, some key-features have to be kept in mind, like possibility of contamination of your craft, reliability, safety considerations, deployment time and additional training for operators and first responders. Smídl et al. [43] provided simulations of two UAVs following an incidental release of a radiological plume. The data from the two UAVs supplemented the measurements of the stationary network. As a result, the release could be followed with more accuracy. An additional advantage of UAVs that was mentioned by Smídl et al. is the adaptable flight height. [43] As this study was theoretical, it is of great interest to perform such measurements in a real environment to review whether the findings remain the same.

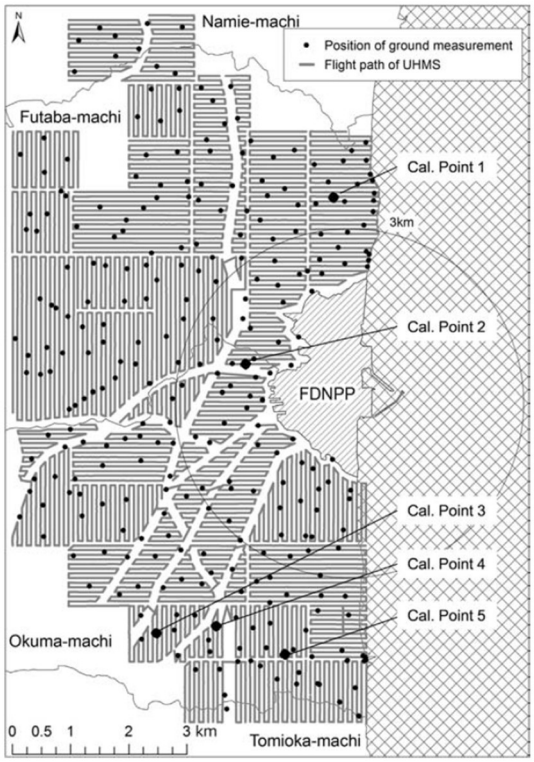

Figure 11: Flight lines from the study done by Sanada et al. with the black dots representing ground measurements to validate the results obtained from the unmanned helicopter. The calibration points were areas over which the unmanned helicopter hovered for 2 minutes. The calibration points were selected over areas that were flat and with an average dose rate of 7 µSv/h [14].

When remediating an area that has been contaminated, UAVs can be used to perform the exact same measurement before and after the remediation. This allows us to have a one-on-one comparison, clearly showing the impact of the remediation efforts. This is already proven by Connor et al., Martin et al. and Cresswell et al. [44-47]. Connor et al. used a Sigma-50 CsI scintillator detector mounted underneath a quadcopter. The Sigma-50 is a 2' by 1' by 1' CsI scintillator from Kromek that uses a silicon photo multiplier. Connor et al. performed measurements before and after remediation efforts to compare both to assess the efficiency of their efforts. The results of Connor et al. are shown in Figure 12. Although there is an overall reduction, the north-eastern corner and the north-western side had an increase in dose rate. It is certainly possible that this is due to the remediation, but it could also be linked to variations in position or height. At the edge of the measured area the influence of unremediated soil outside of the fence can have a significant influence [44], [45].

Another advantage of UAV measurements is that it removes the dose obtained by an operator that would have to do the measurements manually. Additionally, the effect of a human body in close proximity to the detector might even cause some shielding, which influences the measurement as is shown in Martin et al. and Buchanan et al. [48], [49]. The reproducibility of the UAV measurement will also be more accurate as is the case with a human operator.

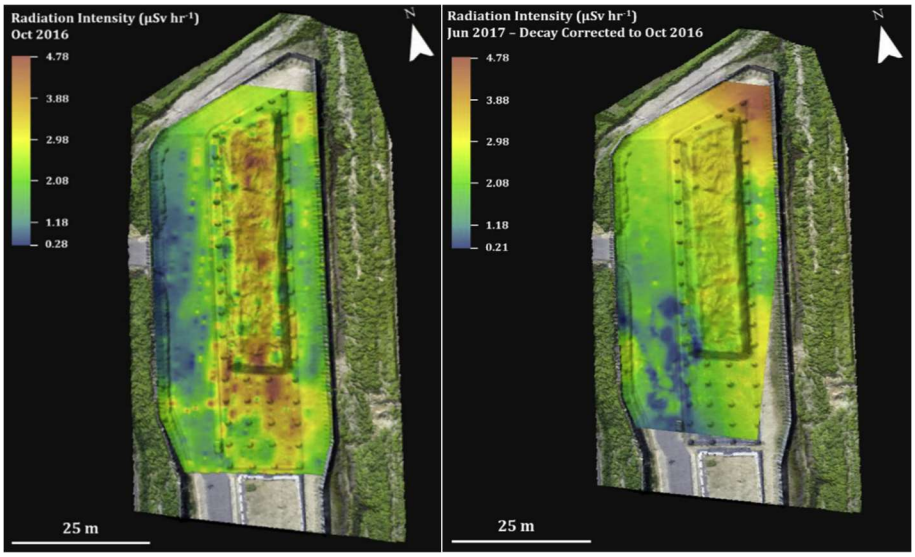

Figure 12: Comparison of measured dose rates before (left) and after (right) remediation efforts. The study was done by Connor et al. using a quadcopter and a CsI scintillator detector (Sigma-50 from Kromek) [44], [45].

Each of the measurements done by Sanada et al. [14] were done over several months. In case of an emergency scenario the time frame does not allow for such a long interval. In Connor et al. [44], [45] the size of the area of investigation is relatively small. This is no issue when reviewing remediation efforts, but in case of a lost source or contaminations over larger areas, this type of drone-detector system will not suffice. Therefore, we need to achieve a drone-detector system that can handle larger areas and flight times, while maintaining sensitivity.

The chapter above brings us to the first research question: How to assess the dose rate distribution of an environment in case of a nuclear or radiological scenario at a safe distance using UAVs to assist first responders in delineating unsafe areas? This question brings forth three additional questions. First, what type of dose rate should be evaluated? Second, which types of detector systems can be used for assessing the dose rate distributions? Last, what are the advantages and disadvantages of each detector system?

1.3 Detector Systems

Detection and identification of radioactivity is not straightforward. The type and energy of the radiation are key factors in the selection of the detector system. Therefore, it is necessary to select the right detector system for the situation. In the next three subsections we will review three types of detectors that could be used as a payload in combination with UAVs.

1.3.1 Geiger Muller Detectors

There are mainly three types of detectors that are used in combination with UAVs. The first type is Geiger Muller counters. They work on the principle of ion-electron pairs created by ionisation of the gas inside of the detector volume. To register the creation of the ion-electron pairs, an electric field is created by setting a bias voltage over the gas container. The electric field will move the ions and electrons to respectively the cathode (negative) and the anode (positive). There they will cause a pulse that can be registered.

The electric field in Geiger Muller detectors is so high that the creation of an ion-electron pair will cause an avalanche of charge creations which is called avalanche multiplication. The pulse created by the charges is independent of energy or type of radiation and therefore, not suitable for spectroscopy purposes. However, it is a relatively cheap and easy system to build and maintain. A downside of a Geiger Muller detector is the deadtime. Deadtime is the time a detector needs to collect the charges from incoming radiation and register the acquired signal. During this time the detector cannot detect a new incoming signal and is not responsive or 'dead'. There are some solutions for high deadtimes like quenching gasses but discussing them falls beyond the scope of this thesis [23].

The implementation of a Geiger Muller counter in combination with a UAV is shown to work in Khan et al., Katreiner et al., and Olyslaegers et al. [50-52]. It can provide quick count rate maps of an area to pinpoint hotspots or point sources. Furthermore, Geiger Muller counters are cheap and light in comparison to scintillation and semi-conductor detectors, meaning that if they were contaminated, the cost to replace the detector and drone is limited in some cases. Additionally, we can use multiple Geiger Muller counters to create a directional system. Khan et al. created a system with three Geiger Muller detectors placed in a forward-facing triangle [50]. Although this system is meant for a UGV, it could be adapted for UAVs. Geiger Muller counters can also work at higher dose rates. Therefore, they can be used in high activity environments, while other detector systems will be saturated.

1.3.2 Scintillator Detectors

The second type of detector is a scintillator detector. Scintillator detectors are made from crystalline materials that are insulators. Their detection method is through visible light. The bandgap for insulators is too large for electrons to excite to the conduction band completely, therefore, the excited electron will remain

attracted to their recently vacated hole [22-24]. As they de-excite the absorbed energy will be emitted in the form of visible light.

Some of the requirements of a scintillator detector crystal are:

- Decent number of electron-hole pairs created by the incoming radiation
- The crystal must be transparent to allow light collection
- The light production must be proportional to the absorbed energy
- They should have a decent stopping power to be able to absorb the incoming radiation
- The decay time of the excited state must be short for higher count rates
- The cost of the material should be reasonable and the refraction index of the material should be easy to couple to photomultipliers.

Some of the frequently used materials are Sodium Iodide (NaI), Caesium Iodide (CsI), Lanthanum Bromide ($LaBr_3$), Cerium Bromide ($CeBr_3$) and Bismuth Germanate (BGO). Scintillator materials like NaI and CsI do not de-excite by emitting visible light but emit energies higher in the electromagnetic spectrum. As this makes detection of the pulses difficult and might cause them to be absorbed, we want to avoid pulses outside of the visible light. The solution for both issues is an activator. For NaI, Thallium (Tl) is used and for CsI, Thallium or Sodium (Na) is used. The amount of activator added is in the order of magnitude of 10^{-3} mol. The activator adds sites between the valence and conduction bands lowering the amount of de-excitation energy as is shown in Figure 13. The lower de-excitation energy might shift the electromagnetic rays to the visible light. Not all energy absorption will result in light output, a large part of the energy will be converted into heat and lattice vibrations [22-24].

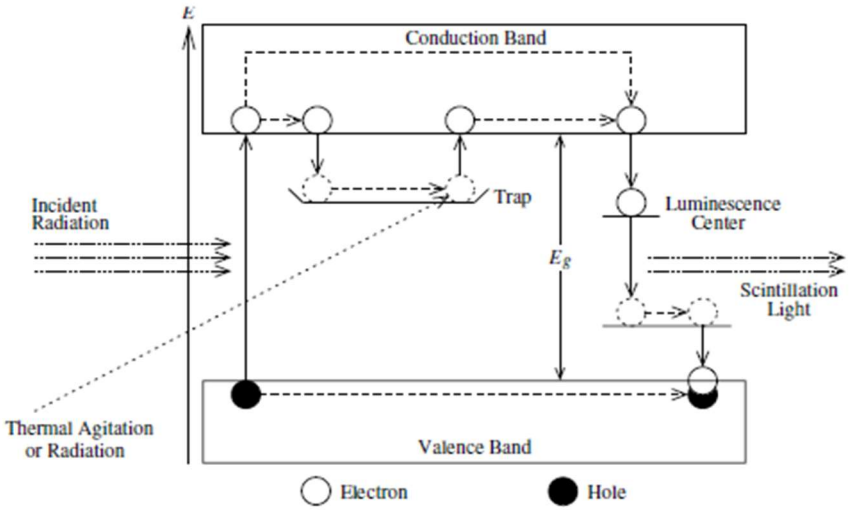

Figure 13: Schematic view of the excitation and de-excitation of an electron in a scintillator material. The upper rectangle represents the conduction band and the lower rectangle the valence band [23].

The lifetime of an activator state is very short, in the order of 100 ns. The almost instant emission is called luminescence. The short decay time allows the creation of short detector pulses. The number of excited states is mostly just one. However, it is possible there are multiple significant activator sites with different lifetimes. In some cases, the de-excitation to the ground state might be forbidden. The lifetime of such de-excitations is significantly longer as they require to gain some additional energy through thermal excitation to allow for the de-excitation to happen. The emitted light from these relatively long-lived de-excitations is called phosphorescence or afterglow. The afterglow might cause issues with the background [22], [23], [53].

Scintillator detectors are relatively temperature independent. Although the electronics still might cause some temperature dependence. A downside to some scintillator detectors is that they are hygroscopic, meaning that they tend to absorb water making the detector perform worse [22-24]. The created light pulses need to be converted into an electrical signal. For this a photomultiplier tube (PMT) usually is used. Figure 14 shows the cross-section of PMT with a scintillator mounted on the left.

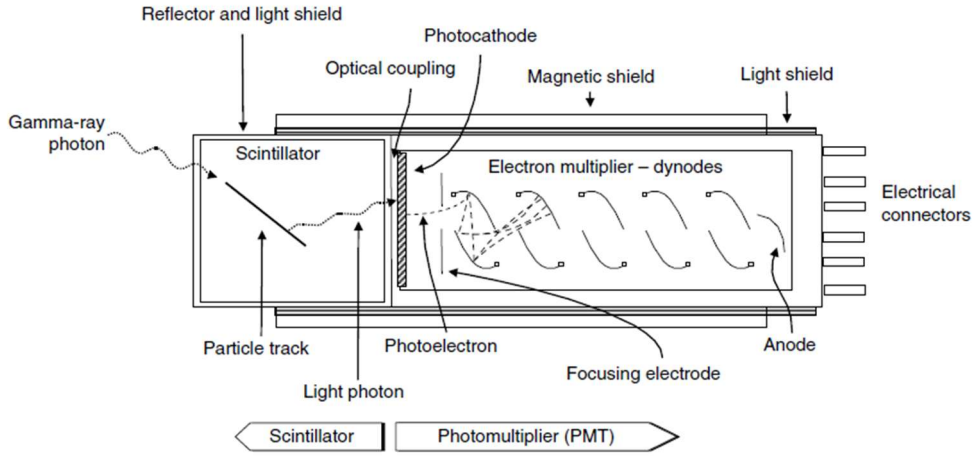

Figure 14: Section view of a scintillator detector with an integrated photomultiplier tube [22].

The initial step is collecting the gamma ray in the scintillator crystal which is converted into light pulses. The crystal is wrapped in reflective material so all light is collected at the photocathode which is connected to the PMT with an optical coupling. The photocathode converts the light pulses into electrons. As the electrons do not carry enough charge, we have to amplify the signal. The amplification is done by using multiple dynodes with increasing voltages. The photocathode electrons are accelerated towards the first dynode, on impact the electrons create additional electrons that are accelerated towards the next dynode. This happens in multiple stages and with each stage the signal is amplified. The last dynode is the anode and is connected to the PMT output. The

dynodes are enclosed in a glass vacuum tube. In air, the electrons would not be able to travel and the high voltages could possibly create arcs. Photocathodes are only efficient at a specific range of wavelengths which is specific for the type of photocathode. The photocathode and the scintillator wavelengths have to agree well to allow for a good detector response [22], [23], [53].

An alternative to PMT's are photodiodes or silicon photomultipliers (SiPM). They tend to have a larger sensitivity range, they are insensitive to magnetic fields and they are significantly less heavy compared to PMT's. They also have a higher quantum efficiency compared to the PMT's. The quantum efficiency is the number of photoelectrons emitted per incident photon. The main disadvantage with SiPMs is that they produce a small signal which is problematic when the noise levels are too high, therefore they require additional amplification as soon as possible to avoid the influence of noise. An additional issue is the temperature dependence of the gain. However, by compensating the bias voltage we can stabilize the gain [54], [55]. For larger detectors multiple SiPMs can be placed to achieve better light collection. SiPMs are gaining popularity at the moment, they are less bulky and weigh considerably less. The size and weight improvement of scintillation detectors that use SiPMs make them a valid candidate to be used with a UAV [56], [57].

1.3.3 Semiconductor Detectors

A semiconductor is a crystalline material that exists out of atoms held by covalent bonds. Their electrical properties depend on several factors causing them to be somewhere between an insulator and a conductor. Germanium and Silicon are two of the most used semiconductor materials. Other types of semiconductor materials like CZT (CdZnTe or Cadmium Zinc Telluride) are becoming more commonly used as their production processes become more advanced and allow the creation of larger and more accurate crystals [22], [23], [53].

Semiconductor detectors are essentially diodes that have been put into reverse bias to fully deplete them. Any additional excitations that happen due to radiation will give rise to an electric pulse in the form of electron-hole pairs. The depletion region can be seen as a layer of insulating material, therefore, creating a capacitor using the electrical contacts. The capacitance of a radiation detector is an important parameter as it directly correlates with the achievable resolution of the detector. The capacitance depends on the shape and size of the crystal and it is preferable to keep it as low as possible. Additionally, it is important to keep the microphonic noise in the detector as low as possible. The vibrations will alter the capacitance causing the resolution to decrease [22], [23], [53].

Another important factor for semiconductor detectors is the charge collection time. This is the time it takes to collect all electron-hole pairs created by the incoming radiation. One of the key parameters is the mobility of the charge carriers. This parameter is related to the semiconductor material and the mobility of electrons is higher as that of holes. The charge collection time is also influenced by trapping. Shallow trapping, small energy pits that hold the created charges,

have a limited effect on the charge collection time as the trapped charge can easily be re-excited to allow full charge collection. For deep trapping, deep energy pits, the charges can stay trapped until the remaining charges are collected by the electronic system resulting in a loss of charge. This will cause a wrongful energy output [22], [23], [53].

For UAV measurements using semiconductor detectors the main issues are vibration and cooling requirements, especially for HPGe (High Purity Germanium) detectors. The equipment to cool a HPGe detector is relatively heavy which is problematic when mounted under a UAV. It will reduce the flight time significantly. As mentioned earlier, the vibrations due to the UAV will impact the resolution negatively. HPGe detectors do have an advantage that their size can be significantly larger than other standard semiconductors, like CZT or PIPS (Passivated Implanted Planar Silicon) detectors. This makes their full energy peak (FEP) efficiency significantly higher, which is an important factor when measuring at larger source-detector distances.

As is already shown in Bell et al., Vargas et al. and Lowdon et al., there are several spectroscopy detector materials, both semiconductor and scintillation, that can be combined with UAVs. Furthermore, each of those systems can be optimized to work with UAV measurements [58-60]. However, it is important to optimize these systems under the same restrictions. For UAV measurements these restrictions are size, weight and robustness. Detector systems that are too large will cause issues with the stability of the UAV. A weight restriction is necessary to assure the maximum take-off weight (MTOW) is not exceeded. Additionally, the weight will influence the flight time as a heavier load will shorten the flight time significantly. The detector systems should also be able to withstand vibrations and weather. The vibrations originating from the UAV could be counteracted with mounting brackets with vibration suppressors, although this adds weight to the system. A last risk is the contamination of the detector system. Therefore, it is important that the price of the detector system and UAV stays within a reasonable amount, as they can be contaminated rendering them useless.

Although Bell et al. gives a thorough overview of the different detector types and materials for airborne radiation monitoring, they do not compare the systems for the same UAV setup [58]. As mentioned above, weight and volume are important parameters to consider as it limits the drones flight time or even grounds it when the weight is over the MTOW. The difference in volume is also visible in Table 2 when the absolute efficiencies are compared to each other. HPGe has the best efficiency, but considering their smaller volumes, $CeBr_3$, $LaBr_3$ and CsI(Tl) are still good options. Bell et al. recognized the difference in volume and geometry and compared the materials accordingly. However, the effect of detector geometry and limiting the weight of the final crystal are interesting topics to investigate further as they can be optimized for specific UAV systems.

Table 2: Table from Bell et al. showing the different detector materials and efficiencies for the 662 keV gamma energy from Cs-137 [58].

Detector	Absolute efficiency at 662 keV	Efficiency relative to HPGe	Volume relative to HPGe
HPGe	1.161(50)%	[n/a]	[n/a]
$CeBr_3$	0.649(11)%	56%	34%
$LaBr_3(Ce)$	0.658(11)%	56%	34%
Cd(Zn)Te	0.01167(28)%	1.0%	0.59%
CsI(Tl)	0.3116(61)%	27%	19%

1.3.4 Signal Processing

The next steps in the complete detector system are a preamplifier, an amplifier and a multichannel analyser (MCA). However, in most modern systems the preamplifier is already built into the detector housing immediately after the SiPMs or PMTs.

The charge created by radiation in a semiconductor detector is proportional to its energy. However, the amplitude of the charges created by the radiation is too low and can easily be lost in noise. A preamplifier can increase the amplitude and convert it to a readable voltage level. It is important that the amplification happens as fast as possible after collection to minimize the noise superimposed on the signal and keep a good signal-to-noise ratio (S/N). The next step is an amplifier that changes the pulse shape and increases the amplitude further. The new pulse shape is then the input to the MCA. The MCA sorts the pulses by pulse height in different bins and converts it to a digital signal. The final spectrum is a visualisation of the MCA's sorting and with an energy calibration it can be used to identify unknown samples. The detector setup also requires two voltage supplies, one for the detector bias voltage and one for the preamplifier voltage.

The preamplifier is the first amplification step to achieve a better signal-to-noise ratio. There are two types of preamplifiers, resistive feedback preamplifiers and reset preamplifiers. Resistive feedback preamplifiers have a feedback resistor, R_f, a feedback capacitor, C_f, and an operational amplifier. The circuit has a time constant defined by the product R_fC_f. The time constant controls how long the collection of charges remains active. The long decay time can cause pile-up due to multiple consecutive pulses. The pile-up is only a real issue when the signal rises above the dynamic range of the preamplifier due to a high count rate, as is shown in Figure 15. If this is the case, the preamplifiers output pulse height will no longer have a linear association to the collected charges. At even higher count rates the preamplifier will not be able to output any pulses and the detector system will no longer work [22], [23], [53].

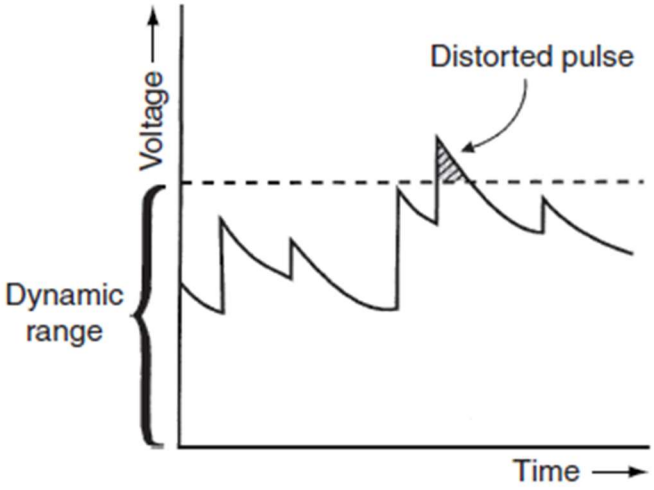

Figure 15: Pulse height in function of the time for a piled-up detector. When the voltage reaches the extent of the dynamic range. The peaks that achieve voltages above of the dynamic range the resulting pulse will be distorted [22].

With a reset preamplifier we measure the step increase instead of returning the signal to the base voltage using a feedback resistor, we reset the signal once the limit of the dynamic range is reached. This way we avoid pile-up. However, during the reset the charge collection is briefly stopped by an inhibit signal. The downside of a reset preamplifier is the mandatory dead time caused by the reset inhibit. The reset takes roughly two to three pulse widths of time. For higher energies the number of resets will also increase as the dynamic range is reached faster causing more resets to happen [23].

The amplifier that follows the preamplifier is mainly used to shape the pulse and amplify the signal further. The amplification factor is the product of the fine and coarse gain. Additional functions of the amplifier are pole-zero cancellation, baseline shift and pile-up rejection [22].

The noise involved with pulse shaping can be subdivided into three contributors. Series, parallel and flicker noise. The origins of these types of noises are beyond the scope of this thesis. For now, it is only important to know that the noise can be set at a minimum for a specific shaping time constant [22], [23], [53].

Pole-zero (PZ) cancellation is needed to resolve artefacts caused by the shaper. Figure 16 depicts the pole-zero problem. The tail of the shaped pulse might drop below the baseline. A pulse that closely follows the previous pulse will start to rise at a lower baseline resulting in a different pulse height. Most recent amplifiers have an automatic PZ algorithm. For reset preamplifiers PZ cancellation is not required [22], [23], [53].

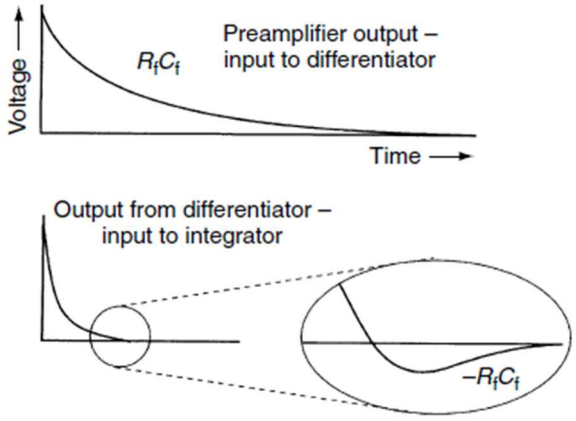

Figure 16: Example of the undershoot in a pulse that is uncorrected for pole-zero [22].

Baseline shift is required when multiple consecutive pulses are shaped. The DC components will not be allowed to pass causing a drift in the baseline. Most recent amplifiers have a baseline restorer (BLR) as standard, a BLR brings the baseline back to ground potential [22], [23], [53].

A last function that is present on most amplifiers is pile-up rejection (PUR). Pile-up is an effect that happens at high count rates when two pulses are detected within the same shaping time constant. The two pulses will be combined as one single event which is undesirable. PUR uses two pulse shaping methods in parallel. A first method uses a short time constant disregarding any noise issues. It is only used to detect pulses. When a second pulse is detected before a predefined time period has passed it will trigger an inhibit signal to block the second method. The second method has a normal time constant to process the pulses. This method will pause when the inhibit signal is high to avoid the pile-up. Both pulses will then be disregarded causing a slight increase in dead time [22], [23], [53].

MCAs sort the incoming pulses from the amplifier into their representative energy bins. The resulting histogram is the gamma ray spectrum. Some of the parameters in the recording of a spectrum are the lower level discriminator (LLD) and the upper level discriminator (ULD). They set the respective minimum and maximum pulse heights used to populate the spectrum. The live, real and dead time (LT, RT, DT) of a spectrum are also important parameters to consider, especially when measuring spectra for calculating activities. The live time is the time the detector was actively measuring, the dead time is the time the detector was not able to process pulses and the real time is the sum of the live and dead time. Digital offset causes the complete spectrum to shift, this might be useful to use the total amount of channels available [22], [23], [53].

Instead of the standard spectral data, we could choose a different approach, list mode. List mode, as the name suggests, returns a list of all the measured pulses.

In list mode we would not have any issues due to the movement of the detector system as the measured pulse is nearly instantaneous. However, this requires significant computing power as we would still want to link the measured pulses with the GPS location and preferably, we would like to receive a live feed of the measurements. The bandwidth to send the output of the list mode would be a significant obstacle but might be interesting for future research.

Some standard functions we will need on an MCA are energy calibration, defining a region of interest (ROI), gross and net area, centroid of the peak, full width half maximum (FWHM) and full width tenth maximum (FWTM). The energy calibration we can use to assign the channels to an energy range. For this we require a measurement with a known gamma energy. A ROI is a defined range of channels normally enclosing a peak. The ROI allows us to calculate the characteristics of the peak. The centroid and total amount of counts and the number of counts without background are parameters that are calculated. Two parameters that are important to define a resolution are the FWHM and the FWTM. Their definition can be seen in Figure 17 [22], [23], [53].

A digital pulse processing system is the digital equivalent of an amplifier. It still needs a preamplifier but the pulse processing happens in an entirely different manner. As a standard analog amplifier uses gaussian or triangular shapers, a digital pulse processing system will use a trapezoidal pulse filter as is shown in Figure 18, it is also dependent on two separate time constants, the flat top width and the rise time. There are several advantages of using a digital amplifier. There is neglectable temperature drift because of the digitization, the throughput can be increased significantly while keeping an improved resolution and there is less peak shift due to high count rates [22], [23], [53].

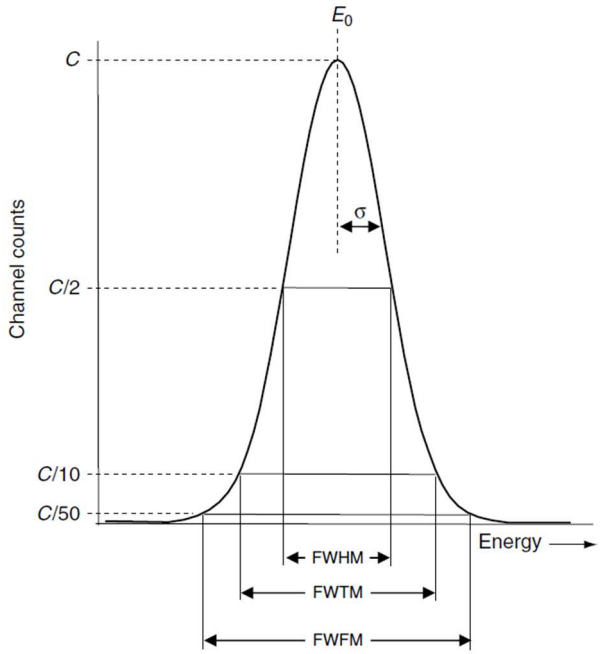

Figure 17: The definition of the Full Width Half Maximum (FWHM), Full Width Tenth Maximum (FWTM), Full Width Fiftieth Maximum (FWFM) [22].

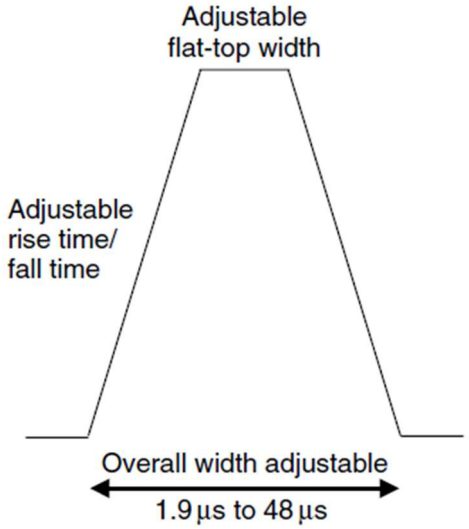

Figure 18: Triangular (Trapezoidal) pulse filter used in digital pulse analysers [23].

1.3.5 Spectroscopy

The first steps in using a spectrometry detector are calibration steps. The three main calibrations that are required are the energy calibration, the efficiency calibration and the peak width calibration. Each has their specific usage and will be discussed.

An energy calibration is always necessary when gain or shaping time constants are adapted. The energy calibration links the channels or bins to their respective gamma energy. The calibration is fairly simple. We only require a detector system, a computer as a readout device and one or multiple known sources with a known gamma energy. After one or several measurements we can link the centroids of the peaks with their known energies. The energy per channel is then reconfigured to match the channel to the correct energy. When the energy shifts due to changes in gain or configuration a new energy calibration is necessary. Information on the gamma ray energies can be found at a multitude of sites and databases such as 'Labratoire National Henry Becquerel' [61] or 'IAEA nuclidechart' [62]. Often the energy calibration gives a linear correlation which is more than accurate enough for most practical cases.

A peak width calibration can happen with the data collected for the energy calibration after the energy calibration. The peak width calibration is used to evaluate the FWHM in function of the energy. This way we can check for errors, double peaks disguised as one peak and possibly debug issues with measurements.

The efficiency calibration is one of the key calibrations for activity measurements in laboratories. For energy and peak width calibrations we only require sources with known gamma energies. For efficiency calibration we need both the gamma energies and the activity of the source. The efficiency we are measuring in this calibration is the full energy peak efficiency. It compares the peak area at a specific energy and compares it to the theoretical number of gamma rays that was emitted by the source, therefore it is strongly dependent on the source-detector geometry. Using an efficiency curve we can calculate the activity of an unknown source. However, we have to keep in mind that the source-detector geometry should remain the same. When the objective is to measure volume sources, the efficiency calibration should happen with the same or at least similar volumes to be able to get activity measurements from the recorded spectra.

1.3.6 In-situ Concentration Measurements

UAVs have the capability to characterise large areas in relatively short time frames. The spatial resolution of the characterisation depends on the flight height, flight speed, detector system, trajectory, spacing of the flightlines and topography. Following Duval et al. and Pitkin et al., a higher flight height reduces the resolution as the circle of investigation is increased, a higher flight speed elongates the area that is measured [63], [64]. The same effect takes place when the detector system's measurement time is prolonged. The measurement will be

integrated over a longer time and area, reducing the spatial resolution. However, this does increase the number of counts in a single spectrum which might be required to identify nuclides. The measurement time should be set to the minimum value as summing can be done in postprocessing. A more complex topography will reduce the spatial resolution as it is difficult to distinguish the origin of the measured gamma rays.

UAV measurements can measure ground concentrations of areas under investigation. However, it requires a good characterisation of the detector, the flightpath and the topography of the ground. It also requires a good understanding of gamma ray spectrometry and the effects of other energies on the energy peaks that are used to calculate the concentration. The method explained by Beck et al. [65] and the IAEA [13], [66], [67] is explained in detail in chapter 3.1.2.8 and derived in annex 8.5. However, the effects of topography should not be underestimated. Ishizaki et al. explains how the topography influences the fluence rate and proposes a relatively simple model to account for height differences [68]. Van der Veeke et al. shows how radionuclide concentrations can be extracted from in-situ measurements with UAVs. Van der Veeke specifically measured K-40, U-238 and Th-232 concentrations, the results are shown in Figure 19 [16]. The measurements were done at 80 cm height and 20 m height. The three detectors were the MS-2000 Agri detector (12 kg), the MS-1000 Drone-borne detector (7 kg) and the MS-350 Ultralight drone detector (2.2 kg). These systems contain a 2000 ml CsI(Na), 1000 ml CsI(Tl) and a 350 ml CsI(Tl) scintillation crystal, respectively [16].

Van der Veeke et al. did not specify the reason for the use of the three detector systems from Medusa Radiometrics or why they chose CsI(Na) scintillation detectors [15], [16]. A better detector material or geometry could improve the sensitivity of the detector system without altering the weight of the detector system. For measurements at larger altitudes the sensitivity will be reduced significantly due to the effects of attenuation.

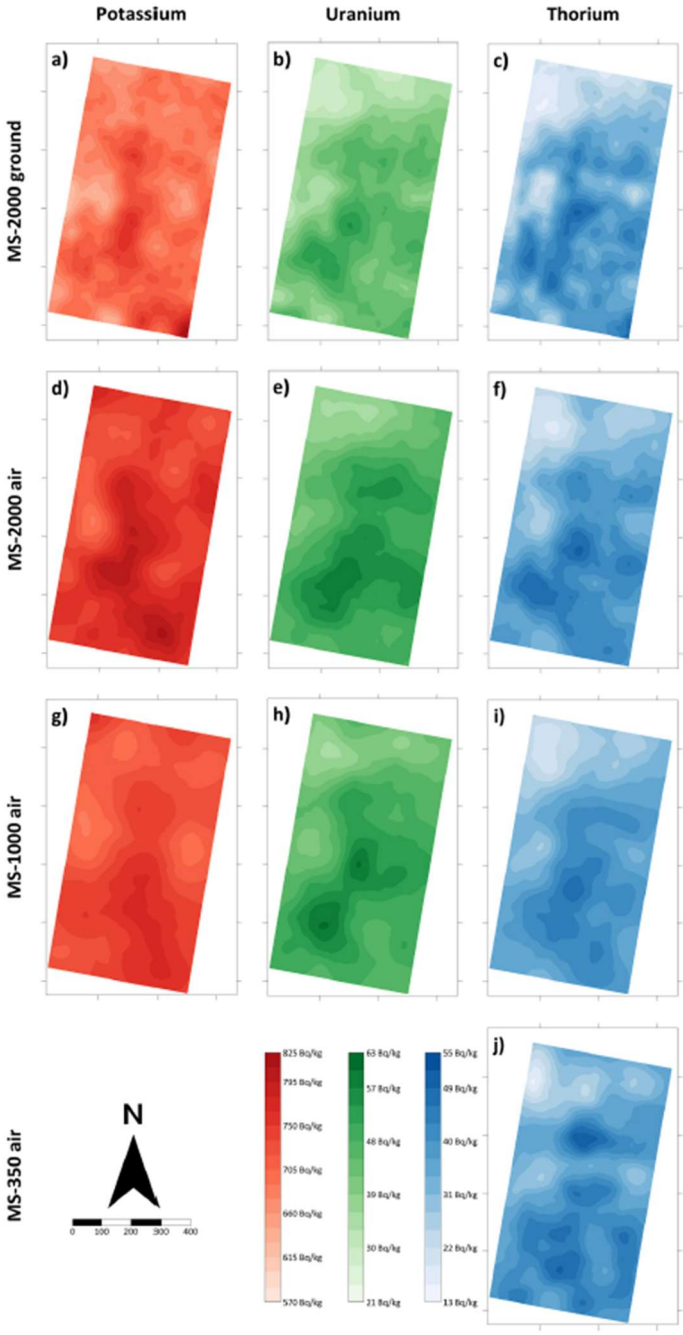

Figure 19: Measurements from Van Der Veeke et al. showing the concentrations of potassium-40, Thorium-232 and Uranium-238. The measurements were done with varying detector systems and heights (80 cm referred as ground and 20 m referred as air) [16].

1.3.7 Directional Detectors

Multicopter drones can move precisely in all three directions which allows us to create detailed maps of an environment. However, in scenarios where radiation is originating from multiple directions it is difficult to distinguish which sources and concentrations are being measured and where they are originating from. To reduce the effects of radiation coming from other sources we can implement directional detectors to supplement the precise movement of multicopter drones.

Directional detectors can be constructed in three ways. The first way uses collimators to shield the detector system from other directions. The second way uses multiple detectors placed in a configuration that makes them shield each other from the radiation. The third way is the use of a Compton camera. A Compton camera uses a pixelized detector to calculate the direction the gamma radiation is originating from [53], [69].

Each method has its own advantages and disadvantages. A collimator adds dead weight to the detector system which causes the flight time of the drone to be drastically reduced. However the directionality of the entire system can be created as is needed with relatively low costs by manufacturing different collimators for the situation. The multiple detectors have an initial cost that is significantly larger than the collimator, however, there is no dead weight, as the shielding detectors can be used to measure in other directions. Additionally we can combine all detector outputs to obtain one larger detector for higher FEP efficiency depending on the situation. With a Compton camera, collimators can be used to further improve the spatial resolution. However, for UAVs this type of system is less useful as it requires the system to remain stationary for long periods of time.

The idea of mounting directional detectors under UAVs is already proven to work by Chen et al. [70] and Carr et al. [71]. And other papers, Willis et al., Schemm et al. and Curtis et al. [72-74] provided us with calibration methods and directional car-borne measurements. However, it is adamant that the direction of the detector system and the direction of the UAV are correct. Errors in one of them will shift the angle that the source is assumed to be. Although the system of Schemm et al. [72] was not used in the field, they did provide a calibration method using a point source revolving their directional detector system, the results of this method are shown in Figure 20. A similar setup was used to validate our own directional detector system.

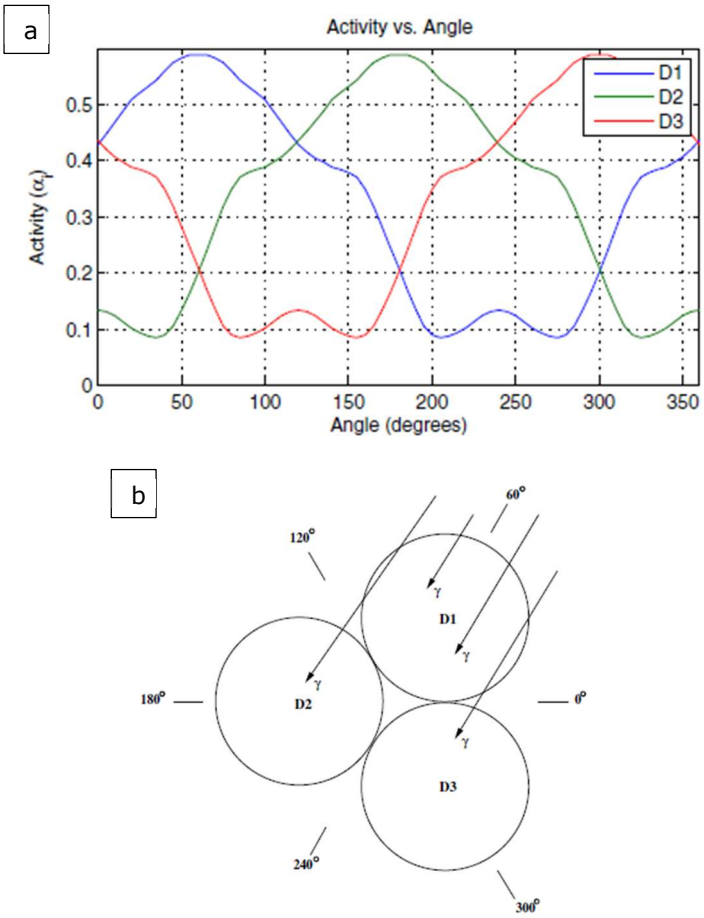

Figure 20: a) Calibration curve and schematic taken from Schemm et al.. A source was placed on different positions around the three detectors. This graph serves as a calibration tool to retrieve angular directions when a source is measured in the field. b) A schematic of the positioning of the detectors [72].

The systems demonstrated by Chen et al. [70] and Carr et al. [71] use different methods for creating directionality. Chen et al. uses multiple detectors to shield each other from the incoming radiation. This has the advantage of a large sensitivity but with eight identical detectors the weight and complexity of such a system can cause issues. Monte Carlo simulations and calculating the directionality will be significantly more complicated. Carr et al. uses a collimator, this adds significant weight to the detector system which causes a decrease in flight time when mounted under a drone. However, it also creates an improved directional resolution as radiation can only pass through the collimator opening. This makes simulating and calculations significantly easier.

A new research question arises from the previous chapters: How can we achieve identification of a nuclear or radiological event and quantification of radioactive

sources using a UAV? The examples given earlier did provide some explanation but it is uncertain whether they can be adapted to work in different radiological or nuclear scenarios and situations. Therefore, it is required to review the possible drone detector combinations as not every type of UAV can easily be combined with each detector system. Furthermore, do we have to consider the efficiency loss of flying at higher altitudes with the possible drone-detector combinations. For multicopter drones the minimum altitude for safe operation is limited to a few meters but for fixed-wing UAVs or unmanned helicopters the required minimum altitude is significantly higher. They are significantly heavier and faster, making possible collisions more dangerous. The next issue we face is the interpretation of the recorded results. They are not linked to one specific point on the ground, meaning that the recorded counts or dose rate is originating from a larger area. For directional detectors similar questions can be constructed: How can we achieve robust directional measurements using a UAV keeping high sensitivity for typical gamma ray energies?

1.3.8 Monte Carlo Simulations

Monte Carlo simulations are used in multiple fields (nuclear physics, finance, business, …). In our context, nuclear physics, we predominantly use it for nuclear particle transport. Monte Carlo simulations use the probability distributions of interaction pathways of the particles together with material and geometry parameters in the model created by the user. The results of the simulations can be adapted by the user. Examples of these results are absorbed dose, energy distributions or shielding calculations.

The probability distribution is used with a pseudo-random number generator to incorporate the principle of random chance in the model. Pseudo-random number generators are algorithms that provide a stream of numbers that appear to be randomly distributed. However, the stream of numbers is dependent on the seed that is provided to the generator. A seed is one or a combination of numbers that is used to create a stream of numbers that appear to be random. The pseudo-random number generators play a significant role in the simulations as they also provide the option to re-run a simulation using the same seed. Running a simulation with exactly the same parameters based on geometry, material and seed will provide the same results. This has the advantage that it can be used to debug strange or skewed results.

Results from a Monte Carlo simulation are coming from a tally. A tally represents a volume or surface in which the interactions and their effects are collected and recorded. In case of a detector model the active volume of the detector will be defined as the tally and the energies that are deposited in this volume will be recorded. The obtained data can then be used for calculating efficiency, dose rate or other characteristics of the detector model.

The response of the physical detector and the Monte Carlo model should be compared over various energies and positions to determine the model's validity. This can be done by iterative adaptations to the model's geometry. However, a

good correlation between the responses of the detector and the model does not necessarily mean that the model's geometry is an accurate representation of the detector. It is possible that by varying multiple parameters, the responses correspond for more than one set of parameters.

Penelope (Penetration and Energy Loss of Positrons and Electrons) [75-78] is a Monte Carlo code for simulations of electron and photon transport. It is written in Fortran and has two main modes, namely Penmain and Pencyl, with the latter being specifically for cylindrical geometries. Penmain can handle more complex and asymmetric geometries. Penelope has a standard material library together with various databases for calculating the interactions that particles and photons undergo. The Monte Carlo code was developed by Josep Sempau, Francesc Salvat and José Fernández-Varea.

The statistics of the simulation, the number of particles simulated and recorded in the tally, must be sufficiently high to reduce the statistical error. Increasing the statistics can be done by running a single simulation over a longer period or by running the code over multiple computer cores, which is also known as parallelization. Since Penelope does not provide parallelization of its code, extremely long simulations would be necessary. However, by using different random number generator seeds we can statistically combine multiple instances of the code. This technique is also known as a poor man's parallelization.

Variance reduction is a collection of techniques that can reduce the simulation time significantly. A clear example of such a technique is the use of geometry settings to reduce the number of particles that have no or only a small chance of interacting with the active volume. Those particles do not contribute to the statistics and waste time and resources. An important comment on this technique is the possible bias. If the assumption that the excluded particles will not interact with the active volume is wrong, the tally will misrepresent the actual dose rate or spectrum. This issue can be avoided by running a shorter simulation with and without this reduction and comparing both results. If there is no significant difference between both results the variance reduction technique is safe to be used.

In the simulations performed in this thesis, Penelope in the penmain mode was used. Both impact and energy deposition tallies were used depending on the objective of the simulation. The time consumption of the simulations became an issue when the geometry became more complex. Examples of increased complexity are increase of the source to detector distance, shielding and scattering caused by different materials, variations in the topography of the area or a heterogeneously distributed source.

1.4 Research Objectives

1. How could UAVs contribute to the acquisition of basic information (dose rate, count rate, …) by the first responders in a nuclear or radiological emergency scenario?

- Which types of detector systems can be used for assessing the dose rate distribution?
- How can UAV measurements be converted to useful information?
- What can we learn from in-depth field-testing?

2. How can we achieve identification and quantification of radioactive sources in case of a nuclear or radiological event using a UAV?

- What would be a good drone-detector combination for these purposes?
- How can we optimize the detection system?
- What considerations or methods should be followed when interpreting the results of measurements done with such a system?
- How can we demonstrate such systems in non-emergency situations?

3. How can we achieve detailed and robust measurements using a UAV, including directional measurements while keeping high sensitivity for typical gamma ray energies?

- What detector configuration can be used to achieve directional measurements while remaining within the limitations of the UAV?
- What considerations, procedures and methods should be followed when interpreting the results of measurements done with such a system?

From these questions we can create the objectives and sub-objectives that we will require to answer the aforementioned research questions.

The first objective **(1)** is to identify an appropriate detector system for UAV assisted dose rate measurements. The method for this goal is to perform a measurement campaign concerning a typical radiological or nuclear scenario for first responders where UAVs assist in the dose rate characterisation of an area of investigation. As first sub-objective **(1a)** we want to use the results from this campaign to investigate different dose rate detector systems to determine their individual advantages and disadvantages. As second sub-objective **(1b)**, a comparison of the results is needed to provide recommendations regarding dose rates measured by UAVs with the aim of assisting first responders.

The second objective **(2)** is to develop a drone-detector system for large area surveillance and long endurance flights to measure, identify and quantify radiological and nuclear sources or contaminations. The main variables are the UAV's maximum payload weight, the UAV's minimum flight height, the detector geometry, the detector materials, the source geometry and the sources gamma ray energies. The detector system is the easiest variable to adapt while maintaining the limitations of the UAV and the source. The first sub-objective **(2a)** from this research question is to optimize the detector system for detector material and geometry using Monte Carlo simulations [75-78]. Additional parameters for these simulations are the maximum weight the UAV can handle as payload, the minimum flight height and the gamma ray energies emitted by the source. The second sub-objective **(2b)** is to show that the UAV-detector combination works for emergency scenarios by demonstrating it in a sufficiently complex non-emergency scenario.

While objective (2) is focussing on achieving a broad overview over large areas, objective (3) is focussed on more precise and localised measurements. To achieve this precision and sensitivity we choose to develop a directional detector system. Therefore, the third and final objective **(3)** is to develop a robust directional detector system that can be used with a UAV while keeping a high sensitivity for typical gamma ray energies. The typical gamma energies are between 30 keV up to 3 MeV. The requirement of 'keeping a high sensitivity for all gamma ray energies' eliminates the use of collimators or standard shielding. Therefore, the first sub-objective **(3a)** is to find and create an implementation of a directional detector system that does not use shielding or collimation in ways that makes us lose directional information. The second sub-objective **(3b)** is to create a robust algorithm to interpret the results coming from the directional detector system. This algorithm will have to take into account the position of the UAV relative to the north and the position of the detector system relative to the UAV.

Chapter 2 was split into two subchapters. The first subchapter, 2.1, explains how objective 1 was executed with a measurement campaign using the 6150AD-b. The second subchapter, 2.2, explains how the same campaign was done with the RadDetecTIF to make a comparison of both systems. RadDetecTIF stands for Radiation Detection and Transmission In Flight and is a detector system that uses a CsI detector. It can run independently and transmits the live measurement to a ground control station As an area of investigation the D1 site at Umicore Olen was chosen. The measurement campaign was done in cooperation with Umicore Olen

and the civil protection of Belgium. For sub-objective 1a, the comparison was done between the standard 6150AD-b dose rate detector and a self-made scintillation detector system called RadDetecTIF. More information on the 6150AD-b and RadDetecTIF can be found in chapters 2.1.3.1 and 2.2.2.1 respectively. In the conclusions, chapters 2.1.6 and 2.2.4, sub-objective 1b is accomplished by giving recommendations for dose rate measurements using UAVs.

In Chapter 3.1 we describe how the drone-detector system, mentioned in objective 2, was designed, tested and verified. Chapter 3.1 shows how sub-objective 2a was achieved by using Monte Carlo simulations. The simulation parameters were selected so they would adhere to the preestablished limits for the detector and UAV. Objective 2b was accomplished by flying over several fields to measure the K-40 concentration at flights over 100 m in height. The results were verified by comparing the concentrations with the concentrations measured in samples taken from the fields. A second UAV measurement was done over the area of the SCK CEN, the specifics of this measurement are discussed in section 3.2.1.5. The regulated Argon-41 releases of the BR1 (Belgian Reactor 1) at the SCK CEN provide an interesting and sufficiently complex scenario to prove whether the system works as a whole in nuclear or radiological scenarios. Both measurements sufficiently prove objective 2b to be accomplished.

Chapter 4 handles objective 3 and its sub-objectives. In chapter 4.1, we provided the initial testing and construction of the detector system with all required settings. This concludes sub-objective 3a. The next chapter, 4.2, explains the directional algorithm and shows measurements in the field with this algorithm implemented, accomplishing sub-objective 3b.

To help the reader in understanding the different detector systems and their measurement campaigns, an overview of the detector systems, UAV platforms, measurement campaigns and in which chapter of the thesis this is handled is provided in Table 3.

Table 3: Overview of the different detector systems and UAVs with their respective measurement campaigns and the chapters they are explained in.

Detector System	UAV	Measurement Campaign	Chapter
6150AD-b	DJI M600	Cs-137 point source	2.1.4.1
6150AD-b	DJI M600	Umicore D1 site	2.1.4.2
RadDetecTIF	DJI M600	Umicore D1 site	2.2.3
Fixed-wing detector	Penguin C	Droneport Sint-Truiden	3.1.3
Fixed-wing detector	Penguin C	SCK CEN and surroundings	3.2.2
Directional detector	/	Ar-41 plume from BR1	4.2.3.1
Directional detector	SABCA X8	Cs-137 point source	4.2.3.2

2 Drone-Borne Dosimetry

It is possible to divide drone-borne radiological monitoring into three distinct categories. The first one is drone-borne dosimetry, entailing the collection of dosimetry readings over a point or area of interest. The results of these types of measurements are heavily dependent on the type and definition of the dosimetry unit [79]. Chapter 2 focuses on drone-borne dosimetry. A second category is drone-borne spectroscopy. The data obtained from this category are far more detailed and information dense as dosimetry measurements. However, it is again heavily dependent on detector shape and material. It is possible to condense the collected data of a spectroscopy measurement into a dosimetric quantity, although this requires extensive calibration. Chapter 3 will focus more on drone-borne spectroscopy. A third category is drone-borne sampling. As the name suggests, this method sends out a drone to multiple points and returns with air, ground or water samples. This last method is not further explored in this thesis but would result in more detailed and localized results.

The first part of the current chapter is published under the title 'Drone-borne dosimetry in a radiological or nuclear scenario' in the Journal for Radiation Measurements [80]. As indicated, it covers drone-borne dosimetry and compares historic ground measurements with their drone-borne counterparts.

The second part includes additional measurements done with the RadDetecTIF detector system [81] over the same area as in chapter 2.1. This part will also go further in depth on the advantages and disadvantages of spectroscopy detectors for dose rate measurements, including stripping as a conversion method to achieve dose rates.

2.1 Drone-Borne Dosimetry in a Radiological or Nuclear Scenario: 6150AD-b

2.1.1 Abstract

This paper describes the drone-borne dosimetry performed in two separate case studies. Two drone measurements were performed using a reference dose rate detector measuring the ambient dose equivalent rate. A first flight was used to obtain reference measurements using a cesium-137 point source and flying at multiple speeds and different heights. A second flight was performed above the D1 radium-containing waste deposit of Umicore in Olen, Belgium. The main objective of this flight was to perform a scanning pattern over the area to create a dose rate map. After the flights, we used historic measurements and a dose rate model verified by Monte Carlo simulations using Penelope to verify the dose rate measurements performed by the drone. Finally, we used the findings from both flights to provide recommendations regarding drone measurements using dose rate detectors.

2.1.2 Introduction

During an emergency situation, drones can support first responders. Drones have the capabilities to create an overview of the emergency [4], [12], [82]. The payload, the system mounted under or on the drone, is most often a camera but can be adapted to serve the specific emergency situation [13], [59], [83-86] for example, a spot-light can be used in a search and rescue scenario, or an infrared camera for detecting fire hazards. In case of a radiological or nuclear scenario, it is important for the first responders to have information on what dose rates they are facing and where they are located.

Radiation protection plays an important role in emergency scenarios. First responders are trained to receive doses that are As Low As Reasonably Achievable (ALARA). The ALARA principle can be achieved using three topics. The first topic is time, attempt to reduce the time of exposure. This can be done by training in safe scenarios or by limiting the allotted time in which the first responder can be exposed. The second topic is shielding. By using shielding materials that are practical and useful for the type of radiation, the received dose rate can be reduced or even completely removed. However, this might increase the required time the first responders are in the radiation zone, which causes an increase in received dose. The third topic is distance. Radiation diminishes following an inverse-square law. Therefore, by doubling the distance to the radiation source, the received dose will be divided by four. However, in case of ground contaminations, the inverse-square law is not always applicable due to the specific geometry.

Dose rates can be obtained by handheld devices requiring an operator that will be put at risk of receiving a high dose. In addition, the measurement can be influenced by operator shielding effects [48], [49]. Furthermore, to screen larger and hard-to-reach areas the measurements take longer. However, a dose rate detector mounted under a drone or Unmanned Aerial Vehicle (UAV) would solve this problem since the drone pilot can be at a safe distance from the measurement site and the drone can cover larger areas in a shorter period of time. Therefore, a drone-based measurement strategy supports the implementation of the ALARA principle.

The combined advantage of efficient area coverage and increased operator safety has been readily confirmed by studies in Chernobyl and Fukushima Daiichi [14], [17], [18], [44], [49], [87-89] both with dose rate detectors and spectroscopic detectors. These papers show how the dose rate data can be interpreted in various scenarios like remediation, monitoring, hotspot localization or perimeter placement.

It is also possible to convert spectral data, coming from a spectroscopic detector, to a dose rate by a stripping method [33-36], [90] a technique that uses mono-energetic sources and their respective dose rates to create bins with a dose rate weighting factor. The bins can then be used to convert any spectrum to a dose

rate by multiplying the weighting factor of the bin by the count-rate in the bin. The stripping method is explained in more detail in chapter 2.2.2.2.

The dose rate gives a general idea of the activity of the area and reduces complexity of the measurement data. It is also a decent indicator for remediation efforts as shown by Cresswell et al., Yukihisa et al. and Martin et al. [46], [47], [87], [91].. Cresswell et al. showed the reduction in dose rate before, after and at stages during an experimental remediation campaign of a contaminated forest in the aftermath of the Fukushima accident. Evaluating remediation efforts requires measurements before and after the remediation. The measurements are easy to reproduce using drones with the same programmed flightpath which improves the fidelity of the comparison. This is clearly shown in Cresswell et al. [47], where the change in dose rate is visualized by subtracting the dose rate after remediation from the initial dose rate.

The cases of Chernobyl and Fukushima Daiichi are excellent candidates for performing surface contamination studies. However, to establish a baseline for the measurement system it is instructive to first use calibrated point sources to validate the results. Gabrlik and Lazna [92] used several cesium-137 (Cs-137) point sources to map an area using both a UAV and a UGV.

A noteworthy observation from their findings is the significant impact of the relative source activity compared to the background. When the source is too weak or the background too high, discerning the source from the surroundings becomes challenging and even impossible. The second variable to consider is the height of the drone above ground level (AGL). As the drone's flight height increases, the detector receives a weaker signal, primarily due to the inverse-square law. However, in the case of a relatively large homogenous surface contamination this effect is reduced [92].

The measured dose rate can then be used to create a dose rate map to identify hotspots. In the current paper, the performance of drone-based dose rate mapping is evaluated in two different scenarios using a multicopter drone DJI M600 Pro [93], [94].In the first scenario, a Cs-137 point source is mapped, while in the second scenario the larger area of a radium-226 (Ra-226) residue storage site (Umicore Olen, site D1) is investigated.

During the first scenario, we evaluate the optimal flight parameters for future flights with a focus on speed and altitude. The second scenario is meant as a 'proof of concept' study and combines historical ground measurements with the dose rates obtained by the drone. The current study combines field experiments with a dose rate reference instrument with Monte Carlo simulations to deduce practical guidelines related to flight planning, detector use and overall deployability. The objective of this study is to assess the capabilities of a standard dose rate detector, mounted under a drone, to detect point sources and hotspots in emergency situations to aid the first responders on the ground.

2.1.3 Method and Materials

2.1.3.1 Automess 6150AD-b

The dose rate detector we used is the Automess 6150AD with the 'b'-probe (6150AD-b) [30-32]. This is a 3 inch by 3 inch cylindrical PVT (Poly Vinyl Toluene) scintillation probe sensitive to small variations in levels around ambient background and calibrated for ambient dose equivalent H*(10). The 6150AD-b is an often-used detector in the case of emergency response because it has a high sensitivity and is easy to operate. For higher dose rates the Automess 6150AD, without the 'b'-probe, can be used since it has an internal Geiger counter. The 6150AD-b detector has an energy response that deviates less than 20% for energies between 50 keV and 7 MeV, as can be seen in Figure 21. The angular response is assumed to be 1 with only slight variations for energies between 50 keV and 7 MeV according to the datasheet [30-32].

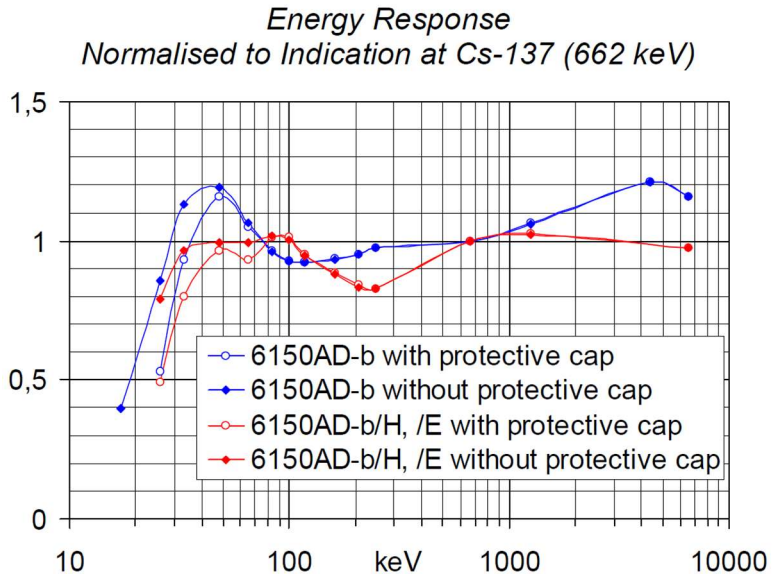

Figure 21: Energy response of the Automess 6150AD-b [30-32].

The detector uses a time constant of 8 s to give a stable dose rate [30-32], this means that after 8 s the detector will output 68% of the measured dose rate. However, when large changes in dose rates are noticed, the time constant is disregarded in the analysis and it is assumed that the detector immediately rises or falls to the new value. For drone measurements we assume that the given dose rates are an immediate response in case of a peak or a constant value for background or relatively constant measurements. In Figure 22, the effect of a point source (black dots) and a surface source (red dots) on the normalized ambient dose equivalent rate are visible. Both flights are at approximately the same speed, 2.0 - 2.5 m/s. The flight was directly above the point source and

over the maximum of the surface contamination. The gradual increase for the surface source creates a less steep peak compared to the point source.

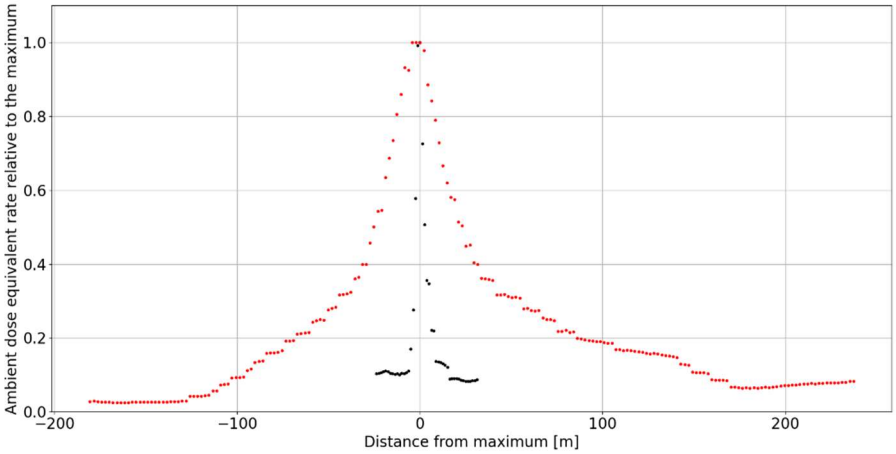

Figure 22: Comparison of the normalized dose rate profile of a point source (black) and a surface source (red).

2.1.3.2 Mounting the Payload

The detector was not built for being mounted under a drone. A 1-mm-thick aluminium connection plate was made that could be mounted under the frame of the drone and 14 holes were drilled to allow industrial zip ties to fix the detector in place. The view of the plate is illustrated in Figure 23.

Figure 23: Mounting plate for securing the 6150AD-b to a DJI M600 (UAV).

2.1.3.3 Communication

The detector has an attachable Bluetooth module to transmit, every second, the measured dose rate. A smartphone application was made to record the dose rate and store the data in a text file combining the (smartphone) GPS-location, time and dose rate. The smartphone is a Samsung Galaxy A8 with Android 8 operating

system. However, the GPS data from the drone instead of from the smartphone are used in the post-processing of the data to improve the location accuracy.

2.1.3.4 Bluetooth Application

We created an Android app written in JavaScript using Android Studio, an IDE specific for creating applications for Android devices. The app creates a connection between the Bluetooth module of the 6150AD-b and the smartphone through Bluetooth. In post processing the GPS-coordinates of the smartphone will be substituted by those from the drone, as its GPS is significantly more accurate as the one from the smartphone. The smartphone was placed in a runner's brace which was fixed around the 6150AD-b. It would be possible to create a live feed with this setup by logging the obtained data on a server or cloud document. We did not choose to do this since this would require an internet connection that could potentially interfere with the connection between the drone and the remote. Figure 24 is a screenshot of the app.

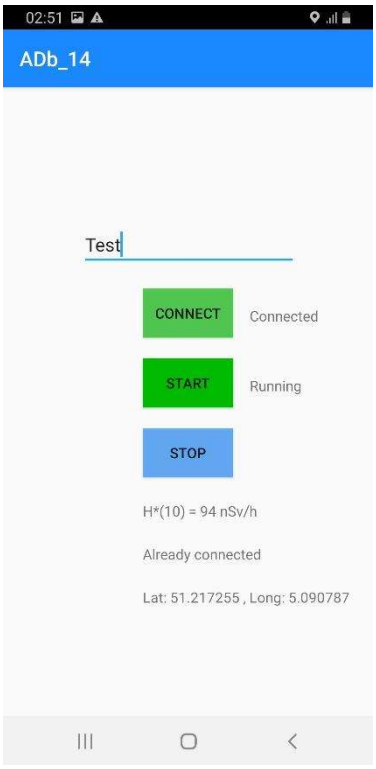

Figure 24: Android application for recording the dose rate values received from the Bluetooth module of the 6150AD-b.

2.1.3.5 DJI M600 Pro

The DJI M600 Pro, shown in Figure 25, is a multicopter drone with six propellers, which can carry a maximal payload of 5.5 kg. The maximum take-off weight is 15.5 kg and the drone has a diameter of 1.67 m with the arms folded out. The

DJI M600 Pro is equipped with an A3 Pro flight control system. The GPS-module of the drone can obtain an accuracy of 1.5 m horizontally and 0.5 m in height [93], [94]. However, this also depends heavily on weather conditions and satellite coverage. For flights without payload, the drone can fly up to 38 min in good weather conditions. However, the flight time is reduced significantly for heavier payloads, for example down to 18 min when using a 5.5 kg payload. The weight of the payload containing the Automess 6150AD-b and the smartphone is 2.9 kg, resulting in a flight time of approximately 25 min. Combining a common multicopter drone and a common and robust dose rate instrument demonstrates that basic radiological monitoring using drones can be quickly and easily set-up and is in reach of many first responders involved in nuclear or radiological emergency management.

Figure 25: DJI M600 Pro with the Automess 6150AD-b payload (including smartphone and Bluetooth module) underneath.

2.1.3.6 Cs-137 Point Source

The point source measurements were performed on a field on the domain of the Belgian Nuclear Research Centre (SCK CEN). A first flight was performed to obtain a background reading, followed by several flights in which important flight parameters (speed and height) were systematically altered: speeds of the flights were 1, 2 and 5 m/s and drone altitudes were fixed to 2, 5 and 10 m. Every flight consisted of parallel flight tracks over the source in two perpendicular directions with a line spacing of 5 m. By flying two times in perpendicular directions we improved the spatial resolution of the dose rate data. A final measurement was done by varying the altitude while hovering over the point source. The Cs-137/Ba-137m point source has one gamma ray peak at 662 keV with an emission probability of 85 % [61]. As calibration, a measurement at 1.00 m source-detector distance was done, resulting in a dose rate of 5250 nSv/h.

2.1.3.7 Radium Waste Site

Umicore, formerly known as Union Minière, used to process uranium and radium ores for the production of radium sources. It also handled the processing of other metals like cobalt. The processing steps of the ores and production of radium created a radiological waste stream that has been stored in the waste storage facility UMTRAP (Uranium Mill Tailings Remedial Action Project). Due to the production processes during 1920-1969, the riverbanks of the river Bankloop have been contaminated. Between 2006 and 2008, it was remediated and the contaminated soil was placed in a second waste storage facility. The D1 storage from Umicore Olen is a historically contaminated site. It was used to store the waste from the radium source production and radium ore processing. It measures 275 m by 450 m and has a surface area of approximately 0.1 km². The radiological contamination present is radium-226 and its daughters. The gamma rays produced by these nuclides with a gamma probability above 5% are listed in Table 4. The Automess 6150AD-b is equipped with an aluminium cap on the front to protect the PVT plastic scintillator from rain and damage, aside from protection it can shield the scintillator from beta-radiation. Removing the aluminium cap would not make a significant difference since the PVT plastic scintillator is also encased in a plastic cover blocking any alpha radiation coming from radon and its daughters.

In 1991, ground measurements were performed with an Automess AD-b on a 25 m grid over the complete area. A smaller grid was not possible due to the dense vegetation present at the site. The measured dose rates at a height of 0.5 m have significant variations due to the very heterogeneous distribution of Ra-226 in the soil [51], [95], [96], giving a distorted view of the actual dose rate in the 25 by 25 m area, this is visible in Figure 26a. The originally measured dose rates are depicted in Figure 27 as a 3D bar plot. We took the Lambert 72 coordinates from the south-west corner as reference point for the figures and used a median filter, with a mask size of 2, to reduce the effects of the local maxima, producing Figure 26b as a result. Median filters are often used in impulse noise filtering and noise reduction because of their robustness against outliers as is the case for the sparse historical measurements shown in Figure 26a [97]. However, this makes it impossible to quantitatively assess the dose rates since the median filter changes the values of the ground measurements. The mask size refers to the size of the area on which the filter is performed for every measurement point. An averaging filter does not work since it spreads out the maxima rather than reducing the influence on neighbouring measurements. In total we have tested three filters (median, Gaussian averaging and uniform) and also the unfiltered ground measurements, with the median filter giving the best approximation to the data measured by the drone.

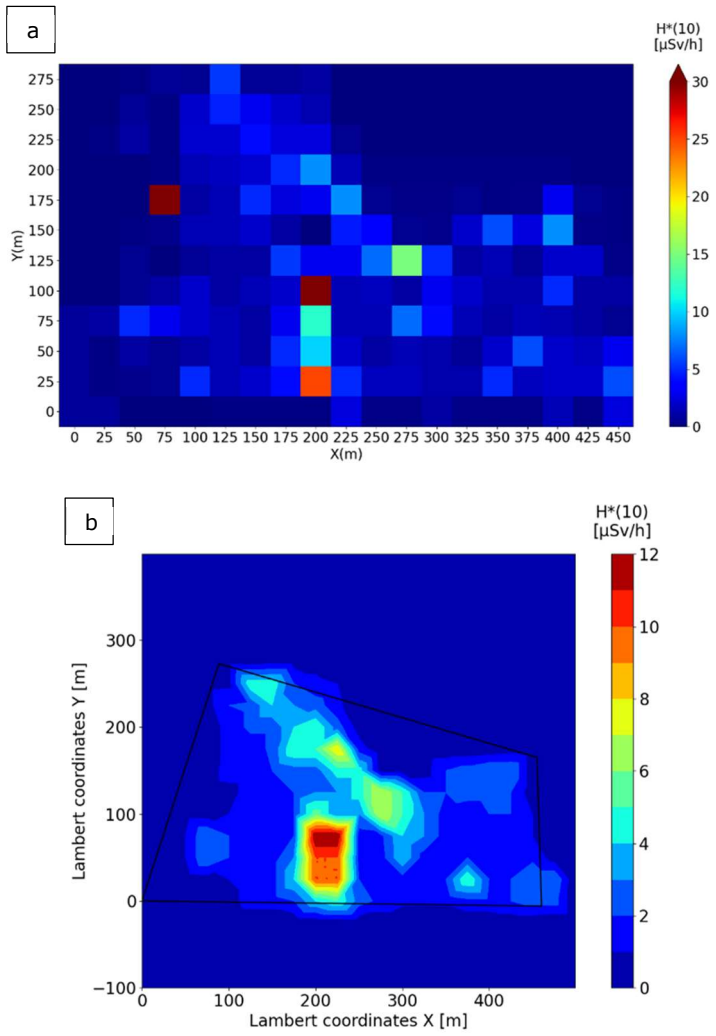

Figure 26: (a) Historical ground level measurements at 0.5 m height expressed in ambient dose equivalent rate (H(10)). The pixels represent a 25 by 25 m square, referring to the grid size of the ground measurements done in 1991 on the D1 site [95], [96]. (b) Ground level measurements at 0.5 m height expressed in ambient dose equivalent rate (H*(10)) with a median filter. The black line represents the fence around the D1 site.*

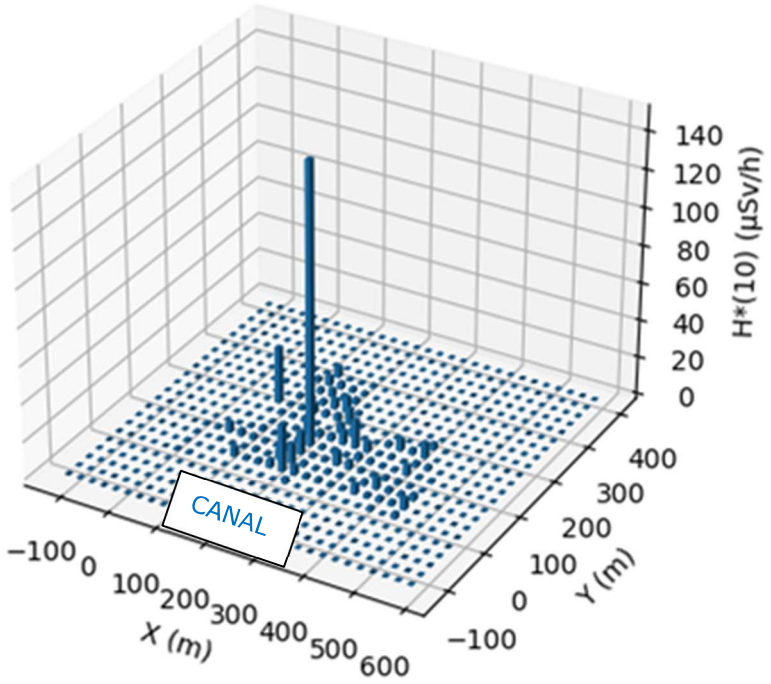

Figure 27: 3D bar plot of the historical data taken in 1991 on the D1 site with a 25 m by 25 m grid size [95], [96].

Another factor with a significant impact on the dose rate measurements on the ground is the presence of radon-222 (Rn-222). Rn-222 is a daughter of Ra-226 and decays through alpha emission with a half-life of 3.82 days [61]. Since it is a noble gas, it will not interact with the environment, making it very mobile and able to escape from the contaminated ground. Measurements have shown that the Rn-222 concentration at the D1 site is 180 Bq/m³ at a height of 1.5 m [95], [96]. At 0.5 m, the radon concentration can be 2-4 times higher. However, because the Automess AD6150-b usually measures dose rates with an aluminium cap, the contribution of the dose caused by radon will be limited to its daughters that produce gamma rays, they are listed in Table 4.

Table 4: Daughters of radium-226 that produce gamma energies with emission probabilities above 5% [61]. This list is also used for the simple dose rate model. The mass attenuation coefficients are taken from the NIST database [25].

Energy (keV)	Emission probability (%)	Nuclide	Mass attenuation coefficient for air (m^{-1})
242.0	7.3	Pb-214	0,144
295.2	18.4	Pb-214	0,133
351.9	35.6	Pb-214	0,125
609.3	45.5	Bi-214	0,099
1120.3	14.9	Bi-214	0,075
1238.1	5.8	Bi-214	0,071
1764.5	15.3	Bi-214	0,059

2.1.3.8 Flight Parameters D1 Site

The flight plan for the D1 storage site is multiple parallel lines forming a scanning pattern. The spacing between these lines is 15 m and they are East-West oriented. Due to battery constraints it was not possible to reduce the spacing below 15 m. The entire flight was flown at a height of 25 m AGL. Due to the dense tree population on the site it was not possible to fly at a lower height without risking the drone hitting any branches. The flight speed was selected to be between 2.0 and 2.5 m/s. The point source measurements still showed decent results with this speed. Lower speeds would cause issues regarding battery usage. While faster speeds would cause streaking effects as can be observed in Figure 39 in the 5 m/s row. The streaking effects mentioned are the elongations of the dose rate contours caused by the time constant of the detector. Afterwards, the time and GPS-location were synchronized with the time, height and GPS-location of the drone to achieve a more accurate position.

2.1.3.9 Dose Rate Model and Monte Carlo Verification

A dose rate model was created using Equation 2 to calculate the ambient dose equivalent rate $\dot{H}^*(10)$.

$$\dot{H}^*(10) = KH\ k\ \frac{\mu_{en}}{\rho_{air}}\ \frac{1}{1-g}\ E_\gamma\ \varepsilon\ \frac{B}{4\,\pi\,r^2}\ e^{-\mu r}\ C \qquad (2)$$

Where, KH stands for the air-kerma to ambient dose equivalent rate $\dot{H}^*(10)$ conversion factors, k is the conversion from eV to J, μ_{en}/ρ_{air} is the mass energy absorption coefficient in cm^2/g, g is the average fraction of the kinetic energy of secondary charged particles, E_γ is the gamma ray energy in eV, ε is the gamma-emission probability, B is the build-up factor for the gamma energy and the mean free path μr, r is the distance between the source and the detector under the drone in m, μ is the mass attenuation coefficient for the gamma energy E_γ expressed in cm^{-1} and C is the point source activity expressed in Bq. The air-kerma to ambient

dose equivalent conversion factors are taken from ICRP74 [28] and the mass energy absorption coefficients from the NIST database [25] together with the factor g. The build-up factors are obtained from the handbook Physics for Radiation Protection [24].

With this model, we can compare the results of drone-borne measurements with the dose rates at ground level. This is especially useful when the environment does not allow for sampling or ground measurements to be executed. Furthermore, we can exclude operator-shielding effects and reduce the total dose that a first responder would obtain during the ground measurements. However, a downside of using drones is the reduction in spatial resolution due to the height they are required to fly at when vegetation or other obstacles are present. When no vegetation is present it is possible to fly at lower heights, giving results similar to what an operator would measure. We used Monte Carlo simulations in Penelope 2018 [75-78], more specifically the penmain package, to obtain theoretical ambient dose equivalent rate values. These are then used to verify the dose rate model described earlier so that future calculations can be carried out quicker and on a larger scale.

Figure 28 shows the results and relative difference of the Monte Carlo simulations with the dose rate model for sources with varying energy, at a distance of 1 m and with a source activity of 2 GBq. On average the simple model over predicts the ambient dose rate with 3,2 % compared to the more detailed Monte Carlo model over the considered energy range. However, assuming a 5 % uncertainty on the simple model, as shown in Figure 35, results in values within the uncertainties of the simulated dose rates. Because a 5 % uncertainty on the calculated ambient dose rate is small compared to the uncertainties in the measurement of the ambient dose rate by a radiation detector, it is justified to use the simple dose model to perform calculations for ambient dose rate.

As a tally, the deposited energy is used. The active volume is a voxel of 1 cm^3 with a centre at a depth of 10 mm in the ICRU sphere. The ICRU sphere is made from a fictive tissue equivalent material with a diameter of 30 cm. The Monte Carlo simulations follow the ICRP 74 [28] definition of ambient dose equivalent rate that states that: *"The ambient dose equivalent, H*(d), at a point in a radiation field is the dose equivalent that would be produced by the corresponding expanded and aligned field in the ICRU sphere at a depth, d, on the radius opposing the direction of the aligned field. The recommended value of d is 10 mm for penetrating radiation and 0.07 mm for low-penetrating radiation".*

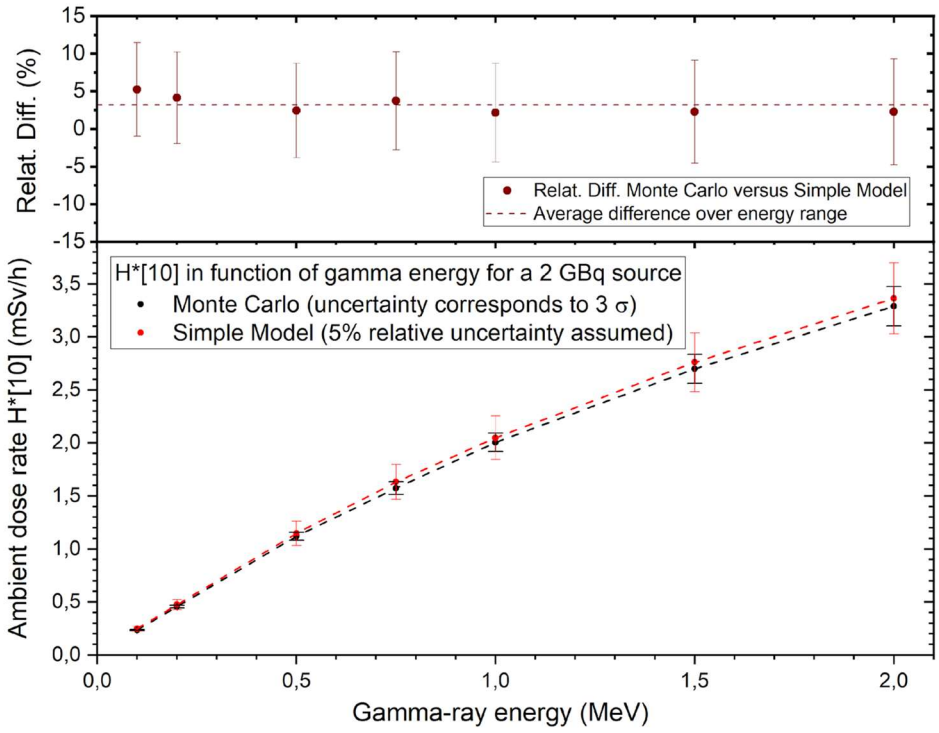

Figure 28: Comparison of the ambient dose equivalent rate calculated with the dose rate model and obtained by Monte Carlo simulations in Penelope using penmain and the ICRP74 definition for ambient dose equivalent rate (H(10)).*

2.1.3.10 Effects of the Time Constant of the 6150AD-b

Our first objective was to verify the detector output of an Automess 6150AD-b. A setup for measuring the dose rate output per second while passing by a Na-22 source at multiple heights was created using a Lego Mindstorm set. We built a small vehicle that drove at a constant speed while carrying the Na-22 source. The results of these measurements are shown in Figure 29 for three detector heights. The sudden jumps between measurements near the source are due to the detector algorithm. It decides that the change in dose rate is too large to continue with averaging over the time constant of 8 seconds and it switches immediately to the new value. The sharp increases agree well to Equation 2, while the parts that are using an average over 8 seconds cause a shift in either direction depending on whether the dose rate is raising or lowering.

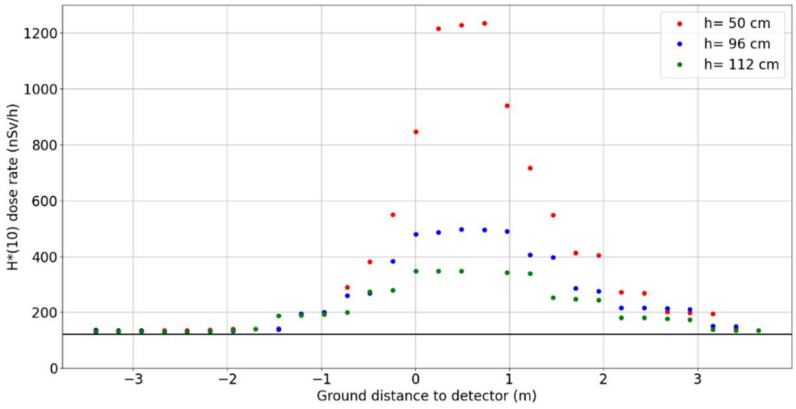

Figure 29: Ambient dose equivalent rate response from the 6150AD-b placed stationary and the Na-22 source moving at a constant speed underneath. The different colours represent the different heights at which the detector was placed.

2.1.4 Results

2.1.4.1 Cs-137 Point Source

In

Figure 31, the dose rate maps of the flights over the point source are shown. The measurements are from two separate perpendicular flights, resulting in a grid pattern, the colormap is created using linear interpolation in QGIS. Figure 30 shows the height AGL in m together with the ambient dose equivalent rate in nSv/h for a height measurement, while attempting to hover over the point source. The variations in dose rate at a fixed height are because the drone cannot hover over the source consistently, resulting in a larger source-detector distance and thereby a lower dose rate.

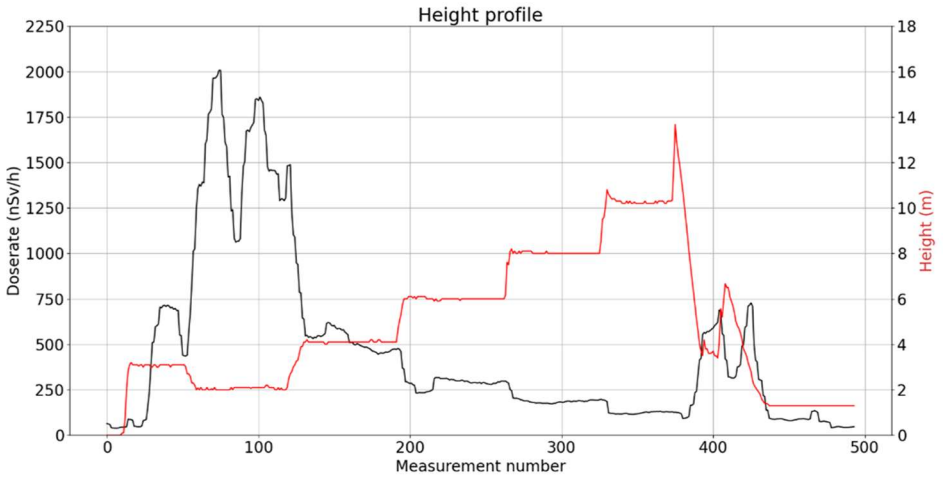

Figure 30: Height measurement while hovering over the point source, the height is the height above ground level. Variations at a constant height are due to the drone not being able to hover exactly above the point source. The dose rate is ambient dose equivalent rate (H(10)).*

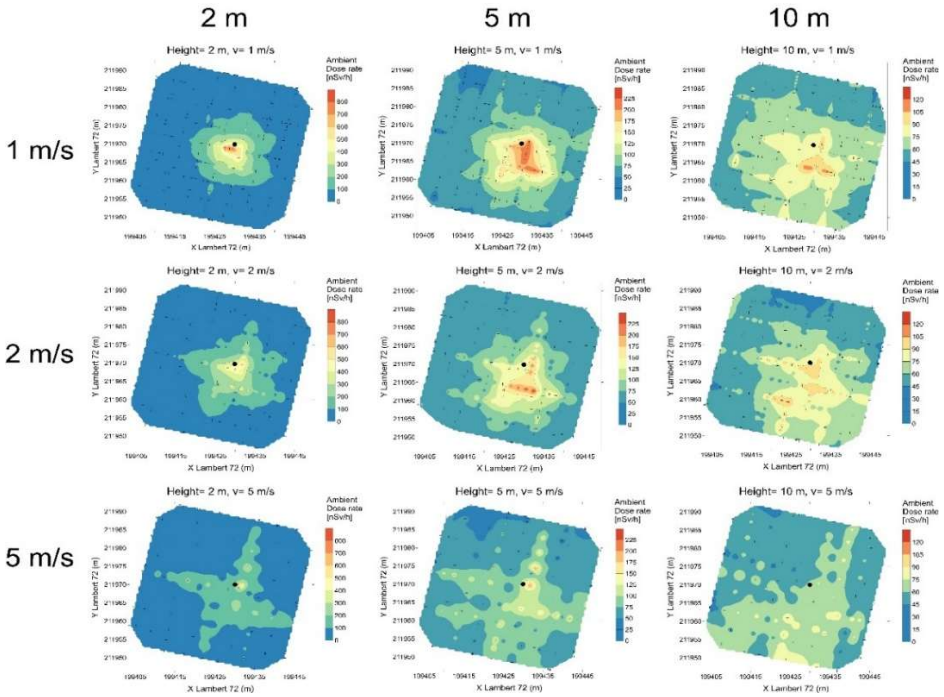

Figure 31: Point source measurements flown at multiple heights and speeds. The black point represents the Cs-137 point source location.

From the Cs-137 point source data in Figure 31, an attempt was made to retrieve activity estimates. The North-South flightline closest to the point source was selected and a curve fit using Equation 2 was done, the fits are visible in Annex 8.1. The curve fit had three variables, i.e. activity, x-coordinate shift and y-coordinate shift. The coordinate shifts were necessary, because the GPS locations of the source and the drone have significant uncertainties. By incorporating the shift in the curve fit, we can couple a value to these uncertainties. An attempt to do the curve fit without the x- and y-shift was done, but this gave worse results, especially for the measurements at 2 m height, as a small shift causes a relatively larger error in source to detector distance. However, it could be argued that for this reason the measurements at 5 m height are superior in activity estimation as they are less sensitive to small positioning errors.

The curve fit is also background corrected for each flight height, 2 m, 5 m and 10 m, giving a background of respectively 51 (6) nSv/h, 34 (2) nSv/h and 44 (1) nSv/h, the values between the brackets are the standard deviations. The curve fits are visible in Annex 8.1, the activities retrieved from these fits are shown in Table 5 together with the R^2 values for each curve fit. The coordinate shifts are shown in Table 12 and Table 13 in Annex 8.1. As reference a measurement at 1 m above the Cs-137 point source was done resulting in an average ambient dose equivalent rate of 5250 nSv/h. Using Equation 2 this gives an activity of 0.933 (0.047) MBq.

Table 5: Activities (MBq) and R^2 (goodness of fit) retrieved from fitting the Cs-137 point source measurements with Equation 2. The columns represent the different speeds and the rows the different altitudes.

A (MBq)	1 m/s	R^2	2 m/s	R^2	5 m/s	R^2
2 m	1.093 (0.069)	0.98	1.435 (0.168)	0.96	3.259 (0.585)	0.94
5 m	1.155 (0.082)	0.96	2.257 (0.215)	0.94	2.214 (0.415)	0.92
10 m	0.932 (0.032)	0.80	1.072 (0.185)	0.81	1.465 (0.494)	0.50

2.1.4.2 Radium Waste Site

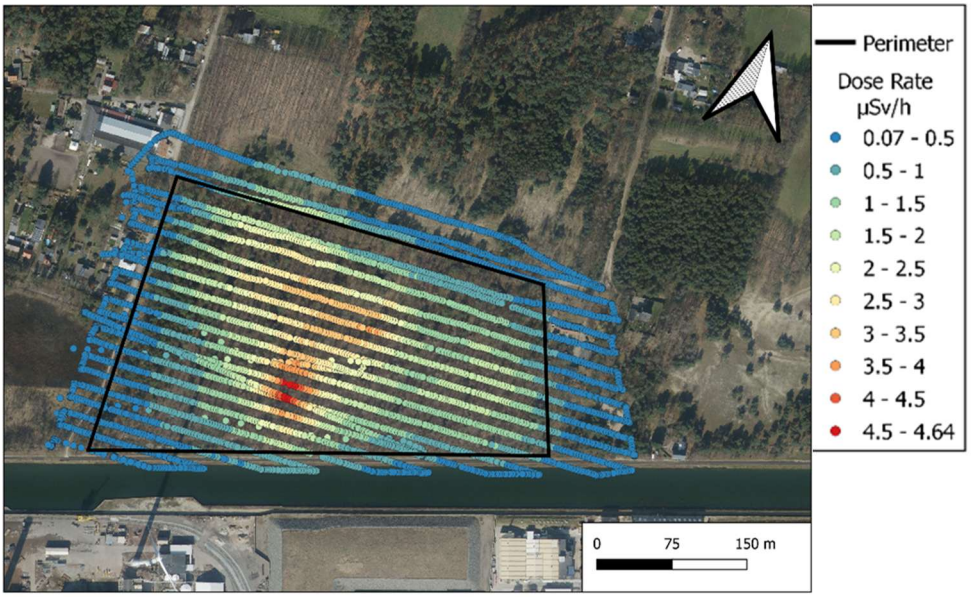

Figure 32: Data points over a satellite image of the D1 site. The colours represent the dose rates measured by the drone at an altitude of 25 m AGL with a speed of 3 m/s. The black line represents the fence around the D1 site.

In Figure 32 the data points for the D1 flight are shown over a 'Geopunt Vlaanderen' satellite image [98] revealing the flight lines and show an important detail, the canal at the south side of the storage site. The large amount of water will cause the dose rates to be lower at the south side because of the large field of view from the detector under the drone. For the ground measurements, this is not the case. For the D1 site, Figure 33a and Figure 33b show a comparison between the normalized dose rate from the drone measurements and the normalized dose rate at 25 m AGL height calculated from the ground level. The latter calculated the dose rate at 25 m using a median filtered dose rate at ground level together with the dose rate model described in section 2.1.3.9. The results using a uniform (averaging) and gaussian filter are also shown as respectively Figure 33c and Figure 33d.

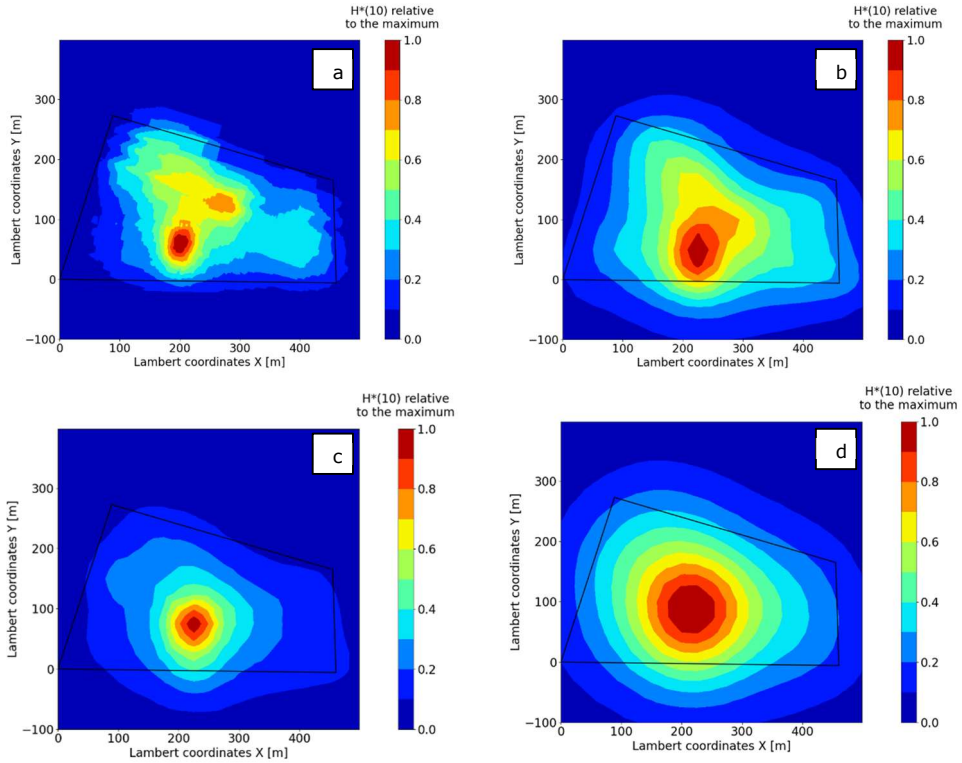

Figure 33: (a) Results from the drone with the dose rate relative to the measured maximum. (b) Calculated dose rate at 25 m by using the dose rate model and the median filtered dose rate measured at 0.5 m with the dose rate relative to the calculated maximum. (c) Calculated dose rate at 25 m by using the dose rate model and the uniform filtered dose rate measured at 0.5 m with the dose rate relative to the calculated maximum. (d) Calculated dose rate at 25 m by using the dose rate model and the gaussian filtered dose rate measured at 0.5 m with the dose rate relative to the calculated maximum. The black line in all figures represents the fence around the D1 site.

The results in Figure 34 show the height in m AGL and the ambient dose equivalent rate in nSv/h. The data can be used in a similar fashion as in Martin et al. and Cresswell et al. [46], [47], [91], with a repeated measurement after remediation. The drone was hovering over the centre of the area at multiple heights. Because the site is relatively large, slight changes in position, when hovering over the centre of the area, will not cause the same erratic behaviour as in Figure 30. Both Martin et al. and Cresswell et al. show drone measurements over contaminated sites around Fukushima Daiichi nuclear power plant. Once before and once after remediation efforts were executed. The comparison of both measurements provides a clear view of the effects of the remediation actions. In Figure 35, the normalised dose rate in function of the drone's altitude is visible. The fit of the results gives us a mass attenuation coefficient. Figure 35 also shows how the

normalised dose rate of the D1 site in function of the drone's altitude can be compared to the ambient dose equivalent rate from a radium-226 point source and a practically infinite radium-226 surface source.

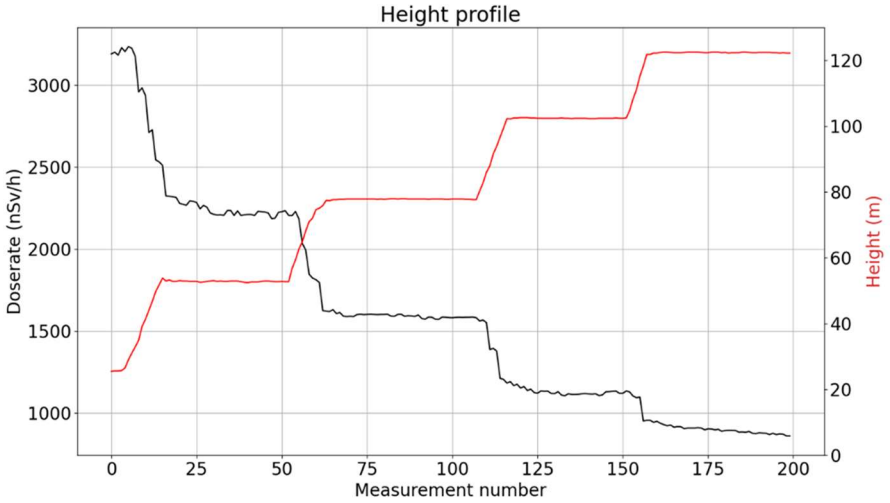

Figure 34: Height measurement while hovering over the maximum measured at the D1 deposit site. The height is the height above ground level and dose rate is ambient dose equivalent rate (H(10)).*

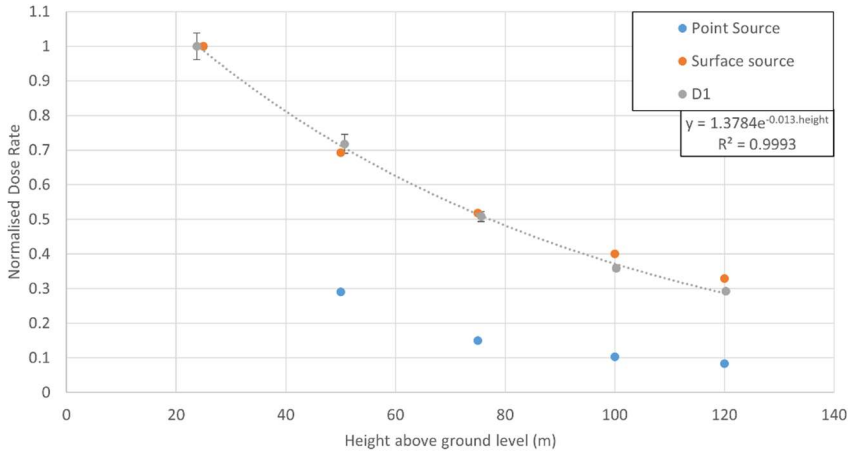

Figure 35: Normalised ambient dose equivalent rate in function of the height of the drone measured during the D1 site measurements are shown in grey. The blue and orange dots represent the theoretical normalised ambient dose equivalent rates for respectively a radium-226 point source and a practically infinite radium-226 surface source. The mass attenuation coefficient from the exponential fit of the D1 data, lies between the values in the energy range of the Ra-226 daughters.

In annex 8.2 we provide a frequency plot of both height and speed (Figure 78 and Figure 79 respectively). The height AMSL is confirmed to be approximately 42 m which corresponds to 25 m AGL. Although the speed shows an average of approximately 2.7 m/s, the majority of the time the drone has flown around 3 m/s instead of the targeted 2.5 m/s. This is probably due to human error.

2.1.5 Discussion

The point source measurements had two functions. First, to check the flight parameters at which we should perform the flight above the D1 site. We varied both the speed and AGL height to find the optimal values to ensure the flight above the D1 site would yield useful results. The variation-in-speed-experiments were especially useful since the AD6150 with the b-probe uses an 8 second time constant. The time constant causes a streaking effect in the dose rate map visible in Figure 31 at higher speeds. The streaking effect is especially visible at 5 m/s and at 2 m height. The contours become elongated resembling streaks of paint originating from the source. The altitude variation with the point source gave us less insight in parameters for the D1 site as the source-detector geometry is completely different. The heterogeneous ground contamination of the D1 site is significantly more complex, additionally, the increased height to stay clear of the treetops makes the D1 site additionally challenging to process. The topography is also a difficult parameter as determining it with the dense vegetation is troublesome.

Second, to attempt retrieving activity values from the flightlines closest to the Cs-137 point source. Note that this is only possible when the identity of the source is known, since it requires the gamma ray energies. As was mentioned earlier, the Cs-137 point source has an ambient dose equivalent rate of 5250 nSv/h at 1 m, resulting in an activity of 0.933 (0.047) MBq. The values in Table 5 should lie close to this activity. For the measurements at 1 m/s, the fitted activity is within 20 % of the source activity, for all heights. It is also clear that with increasing speed the accuracy of the activity estimate is diminishing and so is the R^2-value of the curve fit. The reduced accuracy and R^2-values are partly due to the lower amount of measurement points at higher speeds together with the influence of the time constant of the Automess 6150AD-b.

However, for the measurements at 10 m AGL height it is important to check the deviations on both x- and y-shift and the R^2-value. For the measurement at 1 m/s and at 10 m AGL height, the x- and y-shift, Table 12 and Table 13, show uncertainties of 6.4 m and 1.5 m respectively. While the R^2-value is 0.80, which is significantly lower than the values of the measurements at 2 m and 5 m AGL height. Therefore, the results of the measurements at 10 m should be interpreted with caution or even rejected as they do not provide a correct curve fit of the measured data. The reason for the strange and complex data at 10 m height is due to the limited source strength, making it difficult to distinguish background and point source from each other. Additionally, the time constant of the Automess 6150AD-b plays an important role. Due to the limited increase in dose rate, the Automess stays in its averaging algorithm. This causes the more block-like

structure at the 10 m height data visible in Figure 75, Figure 76 and Figure 77 in Annex 8.1. This also explains why the x- and y-shift have a higher uncertainty as there is no clear maximum to use as reference point.

The streaking effect could be reduced or even solved by adapting the flight parameters in flight and make them respond to the changes in dose rate. However, this would mean that the drone would need to be self-correcting and fly automatically. This is certainly possible but is not investigated in this thesis. An alternative for resolving the streaking effect is performing two or more measurements with different flight parameters, i.e. other heights, speeds or spacing. By creating an overview first, we can get an initial estimate of the hotspots or source locations. Hereafter, a specific measurement can be performed around the estimated area with slower and lower flight parameters to diminish the streaking effect.

The main difference between our study with a point source and that of Gabrlik and Lazna [92] is that they changed their flight height and source strength for their point source measurements. We decided to adapt the speed of the drone and AGL height to see the influence of both parameters. The advantages of the Gabrlik and Lazna approach is that they have a better understanding of the discrimination between the different sources. Additionally, they demonstrate the influence of the height (AGL) on their spatial resolution. However, they do not consider the influence of flight speed. Another possible difference is the topography of the area investigated. In Gabrlik and Lazna [92], the area has more height differences, making interpretation of the results more challenging.

The measurements with the Cs-137 point source helped in defining the flight parameters for a more complex and elaborate measurement campaign. The D1 site at Umicore is a waste deposit for radium containing waste. Historical measurements of this site, done by Vanmarcke and Cottens et al. [95], [96], can be compared with the measurements done by UAV. The historical ground measurements, visible in Figure 26a and Figure 27, have poor spatial resolution due to the grid spacing of 25 m. The reason for the large grid size is the dense vegetation on the site. Furthermore there are several localized maxima. The combination of these characteristics makes it difficult to retrieve a reliable dose rate map. To reduce the effect of the localized maxima, a median filter was used of which the results can be seen in Figure 26b. A downside of this filter is that the results of any comparison can only be compared qualitatively, making it necessary to compare both maps relative to the measured or simulated maximum. Figure 33a and Figure 33b are in relatively good agreement, certainly compared to the other tested filters visible in Figure 33c and Figure 33d. The most significant discrepancy between Figure 33a and Figure 33b is visible at the perimeter. A possible explanation for this is that the vegetation did not contribute significantly to the shielding or build-up of gamma rays. However, since this comparison uses a median filter and the historical measurement has poor resolution, the results do not completely validate the simple dose rate model.

Figure 30 and Figure 34 contain the height profile of respectively the point source measurement and the D1 site measurement. When we compare both, two things are noticeable. First, the variation in hoovering location of the drone has less or even no impact for the measurement above the D1 site, while it has a significant effect on the dose rate coming from the point source. It is important to note that the variation in height of the drone was similar in both scenarios. Second, the impact of the height is greater for the point source measurements compared to the D1 measurement. Both differences are due to the different source geometries.

Figure 35 shows the exponential least squares fit over the data from the D1 site, averaged for the five heights that were measured. The error bars are present for both x- and y-axis but for most points they are too small to distinguish, confirming the stability in height and in dose rate over the D1 site. Additionally we can confirm that the mass attenuation coefficient coming from the curve fit lies between the expected values for the energy range for the gammas of Ra-226 daughters, as is visible in Table 4. However, the value of the fitted curve visible in Figure 35, 0.013 m^{-1}, seems to be higher as is expected for all radium-226 daughters.

The reason for this discrepancy can be attributed to two reasons. Firstly, the attenuation of the soil and vegetation are not incorporated in this comparison. These additional sources of attenuation would increase the mass attenuation coefficient. Secondly, at higher altitudes the area of investigation measured by the detector increases. If this area of investigation is larger than the contaminated area, we will be including areas that have no or less contamination into the area of investigation. This will cause a decrease in measured dose rate compared to the dose rate from an infinite ground contamination measured at the same height. The increased area can be verified by adapting equation 9 in chapter 3.1.2.8 and Annex 8.5. The radius of the area of investigation in function of the height can be found in Figure 35. The radius is defined as a percentage of the flux coming from an infinite ground contamination. In Figure 36 the ranges for the lowest and highest energies for the radium-226 daughters are shown together with three different percentages, 50, 90 and 95 % of the flux from an infinite ground source. The angular dependence was set to 1 for the Automess 6150AD-b which according to Figure 21 is justified for the energy range of radium-226 and its daughters.

We also compared the normalised ambient dose equivalent rate in function of the AGL height from the D1 site with the theoretical values of a radium-226 point source and a practically infinite radium-226 surface source. As can be seen in Figure 35, the D1 site follows the surface source rather well, but with increasing height above ground level the D1 site shifts slightly towards the point source. The shift towards a point source is also logical from a theoretical point of view, as the distance increases the solid angle from the detector imposed by the D1 site will decrease until it is indistinguishable from a point. However, the drone that was used in this measurement was limited to the maximum height AGL of 120 m, therefore, we are unable to confirm this with experimental values. We did not use the measurements from the Cs-137 point source as it is a different nuclide and the source was not strong enough to allow measurements at the altitudes used over the D1 site.

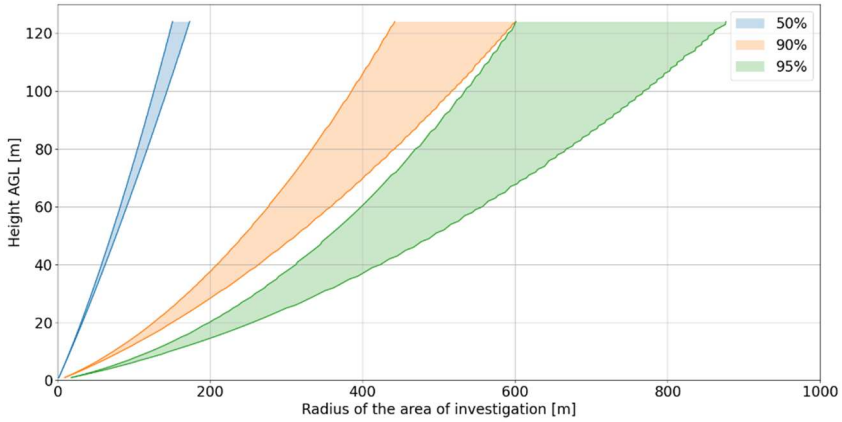

Figure 36: Radius of the area of investigation at varying heights above ground level. The percentages represent the amount of flux compared to an infinite ground source of radium-226. The range is between the lowest (242 keV) and the highest (1764.5 keV) energy for radium-226 and its daughters. The angular dependence of the 6150AD-b was assumed to be 1 for all energies.

Both the point source and D1 site measurements happened in relatively good conditions. There was no precipitation and there was little to no wind on the days of the measurements. This might not always be the case in an emergency situation. A test under worse conditions, rain and stronger winds, would certainly be advisable before this system is certified for use in emergency situations. However, these conditions will cause the UAV to have more trouble with remaining on the preassigned flightpath and flight height. With this information we can make an estimate of the increased variation in measured dose rates.

2.1.6 Conclusion

The point source results give a general idea about the limitations and possibilities of drone-based measurements. One of the main concerns is the flight speed. As can be seen in Figure 31, with an increase in speed the dose rate coming from the source is smeared out causing a streaking effect. However, this is strongly dependent on the time constant and the internal detector algorithms. The detector in this study has a relatively large time constant making it especially stable in stationary measurements or in a homogenous environment. For heterogeneous environments we advise to take a detector with a shorter time constant and to fly at a reduced speed. This would benefit the spatial resolution of the measured area. However, for the current experiment, we had no such detector available.

An improved GPS system with lower uncertainties would provide for a better positioning of the drone and a better estimate of the source to detector distance. This would improve the curve fitting of the point source measurements dramatically. However, the activity estimations using the Automess 6150AD-b did provide a good estimate with only a 25 % relative difference for all heights.

The current detector system is based on Bluetooth communication between the 6150AD-b and a smartphone. The smartphone has to accompany the detector system as the range of Bluetooth communication is limited to several meters. Additionally, work on providing remote resets, live feeds and data storage should be reviewed as the current system is error prone because it does not have any back-up or redundancy.

The flight altitude is another factor that influences the spatial resolution. Although this parameter is largely dependent on the surrounding, we advise to keep the flight altitude as low as safely possible. However, the final decision on height AGL lies with the drone pilot and should always be respected as he is responsible for the safety of the flight. The effect of the altitude can be seen in Figure 31.

The upside of using a dose rate detector is the simple and easy-to-use data output. The results are readily interpretable for first responders while spectrometry data would require more processing, a more in-depth knowledge about spectrometry and time to obtain and analyse a spectrum. The downside of a dose rate detector is that there is no way of identifying the nuclide at hand. However, a combination of both systems or a conversion of the spectra to dose rate would achieve both easily understandable results and the identification capabilities of a spectrometry detector. Other options are using the dose rate detector results as a preliminary measurement and using a more sophisticated detector at the measured hotspots. Other examples for which drone borne dose rate detectors can be used are remediation, source localization and routine monitoring.

The results in Figure 32 and the comparison in Figure 33a and Figure 33b show a good approximation for the simple dose rate model that is used on the median filtered historical data. Future studies might include deconvolution of the measurements [99], [100] or a more complete ground measurement campaign to avoid the use of a median filter. Studies involving gamma ray spectroscopy with the possibility for dose rate conversion might give more insight concerning the distributions of the Ra-226 concentration and the concentration of its daughters, while maintaining the possibility of simple dose rate data by converting the spectra. Studies from Grasty et al., Camp et al., Tsuda et al., Dombrowski et al. and Kanti et al. provided the necessary method for such a conversion to be possible [33-36], [90].

The results from chapter 2 are the first steps in this thesis on radiological measurements using drones. They provide proof of concept and give insight into the importance of flight height and flight speed. Additionally, dose rate readings are relatively simple to understand and can give fast indications about the safety of a region. However, the information the dosimetry measurements provide cannot be used for identification of the radionuclides, which is an important step for a more in depth dose estimation for the public. Some radionuclides (e.g. I-131) have exposure pathways that are significantly more harmful to the public, therefore, the identification is important so that the necessary precautions can be implemented.

2.2 Drone-Borne Dosimetry in a Radiological or Nuclear Scenario: RadDetecTIF

2.2.1 Introduction

The D1 site of Umicore, described in chapter 2.1.3.7, was used as a comparison exercise [51]. In this exercise the RadDetecTIF (Radiation Detection and Transmission In Flight) system [81] was used as a spectroscopic drone-detector system. The CsI scintillator detector, Sigma50, is a simple 2”x1”x1” detector that uses a SiPM as readout of the light pulses. Together with a Raspberry Pi it records and transmits the gathered data to a ground control pc providing a live feed of the readings. Since we wanted to compare the systems, the 6150AD-b and the RadDetecTIF, against each other we had to convert the gathered spectra into dose rates. The conversion was done with the stripping method. The final results are comparable with the data recorded with the 6150AD-b in chapter 2.1.4.2.

2.2.2 Method and Materials

2.2.2.1 RadDetecTIF

The RadDetecTIF is a stand-alone drone-detector system that uses Kromek Sigma50, a CsI scintillator detector with a silicon photomultiplier. The detector measures 2” by 1” by 1” and is placed with the rectangular side facing down. The detector is connected to a Raspberry Pi 2+ that controls the recording of spectra, pressure, time and GPS-coordinates. The Raspberry Pi also prepares the data to be sent through long range radio transmission providing a live stream at the ground control pc. The GPS coordinates are obtained from the MTK3339 GNSS receiver. For a more detailed breakdown of the RadDetecTIF we refer to the technical description [81].

2.2.2.2 Stripping

Stripping is a method to convert spectral data into a dose rate [33-36], [90]. The spectrum is divided into several regions that have a dose weight factor assigned to them. The number of counts and the weight factor are multiplied to obtain the dose contribution of that spectral region. The sum of the results of each region gives the total dose related to the spectrum. The weighing factor of each individual region is calculated by experimental data. Ideally the sources for these experiments should be monoenergetic. This is preferred because additional gamma peaks will make the weighing factor dependent on multiple energy regions, which adds uncertainty to their value. The number of energy regions should be as high as possible to achieve a smooth weighing factor curve. However, this requires several monoenergetic sources which are not always available.

The first step is performing the measurements of the selected monoenergetic sources. The energies of the selected sources should be spread so that lower energies are better represented, as their weighing factors have higher variations. This is also visible in Figure 38 when comparing the weighing factors for the

regions below 500 keV. For higher energies the weighing factors do not change significantly over multiple regions. The second step is calculating the dose rate that would be obtained at the detector's position due to the individual sources. The third step is calculating the dose rate weighing factors beginning with the lowest energy, the second energy and region can then be calculated by first subtracting the dose rate due to the lower region. This process repeats itself until all weight factors are calculated. Equations 3, 4 and 5 show the calculations needed for region 1, region 2, up to region n.

$$w_1 = \frac{H^*(10)_1}{E_1 r_{11}} \qquad (3)$$

$$w_2 = \frac{H^*(10)_2 - w_1 E_1 r_{21}}{E_2 r_{22}} \qquad (4)$$

$$w_n = \frac{H^*(10)_n - w_1 E_1 r_{n1} - w_2 E_2 r_{n2} - \dots}{E_n r_{nn}} \qquad (5)$$

E represents the energy in eV, r is the number of counts in the specified region, $H^*(10)$ is the dose rate coming from the specific region in J/kg and w is the weighing factor for the region expressed in $J/kg.eV$. The weighing factors for the RadDetecTIF system were calculated using the response from a Penelope detector model together with experimental spectra to validate the model. It was difficult to obtain the necessary monoenergetic gamma sources for the complete energy range we wanted to measure. Therefore, we opted for creating a Monte Carlo model in Penelope, validated using the available sources. The results of the validation can be seen in Figure *37*. The model was then used to simulate several monoenergetic sources which made it possible to calculate the weighing factors. The weighing factors are shown in Figure 38. The nuclides used for verifying the Penelope Monte Carlo model were Am-241, Co-60, Eu-152, Cs-137 and Na-22. The gamma peaks corresponding to the respective radionuclides can be found in annex 8.4.

2.2.3 Results and Discussion

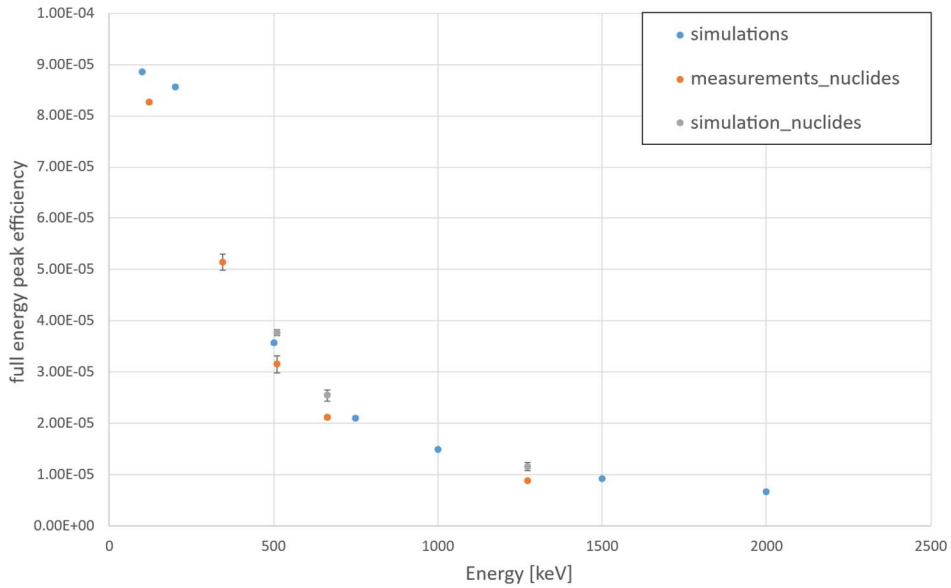

Figure 37: Validation between the experimental and simulated measurements of the Kromek Sigma50 CsI scintillator detector. The simulated measurements were done with Penelope (2018). All measurements had a source-detector distance of 100 cm and the source was placed normal to the rectangular detector face. The blue dots represent the full energy peak efficiency of Monte Carlo simulations with gamma ray energies that were chosen to be evenly spaced for performing stripping. The orange dots represent the measured full energy peak efficiencies for the gamma ray energies linked to the nuclides mentioned in chapter 2.2.2.2. The grey dots represent the full energy peak efficiency of Monte Carlo simulations with gamma ray energies linked to the nuclides mentioned in chapter 2.2.2.2.

Figure 37 shows the comparison between the experimental and simulated full energy peak efficiency taken directly from the Monte Carlo simulations. Although the model could be slightly improved at the lower energies, the uncertainties encountered in flight would make the differences neglectable. A target for further research is to perform all experimental measurements with mono-energetic sources making the Penelope Monte Carlo model redundant.

In Figure 38, the weighing factors for the Sigma 50 CsI detector are shown, based on the mono-energetic gamma rays simulated with the Monte Carlo model in Penelope. The values were calculated using Equations 3, 4 and 5. The lower energies have more simulated points as the weighing factors change more drastically in this region compared to the higher energies. Although experimental data would be preferred, this solution still returns acceptable results.

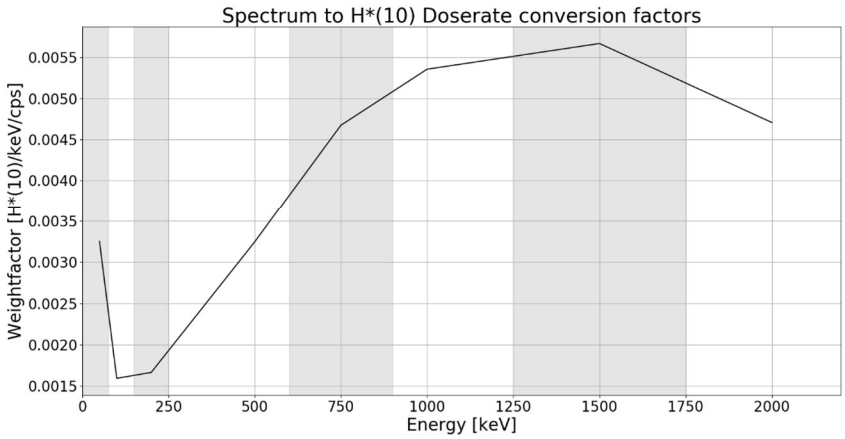

Figure 38: Spectrum to H(10) weighing factors for the Sigma50 scintillator detector in the RadDetecTIF drone-detector system.*

In a similar fashion as with the Automess 6150AD-b, we used the RadDetecTIF to measure the D1 site, which created Figure 39. Figure 39 can also be compared with Figure 32, both show similar features like the shape and location of the measured maxima. The maxima of Figure 39 and Figure 32 are 3762 nSv/h and 4640 nSv/h respectively, which gives a relative difference between the dose rate maxima of roughly 19 %. The differences in dose rate can be explained due to the size of the detector and the conversion of the Sigma 50 spectra into ambient dose equivalent rates. Although the flight plan was exactly the same for both flights, it might also be possible that there are some deviations of the flightpath due to wind, temperature, pressure and GPS uncertainty.

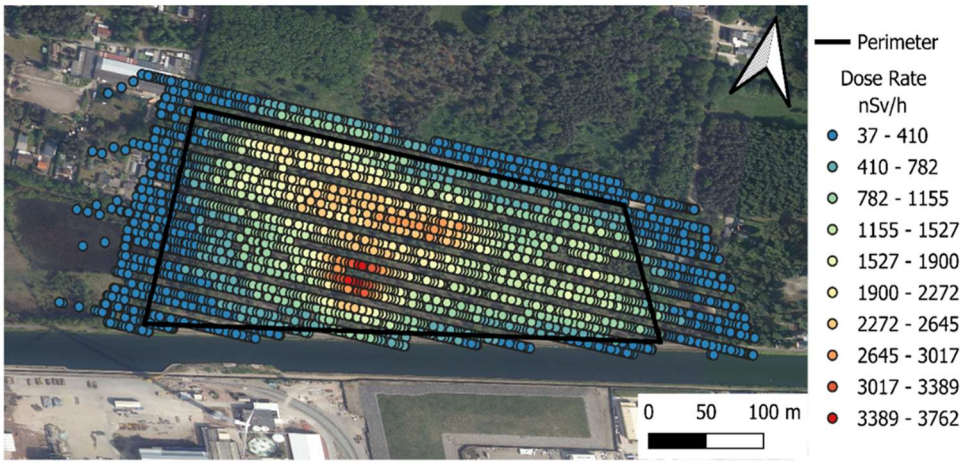

Figure 39: H(10) dose rate map of the D1 site. The data was obtained by converting the spectra from the RadDetecTIF to ambient dose equivalent rate (H*(10)).*

2.2.4 Conclusion

The RadDetecTIF spectral measurements over the D1 Site were compared to the measurements done with the 6150AD-b (Figure 32). Since the RadDetecTIF does not output ambient dose equivalent rate, a stripping method had to be implemented. Stripping allows the spectra to be converted into ambient equivalent rate resulting in Figure 39. The results of the 6150AD-b and the RadDetecTIF measurements seem to correspond relatively well to each other. The shape and location of the maxima show a good agreement. The absolute values of both measurements do not agree with each other, the maxima for example have a relative difference of 19%. The difference in absolute values could be caused by the different detector volumes, the different detector systems or the use of the stripping method. There are two possible adaptations that could significantly improve the stripping method. We could either adapt the Monte Carlo model to correspond better to the detector output or we could obtain the necessary monoenergetic sources and use the experimental results as the basis for the stripping method. This would be an interesting topic for further research and additional testing, especially as the angular dependence of the sigma50 scintillator is not uniform.

2.3 Conclusions on Objective 1

The two subchapters above show that the necessary objectives were achieved. Firstly, sub-objective 1a, comparing different detector systems regarding drone-borne dosimetry, has given us insight into the disadvantages and advantages of both investigated systems, Table 6 gives an overview of the comparison.

The 6150AD-b, a reference dose rate detector measuring ambient dose equivalent rate, showed great potential as a system for drone-borne dosimetry. It can be used as is with minimal modifications to mount it underneath a UAV. A smartphone with an application and Bluetooth and the Bluetooth-transmitter are the only necessary additional equipment needed for recording data. By using the wireless network of the smartphone it is even possible to achieve live monitoring, although this was not tested since it is out of the scope of this thesis. The 6150AD-b has nearly no angular dependence over the targeted energy range, meaning that the uncertainties regarding directionality are limited. However, the 6150AD-b together with the Bluetooth module weigh close to 2.2 kilograms, ignoring the weight of the mounting brackets and smartphone. This might be problematic for some UAVs as it exceeds the maximum payload weight or shortens the flight time significantly. Identification is not possible with this system as its resolution does not allow it.

The RadDetecTIF, a standalone detector system specifically designed for UAV measurements, contains a Sigma 50, a 1" by 1" by 2" NaI scintillation detector from Kromek. The data from the detector is read out by a Raspberry Pi and sent to a laptop on the ground through long range radio transmission. This allows for a live feed of the recorded data and makes identification of hotspots faster. As the NaI detector produces spectral data, we can identify the gamma ray energies and the radionuclide they originate from. This is especially useful for scenarios with limited knowledge on the source. The weight of the system is limited to less than 1 kg making it more flexible to be used with different UAVs. The dose rate can be achieved by using a stripping method on the recorded spectra. However, correctly creating the weighting factors for the stripping method requires monoenergetic gamma sources which are not always available. An additional difficulty is the angular dependence for the Sigma 50 due to its rectangular shape. Spectral data are significantly more complex to understand and read as their dose rate counterparts. Therefore, dose rate values are preferred in case of radiological or nuclear emergency.

Table 6: Comparing the advantages and disadvantages between the 6150AD-b dose rate detector and the RadDetecTIF spectroscopy detector.

Dose Rate Detector (6150AD-b)	**Spectroscopy Detector (RadDetecTIF)**
Advantages	
Simple readout	Identification is possible
Easy setup	Live feed
Readily understandable	Distinguish multiple sources with different gamma energies
No angular dependence	Lightweight (less than 1 kg)
Available for most intervention teams as it is a standard dose rate detector	Dose rates can still be extracted through stripping
	Remote reset in case of issues
Disadvantage	
Heavy (more than 2.2 kg)	Complex system
No identification possible	Readout requires spectroscopy knowledge
No live feed (but possible)	Strong angular dependence might complicate understanding the data
No remote reset	Stripping requires extensive calibrations
Time constant causes streaking effects	
Mounting as payload is cumbersome	
GPS coordinates have to be linked after the flight with the drone data	

The conclusion on sub-objective 1b, recommendations on dose rates measured by UAVs with the aim of assisting first responders, is less straightforward as it depends heavily on the source geometry. For point sources we have proven that the speed and altitude are important factors for creating dose rate maps. As slow as possible and as low as possible rendered the best results regarding spread of the measured dose rates and avoiding the streaking artifacts. Although the streaking was mainly due to the time constant of the 6150AD-b. For ground or surface contaminations the speed is less influential. However the altitude is an important factor and is also linked to the size of the area of investigation. The spatial resolution of the detector is also significantly worse at higher altitudes, as is shown in Figure 36. For future investigations deconvolution would be an interesting topic to investigate, as it can greatly improve the spatial resolution. This concludes objective 1 and research question 1.

3 Drone-Detector Solutions for Radiological Surveillance

Drone-detector systems can be deployed in emergency scenarios, for recovering lost sources or even for security of large events. In this chapter the design, development and testing of a custom drone-detector system will be explained. The initial design was obtained from computer simulations using the Monte Carlo code Penelope. From these simulations a detector material and geometry were chosen to optimize the efficiency. The development was done in cooperation with SABCA to integrate the detector system within the fixed-wing UAV.

The testing was done to cover various environments and sources. Firstly, laboratory measurements were done using point sources. These measurements were used to calibrate the efficiency of the detector system. Secondly, stationary field tests were done using the Ar-41 plume originating from the BR1 reactor at the SCK CEN. This was done to verify the detector could measure the plume over larger distances, 60 m in this case. The third measurement was done with the Penguin C fixed-wing UAV over the fields surrounding Droneport Sint-Truiden. The goal was to measure the K-40 concentration on the ground. This was verified by taking samples from fields in the neighbourhood and measuring the concentrations. The last measurement was done over the SCK CEN using the Penguin C fixed-wing UAV. The sources for this measurement were a radium waste site, Belgoprocess and the Ar-41 plume form the BR1 reactor at the SCK CEN.

This chapter is also split into two separate chapters. The first chapter, 3.1, is taken from the publication Radiological Surveillance Using a Fixed-wing UAV Platform [84]. Chapter 3.2 handles the additional measurements and the more complex measurement campaign over the SCK CEN using the same detector system as was used in chapter 3.1.

3.1 Radiological Surveillance Using a Fixed-wing UAV Platform

For identification and a more in-depth analysis of the results we require spectroscopy measurements with a detector system that can distinguish the different gamma energies it would encounter. Additionally, the detector system needs sufficient counts in the spectrum to account for statistical variation. In the next chapter we will show the process of selecting the optimal detector material and shape such that both prerequisites, resolution and efficiency, are considered. The current chapter is based on the paper 'Radiological Surveillance Using a Fixed-wing UAV Platform' and is published in Remote sensing [84].

A drone–detector system was designed, developed, and tested for radiological monitoring. The system was tailored to perform measurements during the threat, release, and post-release phases of a nuclear or radiological event. This allows

the surveillance of large areas, with an autonomy of up to 12 h, in a large range of altitudes above ground level. The detector system was optimized for gamma spectroscopy, taking into account the available payload for maximum endurance and maximum detection efficiency using 'Penelope (2018)' Monte Carlo simulations. A generic methodology was used to derive quantitative information on radioactivity levels from the raw measured gamma ray spectra at different altitudes. Based on the methodology, it was demonstrated that the drone–detector system can measure the concentration of potassium-40 (K-40) that is naturally present in the soil. These measurements complied within 30% of the soil sampling results taking into account the uncertainties. The functioning of the system was tested during test flights, which demonstrated that radionuclide identification and quantification of radioactivity concentrations are possible.

3.1.1 Introduction

Unmanned aerial vehicles (UAVs) have recently seen increased use in the field of surveillance and monitoring. Depending on the payload, they can be used for environmental monitoring, fire control, search and rescue, visual inspections, or other applications. Most systems require a high-resolution or thermal camera. Although it might be useful to have visual information, such systems are in principle not required for environmental monitoring of radioactivity. It is, after all, not possible to detect, identify and characterize radioactive material with this equipment [2], [4], [12], [82].

Most radioactive materials emit gamma and/or X-rays as they decay. The fact that this type of radiation can be detected over large distances in the environment, due to the limited attenuation in air, makes gamma spectroscopy the most common detection technique of radioactivity using UAVs [92]. While the environmental monitoring of gamma and X-ray radiation with UAVs creates new opportunities for radiological protection in routine and emergency scenarios, as well as for the monitoring of radioactivity in the environment, it also poses new challenges. A first advantage of the use of UAVs is the possible autonomy, i.e., not requiring an operator to perform the measurements. With most radiological surveys, an operator has to systematically map the area of investigation with a hand-held detector. Operators could be exposed to increased levels of ionizing radiation, which is a safety concern. Additionally, operators could possibly influence measurements by shielding the detector with their bodies. By using a UAV, both issues are resolved. No dose is absorbed by operators and the UAV does not shield the detector from the ground [48], [49]. A second advantage is accessibility. People are restricted in their movement because of terrain or vegetation. Although UAVs must also be operated cautiously near high structures and trees, UAVs are less restricted in their movement and can easily reach difficult-to-access places. The UAV in question can also be equipped with an optical avoidance system to increase the safety, as it automatically detects obstacles and avoids them. A third advantage is the reproducibility of UAV surveys. The flight plans can be repeated to see the evolution of a contaminated site over time or to follow up remedial actions[45]. A fourth advantage is the speed of UAVs, making them able to map large areas in a relatively short timeframe. This is especially

important in emergency scenarios where decisions on protective measures need to be made quickly. An alternative for UAVs are helicopters. However, helicopters require both a pilot and an operator, which puts two people at risk of exposure to ionizing radiation.

A downside of using UAVs as an instrument for surveys is the minimal flight altitude of the UAV, which causes a decreased efficiency of the measurement. Depending on the geometry of the radioactive source, the reduction in efficiency can be caused by a combination of the inverse-square law and the attenuation in air. For point sources, the inverse-square law will cause the most significant part of the reduction, while for a surface source the attenuation will be the main parameter that influences the efficiency. Besides the reduction in efficiency, an increase in height also increases the field of view of the detector and therefore decreases the spatial resolution. The decrease in spatial resolution due to the field of view can be improved by using a collimator. However, this makes detection more complex and adds weight to the payload. A second problem specific to battery-powered drones is their power consumption. On the one hand, if a UAV flies too slowly over an area of investigation, it will not be able to carry out the full site survey due to the limited battery power. On the other hand, by flying too fast, the measurements will be integrated over a larger area, resulting in a decrease in spatial resolution. A final issue is the presence of high structures that have to be avoided. This requires pre-flight visits to acquire the position of the obstacle, and pilots might have to intervene during an automated flight when there is a risk of collision.

In recent years, new experiences have been reported regarding radiological monitoring and surveillance using drones. Several studies were performed with both fixed-wing and multicopter drones incorporating a detector system as payload [9], [11], [14-18], [85]. Depending on the task, payloads were optimized in regard to their efficiency, detection method, or mapping. In this paper, we will discuss the development and first results of a new fully optimized drone–detector system using a fixed-wing UAV. For the intended applications, namely radiological monitoring in accident scenarios with gamma-ray-emitting nuclides, we do not require data that are highly spatially resolved. Therefore, the minimal height does not pose a problem. However, during accidents, it is beneficial to use a system that can be airborne for multiple hours and that has the ability to identify and quantify the release or contamination based on gamma spectroscopy. The optimization and development of the new drone–detector system described in this paper is focused on these parameters and requirements.

In principle, if the geometry is known, the gamma ray flux can be calculated. Combined with the characterization of the detector this allows us to quantify the source. For point sources, the gamma ray flux at the detector location can be easily determined. For surface contaminations, however, the procedure is slightly more involved. To determine the gamma ray flux in this case, the historic work of Beck et al. [65] on in-situ gamma ray spectroscopy or the IAEA technical document 1092 [67] can be extended to UAV measurements, the work of Beck et al. was specifically focussed on In-Situ gamma ray spectroscopy. The IAEA

technical document 1092 focusses on 'the generic procedures for monitoring in a nuclear or radiological emergency' and uses the work of Beck et al. as a basis for In-Situ gamma ray spectroscopy but also considers more complex scenarios. The theoretical framework allows for calculating the flux at the detector that originates from either contamination or naturally occurring radioactivity in the soil. This requires extensive knowledge of the detector response as well as a good approximation of the distribution of radioactivity in the soil as a function of the depth.

A spectroscopic system allows us to detect increased radiation levels either as an increase in the total count rate or as the presence of certain lines in the gamma ray energy spectrum. The latter allows for the identification of radionuclides. However, the geometry of a source has a significant influence on the measurements. This can make the quantification of a radioactive source a challenging task. The relation between the detector signal (e.g., the net gamma peak area count rates in gamma spectroscopy) as measured during the drone flight and the radiation source (i.e., the calibration factor C_f, which is specific for every gamma ray energy), can in general be written as:

$$C_f = \frac{N_f}{I} = \frac{N_0}{\varphi}\frac{N_f}{N_0}\frac{\varphi}{I} \qquad (6)$$

where N_f is the net peak area counting rate obtained from the measured spectrum in $counts/s$, I is the surface or soil concentrations expressed in Bq/m^2 or Bq/m^3 respectively, N_0 is the net peak area counting rate from a point source measurement with the point source positioned normal to the detector face in $counts/s$, and φ the flux of incoming gamma rays expressed in $gammas/cm^2 s$. Beck et al. and IAEA split the detector response in three factors as shown in Equation 6. The first factor, N_0/φ, is the estimate of the counts per second under the net peak counting rate due to a unit flux incident normal to the detector face. The second factor, N_f/N_0, is the angular correction factor for the detector and depends on the gamma energy incident on the detector. The angular response is integrated over the spatial distribution in the ground. The last factor, φ/I, is the ratio of the incident flux over the concentration.

In this paper, we describe the development and testing of an optimized drone–detector combination for monitoring during the threat, release, and post-release phases of a nuclear or radiological event. Further, it is demonstrated that the system at different flying altitudes is capable of quantifying a radioactive source. This is done for naturally present potassium-40 in the soil by comparing the UAV results with soil sampling results. This experiment demonstrates that the system can also be used for other applications outside nuclear and radiological emergency response.

In Section 3.1.2, the fixed-wing UAV parameters are described as well as the design and hardware structure of the detector system. Additionally, Equation 6 will be explained in more depth, especially regarding the quantification of radioactive concentration in soil.

In Section 3.1.3, we will present the data obtained during two separate flights. The flights were performed above agricultural fields that contain only natural radioactivity typical for the region and soil type. The gathered data were then used to calculate the potassium-40 (K-40) concentration in the soil. K-40 is a natural radioactive material that emits a gamma ray with an energy of 1460.8 keV that can be measured by a gamma spectroscopy device. To test the detector system, we compared the measured concentrations with concentrations obtained by taking soil samples at the surrounding fields.

3.1.2 Material and Methods

3.1.2.1 Penguin C

The Penguin C [101] is a fixed-wing drone with a gas-powered engine with electronic fuel injection. It can fly with a maximum payload of 2 kg and has a maximum take-off weight (MTOW) of 23 kg. With a flight endurance of up to 12 h, it can easily manage to stay airborne during accidental radiological releases to give live updates on the situation. The wingspan of the Penguin C is 3.3 m, and it has a length of 2.3 m. A pressurized catapult is used to launch the drone with an acceleration of 6 G. To cope with these forces, it is necessary to have a robust detector system. To land, the drone uses a parachute in combination with an airbag. The landing procedure is started a couple of minutes in advance, taking into account wind direction, location, and heading to make sure the drone lands in a clear and safe zone without trees or other obstacles. The airbag is used to reduce the impact and minimize the risk of damaging the drone and payload. The drone and ground control station communicate with each other over long-range data transmission using a tracking antenna. The antenna has a range of 100 km and can send data at a speed of 12 Mbps. The altitude range of the fixed-wing is between 120 m (400 ft) and 5000 m (FL160). FL160 means flight level 16000 feet or roughly 5000 m. For radiological mapping using drones, the lowest altitude is determined by the automatic deployment altitude of the parachute, which SABCA set to a height of around 150 m for safety reasons. This range is ideal to survey the area of a nuclear site and its surroundings. In the threat and release phases of a radiological accident, the UAV can fly at high altitudes to avoid contamination by potentially released radioactive material. In the post-release phase, the UAV can fly at lower altitudes, typically just above common structures in the landscape, to map the area in detail. The minimum flight height for the Penguin C is not the same for every other UAV. It is dependent on the type, region and scenario and can be either higher or lower. The Penguin C has a nominal cruise speed of 19 to 22 m/s and a maximum speed of 32 m/s. Figure 40 shows the fixed-wing drone mounted on the pressurized catapult.

Figure 40: Penguin C mounted on the pneumatic catapult.

3.1.2.2 Flight plan

The flight plan can be created and adapted on the [102]. The Piccolo software can adapt the flightpath during the flight. For accident scenarios, adapting the height is useful to avoid contamination by the released radiological plume or to improve the spatial resolution and efficiency for monitoring contaminated sites. For the performed flights, we used two flightpaths. The first path was a circle with a 300-m radius at multiple heights, while the second path was a scanning grid. The path can be closely monitored since the drone transmits all parameters each 0.1 s. Afterwards, these parameters can be used for post-processing. For example, this involves incorporating the tilt angle into the angular dependence and correcting the altitude due to topography changes.

3.1.2.3 Requirements and Limits

The design of the payload has certain limits and requirements. Firstly, the weight limit of the payload is 2 kg. In case of additional weight, the good flight performance of the Penguin C is significantly compromised, and adaptations are required for stabilizing the drone. Secondly, to achieve a decent spatial resolution, the detector has to take spectra every second. However, to obtain better counting statistics in the spectra, it is possible to combine multiple spectra, which reduces the spatial resolution but improves the counting statistics of the spectra. Thirdly, data can be transmitted with a maximum bandwidth of 12 Mbps. The bandwidth is meant to be used for camera footage and therefore it is certainly possible to transmit text files that contain time, height, GPS coordinates, and spectrum data, which add up to approximately 24 kbps. Fourthly, the efficiency of the payload has to be optimized, as the height will cause the efficiency to drop due to the inverse-square law for point sources and due to attenuation for surface contaminations. Fifthly, because the drone–detector system is subject to strong accelerations and vibrations, a secure and safe connection has to be established between the payload and the drone. Therefore, we use a micro-D connector.

These connectors are mainly used in the aerospace industry and comply with our needs regarding vibration resistance because of their shape and fastening screws between both ends of the connectors.

3.1.2.4 Detector Design

One of the main limitations of using a fixed-wing drone is the minimum height required to fly safely. For the Penguin C, this is approximately 150 m. Because of the inverse-square law and attenuation effects, the efficiency of a detector system is reduced significantly compared to a measurement at or near ground level. This can be compensated by increasing the detector volume. This, however, cannot be done irrespective of the payload of the UAV system. Consequently, to maximize the efficiency of the detector system it is necessary that the detector geometry and material be optimized. This was done by performing Monte Carlo simulations using the Monte Carlo code PENELOPE (2018), more specifically the main program penmain [75-78]. Four types of detector material were selected (CsI, NaI, CeBr, and LaBr) and tested by simulating a cobalt-60 (Co-60) point source. Three other materials, CZT, BGO, and HPGe, were also taken into consideration initially but respectively discarded because of production volume, spectroscopic resolution, and cooling requirements. Each simulated detector was enclosed in an aluminium housing with a thickness of 1 mm that was separated from the detector crystal by another 1 mm of air. An example of the simulated detector geometry can be seen in Figure 41, although please note that it is not to scale. We constrained the weight of the crystal to 1 kg and varied the thickness and radius of the crystal to keep the same volume and weight of detector crystal. This allowed us to add 1 kg of additional hardware materials, such as detector housing, electronics, cables, etc. The detection efficiency is strongly dependent on the gamma ray energy emitted by the radionuclide. Co-60 was used because of its main gamma energies at 1173 keV and 1332 keV. These energies are on the high end when compared to gamma energies encountered in the decay of the most common artificial radionuclides. By optimizing the detector for higher energies, we make sure that the lower gamma ray energies will also be detected. Besides the gamma ray energy, Co-60 is also easily available as a point source for calibrations.

3.1.2.5 Monte Carlo Simulations

The simulations were performed on the supercomputer of VSC (Vlaams Supercomputer Centrum) to perform parallelization to increase the number of counts in the spectrum and reach a statistical uncertainty of less than 0.2%. Parallelization was performed by running multiple instances of the simulations on different cores of the supercomputer. For each instance, a different seed was selected for the pseudo-random number generator. Afterwards, the results of the separate simulations were combined to obtain one simulation.

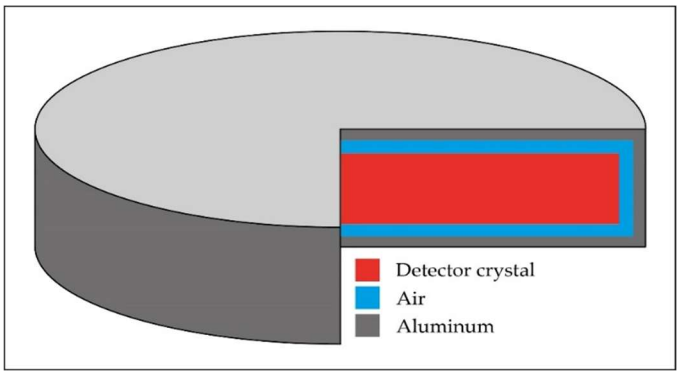

Figure 41: Schematic of the simulated detector geometry (not to scale).

In Table 7 all simulations are listed together with the geometries of the crystals and their full energy peak efficiencies calculated from the combined Co-60 peaks corrected for the gamma ray intensity. The simulations with the square slab geometry were slightly worse in regard to solid angle than their cylindrical counterparts. A last reason to prefer the cylindrical geometry is the symmetry: the cylindrical geometry makes it easier to determine the angular dependence and implement corrections for this effect. Therefore, we chose to investigate the cylindrical geometry further.

In the simulations, we worked with both an energy deposition detector and an energy impact detector defined to the detector crystal. Energy deposition detectors keep track of the distribution of the amount of energy that is absorbed by the entire crystal per decay while the energy impact detectors keep track of the distribution of the gamma rays that reach the detector crystal. Using these two types of detectors allowed us to calculate the solid angle, the full energy peak efficiency, and the detector efficiency of the detector crystal.

The full energy peak efficiency, detector efficiency and solid angle calculated for different detector thicknesses are given respectively in Figure 48, Figure 49 and Figure 50. The solid angle is defined as the ratio of the number of gamma rays (with energy E) that reach the detector and the number of gamma rays (with energy E) emitted by the simulated source. The absolute full energy peak efficiency is defined as the ratio of counts in the simulated full energy peak and the number of gamma rays (with energy E) emitted by the simulated source. The detector efficiency is defined as the ratio of counts in the simulated full energy peak and the number of gamma rays (with energy E) that reach the detector. Figure 3 demonstrates that CsI with a thickness of 3.0 cm gives the highest full energy peak efficiency. The source–detector distance is 5 m in the simulations because the simulation efficiency at a distance of 200 m is too low. For the extrapolation to larger distances, the detector efficiency, shown in Figure 4, can be used as a decision parameter for the selection of a suitable detector material and size or the inverse-square law can be used to apply a correction factor to account for the reduction in efficiency. In both cases, CsI comes out as an optimal

option. We chose CsI because of these simulations and because it is less expensive than CeBr and LaBr. Furthermore, aerial measurements do not require high spectral resolution, making CsI a valid candidate [58].

Table 7: List of geometric parameters for all Penelope Monte Carlo simulations and the full energy peak efficiency with their respective percentile error. The simulations were done with the detector crystal and a 1-mm-thick aluminium housing. The Co-60 point source was placed 5 m below the detector and the two main gamma peaks were combined for the full energy peak efficiency.

Detector Geometry	**Material**	**Thickness (cm)**	**Side/Radius (cm)**	**FEP Efficiency**	**Error %**
Square Slab	CeBr	1.00	14.00	6.24×10^{-6}	0.10
		2.00	9.90	2.99×10^{-6}	0.15
	LaBr	1.00	14.06	6.05×10^{-6}	0.10
		2.00	9.94	2.90×10^{-6}	0.14
	NaI	1.00	16.51	5.98×10^{-6}	0.10
		2.00	11.67	7.54×10^{-6}	0.09
	CsI	1.00	14.89	7.26×10^{-6}	0.09
		2.00	10.53	8.56×10^{-6}	0.08
Cylindrical Disk	CeBr	0.50	11.17	4.50×10^{-6}	0.11
		1.00	7.90	6.29×10^{-6}	0.10
		2.00	5.58	7.68×10^{-6}	0.09
		3.00	4.56	8.07×10^{-6}	0.15
		4.00	3.95	7.68×10^{-6}	0.09
	LaBr	0.50	11.21	4.37×10^{-6}	0.11
		1.00	7.93	6.15×10^{-6}	0.10
		2.00	5.61	7.47×10^{-6}	0.09
		3.00	4.58	7.94×10^{-6}	0.15
		4.00	3.97	7.58×10^{-6}	0.09
	NaI	1.00	9.31	6.00×10^{-6}	0.10
		2.00	6.59	7.59×10^{-6}	0.09
		3.00	5.38	8.03×10^{-6}	0.09
		4.00	4.66	7.96×10^{-6}	0.08
	CsI	1.00	8.40	7.23×10^{-6}	0.09
		2.00	5.94	8.69×10^{-6}	0.08
		3.00	4.85	8.91×10^{-6}	0.08
		3.50	4.49	8.90×10^{-6}	0.13
		4.00	4.20	8.68×10^{-6}	0.12
	Final design CsI	3.00	5.50	1.17×10^{-6}	0.10
		3.50	5.00	1.12×10^{-6}	0.11

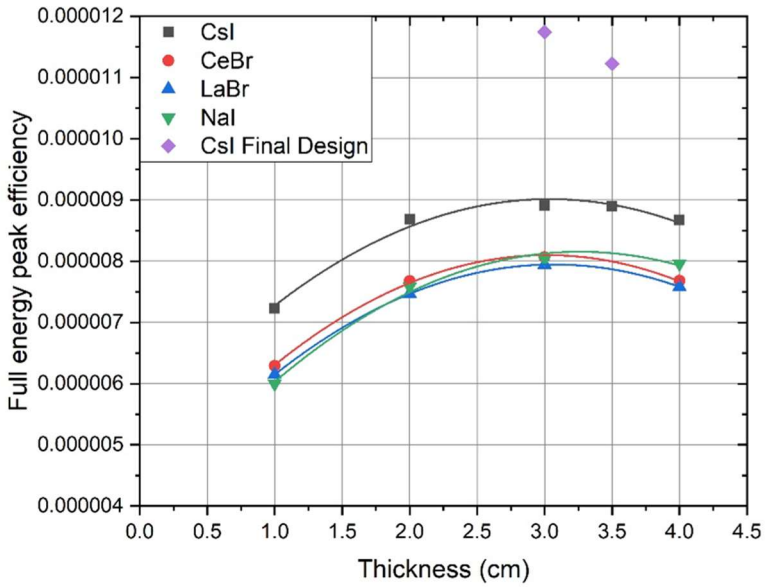

Figure 42: Results of Monte Carlo simulations using Penelope (2018). Different detector materials and geometries with a mass of 1 kg (all except Final Design) compared to the detector efficiency of the combination of the two main gamma peaks of Co-60 (1173 keV and 1332 keV).

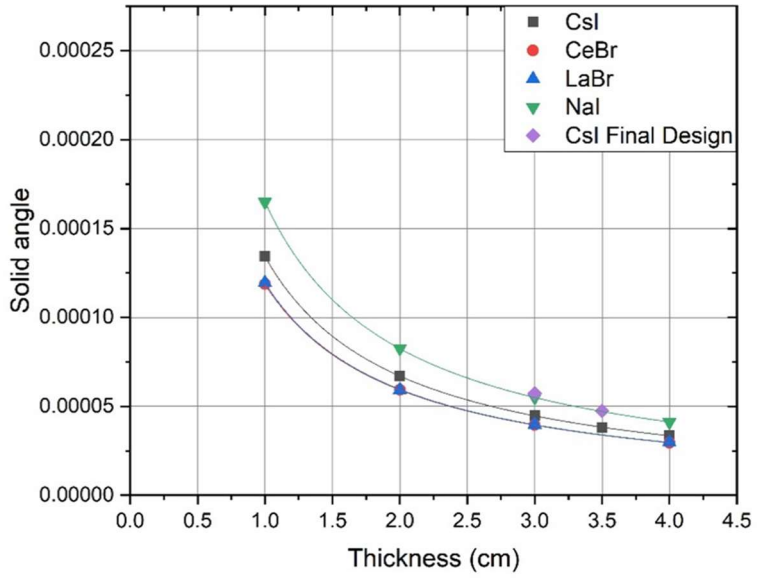

Figure 43: Results of Monte Carlo simulations using Penelope (2018). Different detector materials and geometries with a mass of 1 kg (all except Final Design) compared to the solid angle of an isotropic Co-60 point source.

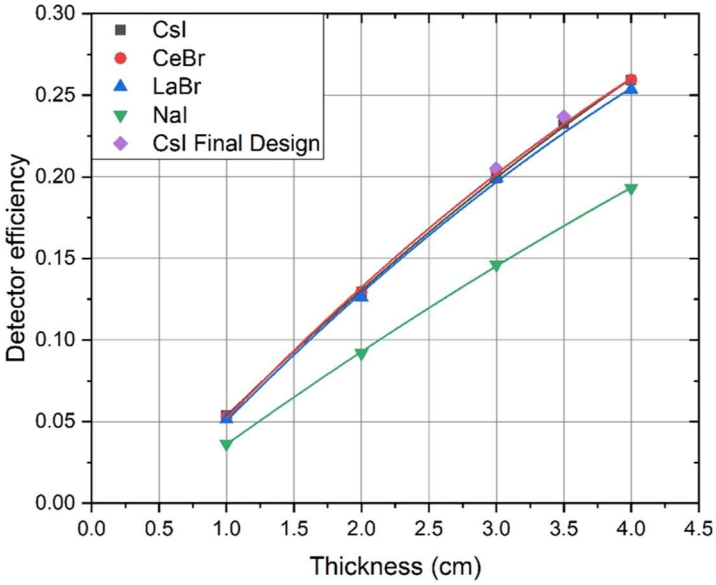

Figure 44: Results of Monte Carlo simulations using Penelope (2018). Different detector materials and geometries with a mass of 1 kg (all except Final Design) compared to the full energy peak efficiency of the combination of the two main gamma peaks of Co-60 (1173 keV and 1332 keV).

3.1.2.6 Final Detector Design

In the final design, it was noticed that the weight of the complete detector system was still below the predefined limit of 2 kg. Therefore, we adapted the detector shape slightly by increasing the radius of the detector to 5.5 cm. We chose to adapt the radius instead of the thickness by running a final set of Monte Carlo simulations investigating both options. The results of the simulations are shown in Figure 42, Figure 43 and Figure 44. The final detector shape was set to a CsI disk with 3.0 cm thickness and a radius of 5.5 cm. The volume of the CsI scintillation crystal is 285 cm^3. This results in a detector weight of approximately 1.4 kg, including the aluminium housing with a thickness of 0.8 mm at the entrance window of the detector.

3.1.2.6.1 Silicon Photomultiplier

Usually, scintillation detectors require a photomultiplier tube (PMT) to amplify the signal caused by the light-output from the crystal. However, a PMT is large and heavy. Therefore, it is better to use silicon photomultipliers (SiPM) that are smaller and lighter. Their downside is that the resolution of the spectra will be slightly worse, but since we are already using a CsI detector, the reduced resolution will have a limited influence, as shown in [54-57], [103-105]

Figure 45 gives a schematic overview of the detector system and the necessary connections between all the components. Figure 46 shows the technical drawing

of the detector. In Figure 47a and b, the final product can be seen mounted on the fiberglass interface plate to mount it in the drone.

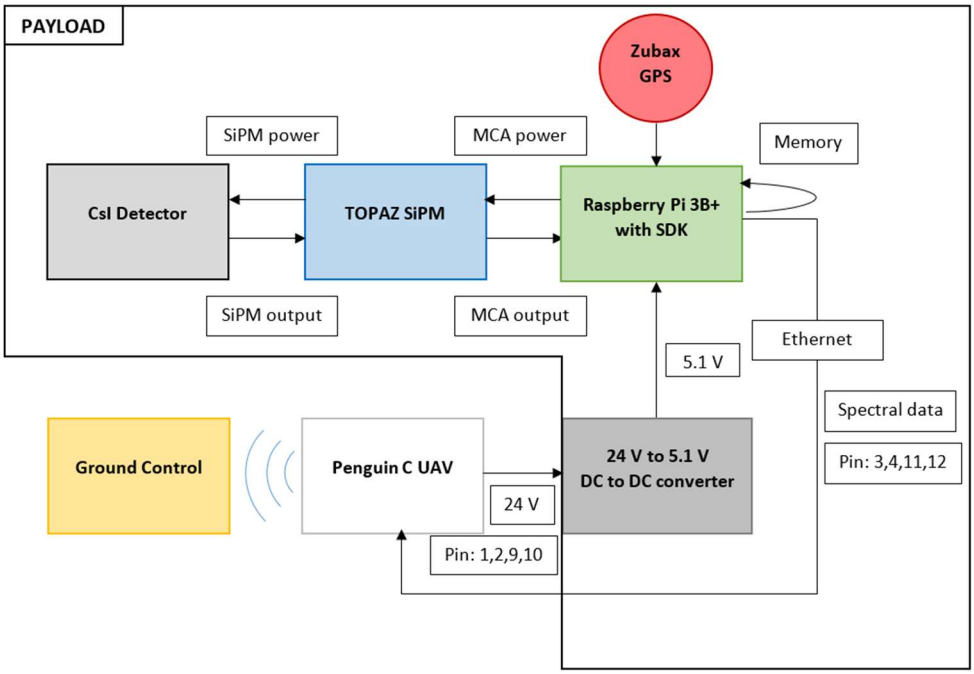

Figure 45: Schematic of the detector system and connection to the Penguin C UAV for remote communication.

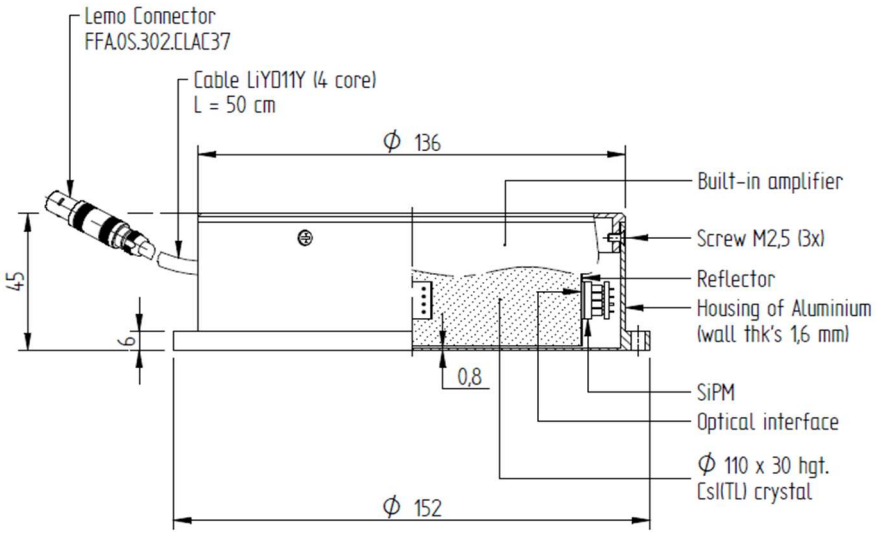

Figure 46: Technical drawing of the fixed-wing CsI detector made by Scionix Holland B.V. (mm when no unit is given).

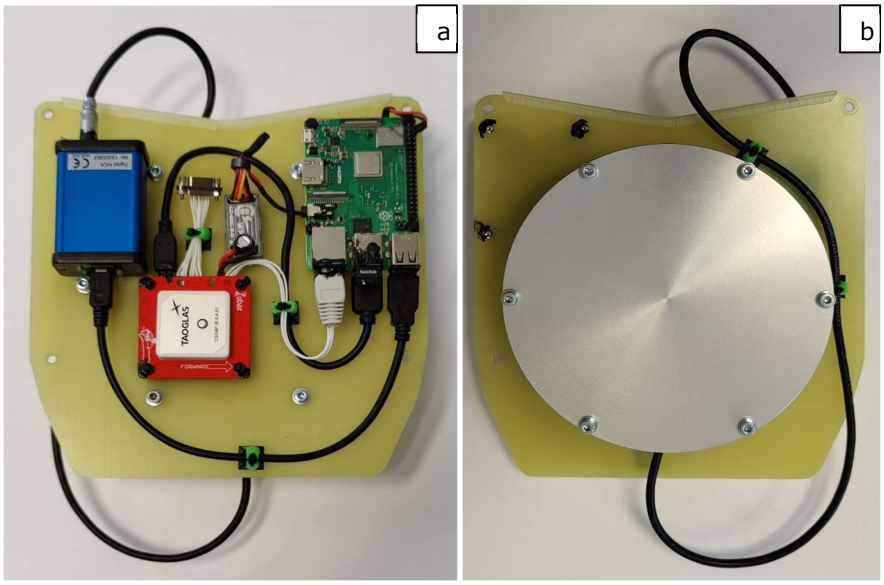

Figure 47: (a) Detector system electronics. Brightspec SiPM multi-channel analyser (blue), Zubax GNSS 2.0 (red), Raspberry Pi 3 B+ (green), BEC 2.0 DC-DC converter (grey). (b) Scionix CsI detector with SiPMs and aluminium housing.

3.1.2.6.2 Topaz SiPM Multi Channel Analyzer

The Brightspec Topaz-SiPM multichannel analyser (MCA) is developed specifically for scintillation detectors that use SiPMs. The MCA uses 1024 channels, but the number of channels can be increased to 4096 channels if necessary. However, since spectra of approximately 1-s integration time are recorded, most of the channels will contain zero counts, and therefore 1024 channels are sufficient. The MCA is controlled by the Raspberry Pi using Python and the C++ library from Brightspec [106], [107].

3.1.2.6.3 Raspberry Pi and Peripherals

The Raspberry Pi 3B+ is a single-board computer with the Raspbian operating system. When the payload/detector is turned on, a Python script is initiated automatically on this computer. The script reads GPS coordinates from the Zubax GPS module together with the date and time in UTC, the above-mean-sea-level (AMSL) height, and the pressure. From the MCA, the spectrum together with the live and real-time of the measurement are obtained. With this data, a text file is created and saved in the Raspberry Pi's memory. In addition to being stored on the Raspberry Pi, the text file is also sent to the ground control station to provide data for a live feed.

The Zubax GNSS 2.0 [108] is a GPS module specifically designed to be used in combination with UAVs or drones. The outputs are divided into multiple lines that show the GNSS data (Global Navigation Satellite System). Among these data, there are latitude, longitude, AMSL height, UTC time, date, magnetic heading, and pressure. The data obtained from the GPS module are then read by the Raspberry Pi and added to the text file containing the spectrum. The BEC 2.0 DC-DC converter is used to reduce the 24 V coming from the drone to the 5.1 V that is required to power the Raspberry Pi.

3.1.2.6.4 Detector Integration

The detector system is located in the front of the drone in a fiberglass casing of 0.85-mm thickness to protect it from wind and rain. It also has dampers to counteract vibrations and shocks. These measures are necessary to avoid damage to the detector system. We verified that the possible attenuation due to the encasement will be limited to less than 1% for the gamma energy of K-40 (1460.8 keV) by Monte Carlo simulations using Penelope. The detector and the drone are connected by a micro-D connector to make sure they will not detach due to vibrations.

3.1.2.7 Fixed-wing Detector System by Car

As a first test we fixed the detector system to a car and drove around the SCK CEN. The GPS module was mounted on the roof of the car to provide enough field of view to achieve connection to at least 4 GPS-satellites. The results and findings of this measurement can be found in chapter 8.3 in Figure 80.

3.1.2.8 Theoretical Framework

Following Beck et al. [65] ,we find that Equation 8 requires three factors: (1) the angular dependence, (2) the efficiency, and (3) the theoretical distribution of the

source in the soil. For K-40 measurements, the theoretical distribution is homogeneous in depth. However, for contaminations that originate from incidents, it is possible to define the distribution as an exponential function.

The first two factors have to be determined experimentally using point sources and measurements under different angles. Monte Carlo calculations, as used during the optimization process, can be used to determine the first two factors in Equation 6. However, for a real detector with its housing, exact position of crystal, and SiPMs, it was decided to determine these factors experimentally. For the angular dependence and the full energy peak efficiency η, we used a europium-152 (Eu-152) point source. The full peak energy efficiency is given as

$$\eta = \frac{c}{A\, t\, \varepsilon} \qquad (7)$$

where c is the number of net counts in the gamma peak, A the activity of the point source at the time of the measurement in Bq, t live time of the measurement in s, and ε the gamma ray intensity. For the angular dependence, multiple measurements were taken with a constant distance between the source and the detector but under different angles ranging from 0° to 90°, with 0° normal to the detector surface, Figure 48 shows a schematic of the setup. For the full energy peak efficiency, we used the measurement at 0°. Eu-152 was chosen because it has multiple gamma ray energies, mainly between 122 and 1408 keV, allowing for the determination of these factors for a wide range of gamma energies. Additionally, the peak at 1408 keV is relatively close to the 1460-keV peak coming from K-40 which is the nuclide used for testing the methodology for quantifying the concentration in soil. Therefore, the 1408 keV line was used to calculate the relative angular dependence. The full energy peak efficiency and the angular dependency are shown in respectively Figure 49 and Figure 50.

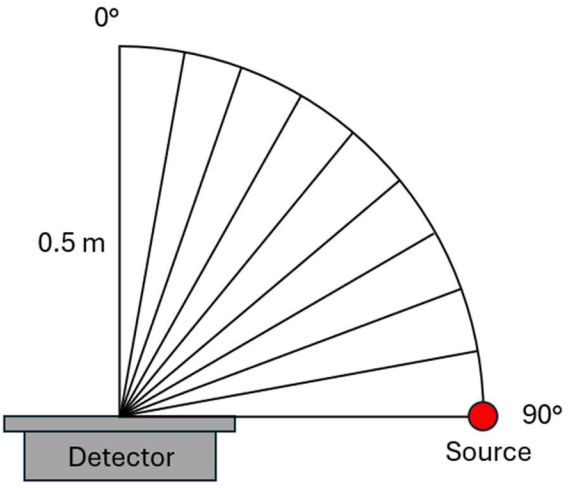

Figure 48: Measurement setup for the angular dependence of the fixed-wing detector.

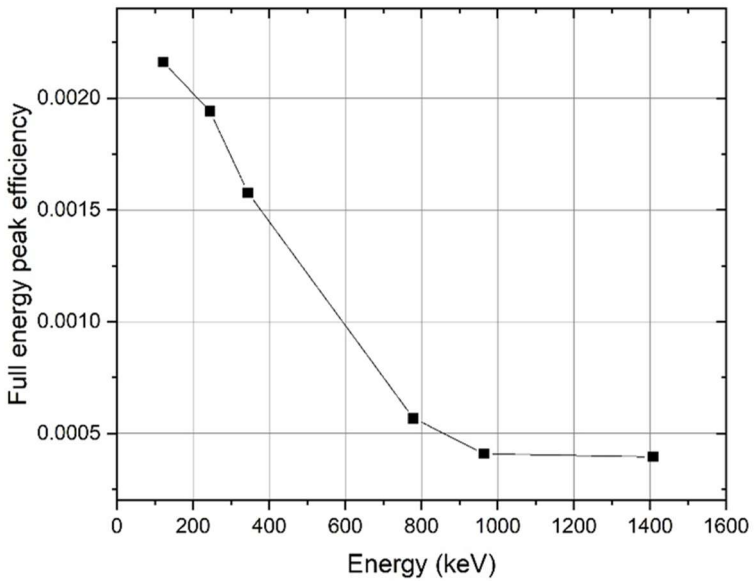

Figure 49: Full energy peak efficiency experimentally determined with a Eu-152 point source positioned 50 cm under the detector.

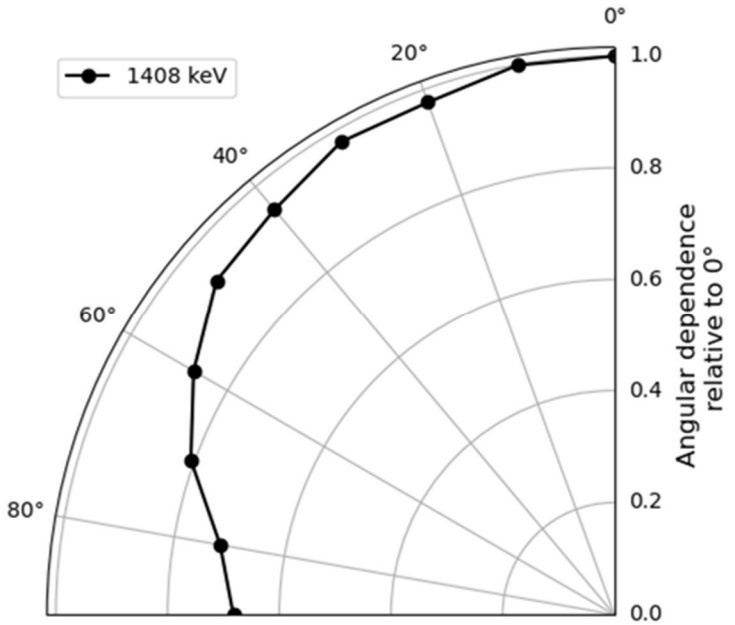

Figure 50: Relative angular dependence to 0° for the full energy peak efficiency of 1408 keV from a Eu-152 point source.

The last factor of Equation 6 can be determined by calculating the theoretical flux at the detector location. We start with the equation for the theoretical flux coming from a point source at a distance R (m) and an activity S_0 (Bq), as can be seen in Equation 8. Herein, we adapt the source term by incorporating the exponential distribution in the soil and the self-attenuating effects. However, the point source used Cartesian coordinates while polar coordinates will be of more use to incorporate the angular dependency of the detector. Therefore, we substitute the Cartesian integrals with their polar counterparts. After integrating over the azimuthal angle, this results in Equation 9.

$$\varphi_{point}(R) = \frac{S_0}{4\pi R^2}\, e^{-\mu_a R} \qquad (8)$$

$$\varphi_{soil}(r,\theta) = 2\pi \int_0^{\pi/2} \int_{h/\omega}^{\infty} \frac{S_0}{4\pi r^2}\, e^{-\left(\frac{\alpha}{\rho}\right)\rho z}\, r^2\, sin\, sin\, \theta\, e^{-\mu_s\left(r-\frac{h}{\omega}\right)}\, e^{-\mu_a\left(\frac{h}{\omega}\right)}\, dr\, d\theta \qquad (9)$$

In Equation 9, r is the distance from each element of differential volume to the detector position in m, h is the height above ground in m, $\omega = cos\, cos\, \theta$ with θ the angle of the photon incident on the detector, z is the depth beneath the surface in cm, S_0 is the surface activity in $photons/cm^2\, s$, α is the reciprocal of the relaxation length of the approximately exponentially distributed source activity with depth in cm^{-1}, ρ and ρ_a are respectively the soil and air density expressed in g/cm^3, and μ_a and μ_s are respectively the air and soil mass attenuation coefficients in cm^{-1}. By integration over r and moving from θ to ω, we obtain Equation 10.

$$\varphi = \int_0^1 \frac{S_0/\rho}{2} \left(\frac{1}{\left(\frac{\alpha}{\rho}\right)\omega + \left(\frac{\mu_s}{\rho}\right)} \right) e^{\left(-\frac{\left(\frac{\mu_a}{\rho_a}\right)(h\rho_a)}{\omega} \right)} d\omega \qquad (10)$$

In the work of Beck et al., an exponential function is used to define the activity as a function of depth with an exponent α/ρ. However, for naturally occurring radioactivity, such as K-40 in soil, this exponent is equal to zero since K-40 can be assumed to be homogeneously distributed with respect to depth. A full derivation of equation 10 can be found in chapter 8.5.

3.1.2.9 Topography

One of the factors that influences the results obtained by the theoretical framework of Beck et al. is the topography of the area of interest. In case of terrain that cannot be assumed flat, the results need to be corrected for the roughness and irregularities found in the region [109]. Using height maps from the region obtained from Geopunt Vlaanderen [98], it is clear that there are only slight differences in height over the measurement site. The changes have a maximum value of 2.3 m or 1.1 % of the flight height of 209.9 m. Therefore, it is assumed that the topography has no significant influence on the measurements over this region regarding the attenuation of soil. However, the changes in the height above ground do have a significant influence due to the attenuation of air and therefore have to be accounted for by a height correction. This is different in the sense that the topography correction would correct for radiation coming from

higher areas or areas that attenuate the contamination. Meanwhile, the height correction is only correcting for the above ground level (AGL) height. The AGL height is calculated by obtaining the AMSL height from the drone and subtracting the average AMSL height of the topography.

3.1.2.10 Ground Measurement and Samples

Samples and a ground measurement were done at a nearby field. A measurement at 1 m height was done using a tripod and the fixed-wing detector. After the measurement, three samples were taken at a 4.5 m radius around the detector location. Each soil sample weight approximately 1 kg. The K-40 concentration of each sample was measured using a HPGe detector at the Laboratory for Gamma Spectrometry at the SCK CEN.

3.1.3 Results

The test flights were performed above Droneport Sint-Truiden (50°47’31”N 005°12’06”E) [110]. Droneport is a small airfield that combines both the flight control of small airplanes (e.g., logistics of personal aircraft) and UAVs (e.g., logistics of multicopter and fixed-wing drones). The test flights had different objectives; firstly, to demonstrate the good functioning of the detector–drone system (data collection, transmission, etc.), and secondly to test the reproducibility of results collected during the flight, and, finally, to demonstrate that quantitative results can be obtained with the system if a source geometry can be assumed.

A first flight to evaluate the performance of the Penguin C UAV and CsI detector took place at Droneport in Sint-Truiden, Belgium on 7 October 2021. After a calibration and check-up of both the UAV and the detector system, the Penguin C drone was launched. The detector system was powered off during the launch to avoid any interference. After the take-off, the detector system was turned on and a connection to the ground control station was established. Thereafter, a circular flight pattern was executed at multiple heights.

On a second flight on 22 January 2022, we used the same flight plan as in the first to verify the reproducibility of the flights and measurements and to collect more data as a function of the detector height above ground. In the second part of this flight, a grid pattern flight path was used to investigate the implications on the measurements regarding tilt angle and turning radius. The tilt angle is influenced by the turning radius and alters the geometry from a detector parallel to the ground to a geometry with a tilted detector relative to the ground. This can be corrected with the use of the tilt angle coming from the UAV log files and the angular dependence. However, for grid patterns, the tilt angle will be 0° for the straight flight lines. Only during the changes in direction will it have an influence on the detector geometry and since these changes happen outside the border of the area of investigation, their impact on the overall results will be limited.

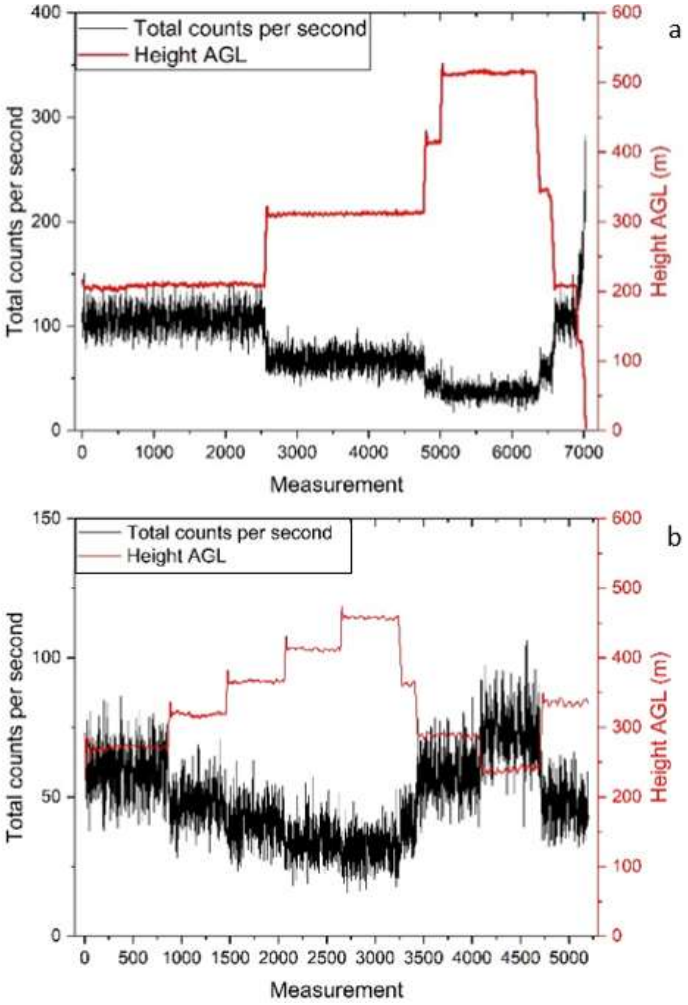

Figure 51: Total number of counts per second compared to the height above ground level in m for flight 1 (a) and flight 2 (b).

Figure 51 a and b show the total counts per second for every measurement at different heights and illustrates how the changes in height influence the number of counts per second. We can clearly see the inverse connection between the height of the drone and the total number of counts per second. However, in Figure 52 a and b, the only clear K-40 peak is visible for the AGL height of 209.9 m. The K-40 peak at 311.4 m is still measurable but at higher altitudes it was not possible to measure a net peak count.

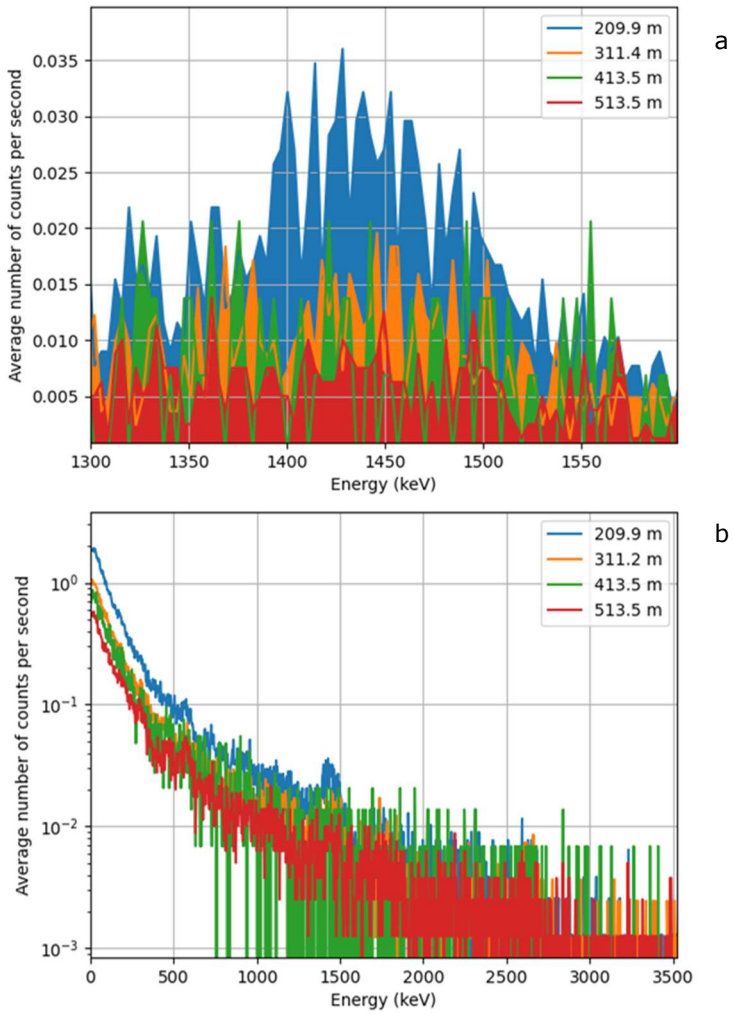

Figure 52: a) Average number of counts per second at different heights zoomed in on the K-40 peak (1460 keV) on a linear scale. b) Average number of counts per second at different heights shown on a logarithmic scale.

In these spectra, the gamma peak of K-40 at 1460 keV is visible and is used to calculate the K-40 concentration. To verify our calculated results, three samples were taken near the site of measurement. The results from these samples are shown in Table 8. The obtained results were verified by using the samples taken by FANC (Federal Agency for Nuclear Control) at multiple sites in Belgium [111]. Figure 53 a and b show the flight paths of both flights. For the heights between 209.9 m and 311.4 m, we were able to find a K-40 peak. In Table 9, the K-40 peaks are used to calculate the K-40 concentrations and compare them with the concentrations of the ground samples. The efficiency is corrected from 1408 keV to 1460.8 keV by Monte Carlo simulations. Two simulations were executed with a

point source and the final detector geometry, but one with an energy of 1408 keV and another one with an energy of 1460.8 keV. The detector efficiencies of both simulations were then taken, and the ratio of both efficiencies used to correct for the efficiency used in Equation 6. At higher altitudes, the gamma rays of K-40 are more strongly attenuated and therefore they cannot be seen in these spectra.

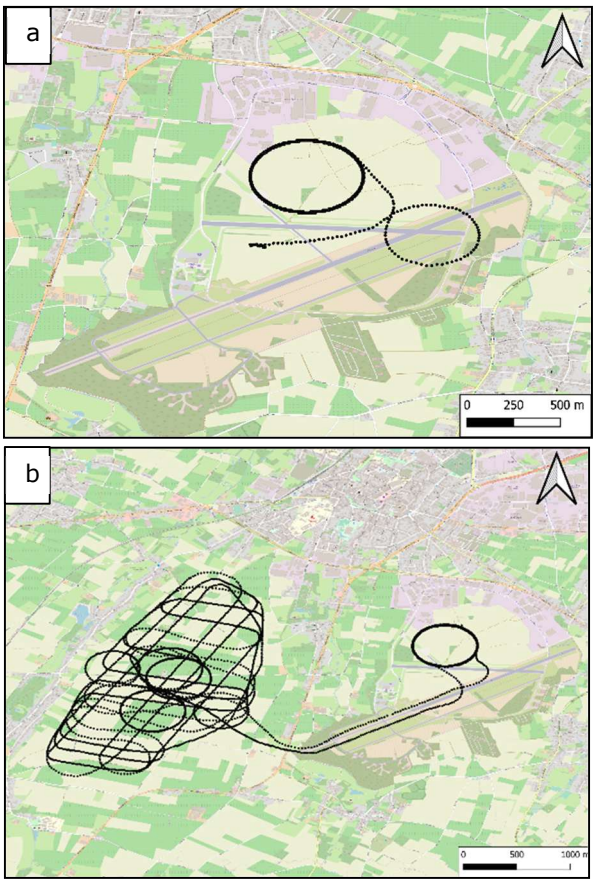

Figure 53: (a) Flight path of the first flight with the circular pattern. (b) Flight path of the second flight with the circular pattern and the grid pattern.

Table 8: Table with sampled concentration data and their uncertainties.

ID	K-40 Concentration (Bq/kg)	Uncertainty (Bq/kg) (1σ)
1	500	30
2	460	30
3	460	25
Average	**473**	**16**

Using Equation 10, the theoretical fluxes from a homogeneously distributed source were calculated at different flight heights. The theoretical flux can then be used together with the full energy peak efficiency and the counts per seconds from the K-40 peak to calculate the concentration at the ground using Equation 6. Results are shown in Table 5. The uncertainty in the concentration is mainly caused by the limited number of counts in the K-40 peak.

A measurement at the site of the sampling was executed and in the same way as with the drone measurements, a K-40 concentration was calculated. At a height of 1 m, we measured a net peak counting rate of 4.945 ± 0.052 counts per second and calculated a theoretical flux of 0.83 ± 0.04 gammas/cm² s. These values give us the corresponding K-40 concentration of 492.6 ± 28.4 Bq/kg. All uncertainties are for one standard deviation.

Table 9: Table comparing K-40 concentration measurements at multiple heights with the sampled concentration of K-40 shown in Table 8.

Height (m)	Net Counts per Second in K-40 Peak (cps)	Uncertainty Net Counts per Second in K-40 Peak (%)	Theoretical Flux Calculated with Equation (10) (Gammas/s.cm²)	K-40 Concentration (Bq/kg)	Uncertainty K-40 Concentration (%) (1 σ)	Relative Difference from Sampled Concentration (%)
209.9	0.5994	4.6	0.083	604.4	7.2	27.8
239.1	0.4660	6.2	0.065	600.0	8.3	26.8
271.7	0.3666	6.5	0.049	626.1	8.6	32.4
288.4	0.3172	8.2	0.043	617.4	9.9	30.5
311.4	0.2927	6.5	0.036	680.4	8.6	43.9

3.1.4 Discussion

The drone–detector system for radiological monitoring as presented here started from the pre-requisite to be a system with a long flight autonomy (more than 8 h, ideally 12 h) and an extended range of operation. The range should allow for operating the system remotely from a safe location in case of a nuclear or radiological emergency. Autonomy is important to guarantee continuous surveillance and minimal downtime to recharge or refuel. During the Fukushima accident, for example, releases to the environment continued for two weeks [40], [112]. Having remote access to data during this period with flights over different areas and different altitudes, depending on, e.g., the meteorological situation, with a drone–detector system as described here, would have been an important asset in the radiation protection strategy. Further, the system has been designed to be flexible: the UAV is launched by catapult and recuperated with a parachute from nearly all locations with limited resources needed. The used flight patterns are chosen for specific reasons. The circular flight patterns can be used for monitoring an installation and detecting possible anomalies, while the grid pattern can be used to map contaminated sites or to search for lost sources.

The restrictions defined in the certificate of conformity of the UAV put limitations on the payload available for the radiation detection system. The radiation detection system was fully optimized to yield the highest efficiency for the available payload. Both the type of detector as well as its size were optimized. To allow radionuclide identification, only detection methods allowing gamma spectroscopy have been included in this optimization process. The optimization using the Penelope Monte Carlo code allowed us to further investigate the detector efficiency and solid angle for four detector materials: LaBr, CeBr, CsI, and NaI. The best detector option was a CsI using SiPMs with a miniature MCA. Other detector materials, such as HPGe or CZT, have drawbacks, e.g., cooling or limited volumes, and were not included in the simulations.

The detector takes a spectrum every second. The one-second spectra create a flexible data flow in which we can combine several spectra for increased statistics since the statistics for the one-second spectra are very limited.

The results in Table 8 are within the range as stated by FANC [111]. The calculated concentrations from the UAV measurements can differ somewhat from the samples due to the differences in sampled area, as is also the case for measurements at different heights due to a different field of view. However, for the measurement at 1 m height, the result agrees well with the ground sample concentrations.

The sensitivity of the system is dependent on the altitude. We can use this to our advantage to obtain a required sensitivity for a specific case or during radiological releases by flying at higher altitudes to avoid contamination. If sensitivity is important, we can use the repeatability of the flight controller software to accumulate statistics, similar to what was done for K-40. The drone–detector combination can also be used for other applications, such as the screening for

radiation and/or radioactivity during public events in the context of security, locating orphan radioactive sources, or radiological mapping of large areas such as legacy uranium mines. For the location of orphan radioactive sources, the system could scan large areas to obtain an area of interest which can be scanned more accurately using a multicopter drone. This application will require more extensive knowledge on the minimum detectable activities of the detector. The radiological mapping of large areas can be done in a similar way to what was done for K-40 in this paper. However, to obtain a correct calibration, it might be more useful to work with calibration pads, especially for uranium or thorium mines. Their energies are significantly higher, and it would be difficult to get a full energy peak efficiency for these energies using point sources.

3.2 The Fixed-wing Detector System in a Realistic Radiological Scenario

A standard tool for radiological monitoring is the Telerad network, a network of radiation detectors spread over Belgium. To see if the detector system, described in the previous chapter, could aid in the information obtained from the Telerad network, a comparison between the detector system and a Telerad station was done.

Hereafter, the drone-detector system still had to be tested in a more complex scenario. The measurements done over Droneport Sint-Truiden, were relatively simple, one nearly homogeneous K-40 source. In the next chapter, the drone-detector system will be tested by a measurement campaign over the SCK CEN. There are several radioactive sources over the area under investigation, such as storage for radioactive waste, atmospheric releases of Ar-41 from the BR1 reactor and legacy contaminations from other site .

One of the goals was to verify if the drone-detector system could distinguish static sources (like the radioactive waste) from shifting sources (like the radiological Ar-41 plume). The routine Ar-41 releases from the BR1 are far below the limits set by the FANC (Federal Agency for Nuclear Control). Per year, the maximum dose a person could receive from the operation of the BR1 cannot be greater than 10 µSv [113]. This is to show that we will certainly be able to measure emergency releases that would probably be significantly higher.

3.2.1 Methods and Materials

3.2.1.1 BR1

The BR1 (Belgian Reactor 1) was built in 1956 and was the first reactor built in Belgium. It is located at the SCK CEN in Mol and is currently still in use for research and training purposes. The BR1 is an air-cooled graphite moderated reactor. The fissile material, natural uranium, is placed in the 6.84 m by 6.84 m by 6.66 m graphite block with holes for the reactor tubes and separate holes for cooling. Because the BR1 is air-cooled the air exiting the reactor will be activated. One of the nuclides that are released through a stack is Ar-41, coming from the activation of the noble-gas Ar-40, which is present in air for 0.934 vol% and 1.29 wt%. Ar-41 decays through beta-minus decay with a half-life of 1.83 hours. It also has a gamma ray of 1294 keV with an intensity of 99.16% [61], [114].

3.2.1.2 Telerad

The Telerad network is an automated radiation detection network operated by the Federal Agency for Nuclear Control (FANC) in Belgium. It consists of approximately 254 detector stations spread over Belgium with higher densities around nuclear installations. Measurement stations contain a Geiger counter for dose rate measurements and some of the stations also have a cylindrical NaI scintillator spectrometer of 1.5” by 1.5” for nuclide identification and dose rate assessment, the spectra from this detector have 2048 channels. The volume of

the NaI scintillation detector is 43.4 cm³. The data is available online and can be used for the continuous monitoring of the measurement stations. In this test, Telerad station IMR-M11 located at the premises of the SCK CEN was used to compare with the fixed-wing detector system [115].

3.2.1.3 Fixed-wing Detector System

The fixed-wing detector system is explained in depth in chapter 3.1.2.4.

3.2.1.4 Measurements from the Ground

The fixed-wing detector system was placed on a tripod right next to Telerad station IMR-M11 located at the premises of SCK CEN. The location of the measurement was chosen in relation to the wind on the day of the measurement to make sure the Ar-41 plume was measurable. While the BR1 was running, we started a measurement over 80 minutes to compare with the data from the Telerad station.

3.2.1.5 Air-borne Measurements: Fixed-wing Flights over SCK CEN

The fixed-wing detector system with the Penguin C fixed-wing UAV was used to fly over the SCK CEN in a training exercise. It launched from a nearby field West from the SCK CEN. The BR1 produced Ar-41 which was released through the stack. The measurements were done in circles with radii from 300 m to 800 m with increases of 100 m and the BR1 stack in the centre. The height AGL was 200 m meaning that the distance between the top of the stack (60 m) and the drone was 140 m.

3.2.1.6 Analysis Methods

The spectra per second for the fixed-wing detector and per 10 minutes for the Telerad detector were summed to obtain a single spectrum for each detector. Next, a rebinning of the Telerad spectrum was necessary. The Telerad spectrum has 2048 channels which is twice the number of channels for the fixed-wing detector. On the spectra, Gaussian distributions were fitted to all peaks. The downward slope was accounted for by adding a linear slope to the fit with the mean of the outer five measurement points on both sides taken as reference. The net count rate was calculated using the fitted Gaussian distribution. The full width half maximum can easily be calculated using equation 11, with σ being the standard deviation of the gaussian fit [22]. The count rate was calculated by dividing the net count rate by the summed real time of the spectra. Normally the live time would be used, but the Telerad data does not contain the live time per spectrum. However, since the count rates are relatively low, the difference between the real and live time will be small or even neglectable.

$$FWHM = 2\sqrt{2\ln(2)}\,\sigma \qquad (11)$$

3.2.2 Results

In Figure 54 the spectrum of the fixed-wing system and the rebinned spectrum of the Telerad station are shown. The real time of both measurements is the same. Something that is clearly visible in the spectrum is the increased number of counts

in the fixed-wing system. We can also see the Ar-41 peak at 1293.6 keV and the K-40 peak at 1460.8 keV in both spectra. The Th-232 peak at 2614.5 keV is clearly visible for the fixed-wing detector and there is an increase in counts for the Telerad detector.

The NaI detector from the Telerad station has a FWHM of 66.4 keV at 1293.6 keV (Ar-41) or 5.1 %. For the CsI fixed-wing detector the FWHM at 1293.6 keV (Ar-41) is approximately 82.7 keV or 6.4 %. The number of net counts and counts per second can be found in Table 10.

Table 10: Net counts, count rates and FWHM from the comparison between the fixed-wing detector system and the Telerad detector for the main gamma peaks of Ar-41, K-40 and Th-232. The data that was not filled in could not be calculated due to lack of counts in the spectrum.

Nuclide	Fixed-wing System			Telerad Detector		
	Net Counts	Count Rate (cps)	FWHM (keV)	Net Counts	Count Rate (cps)	FWHM (keV)
Ar-41	42797	8.92	82.7	5653	1.18	66.4
K-40	4393	0.92	84.3	1013	0.21	70.3
Th-232	853	0.18	/	123	0.03	/

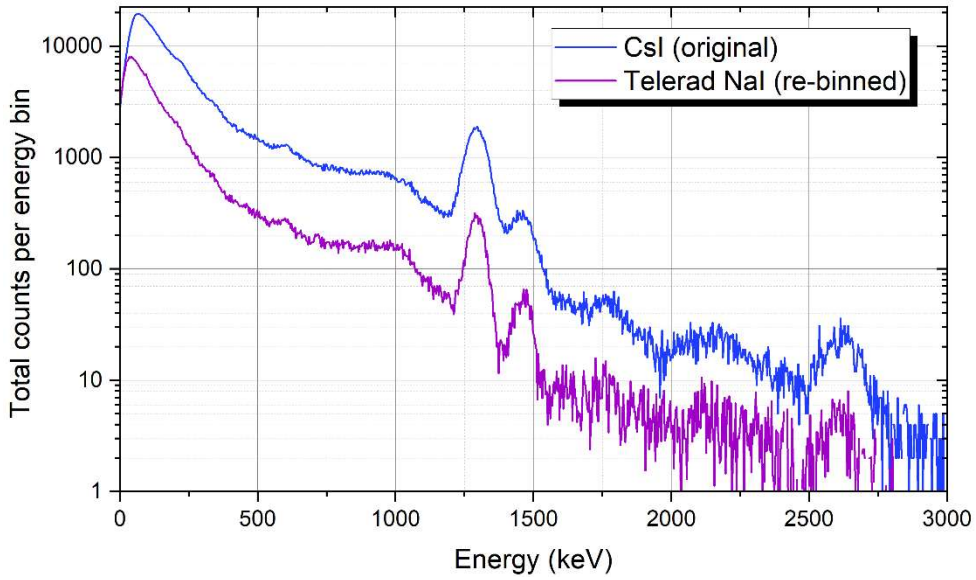

Figure 54: Spectra from the fixed-wing and the Telerad spectroscopy detectors. The measurement was taken over a time of 80 minutes.

Figure 55 shows the measurement over the SCK CEN with the fixed-wing drone. The measurement points were averaged out over sectors of 10 degrees. In Figure 55 there are three separated hotspots around the centrum of the flight lines. The one in the north (A) is the site of Belgoprocess. The hotspot in the east (B) is the Solarium containing large deposits of radium-226. The hotspot in the south-west (C) is due to the BR1 plume containing Ar-41. The atmospheric dispersion simulation in ambient dose equivalent rate is also made visible which corresponds well to the measurements from the fixed-wing detector system. Distinguishing the stationary sources and the plume can easily be achieved when the BR1 would be turned off. The stationary sources will remain present and the Ar-41 plume will disperse and vanish. The ambient dose equivalent rate was calculated using a gaussian plume model, ADDER (Atmospheric Dispersion and Dose Equivalent Rates), made by Frankemölle et al. [116], [117]. In Figure 55, the colorbar on the right shows the background corrected ambient dose equivalent rates. In the overlay of the map, the dose rates caused by the plume are visible going to the south-west.

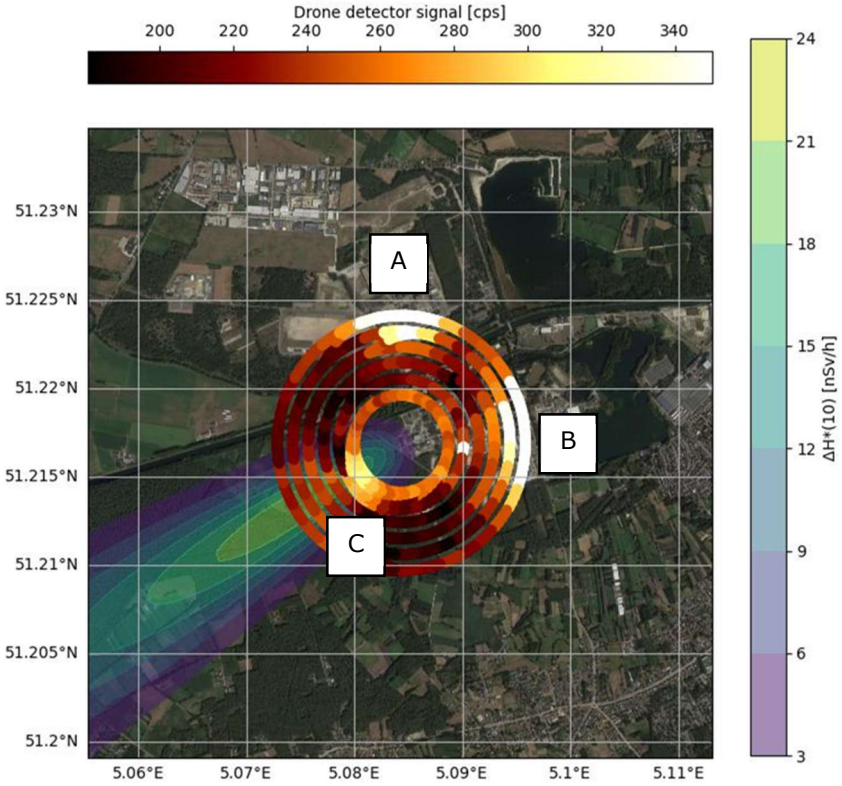

Figure 55: Fixed-wing detector system results from the Penguin C flight over the SCK CEN site. The circles start with a radius of 300 m up to 800 m in steps of 100 m. The height AGL of the drone was 200 m. The atmospheric dispersion is visible and expressed as ambient does equivalent rate H(10). The hotspot in the north is the site of Belgoprocess and the hotspot on the east is due to the Solarium which is a Ra-226 storage.*

In Figure 56, a 1-second-spectrum and a summed spectrum of 10 spectra are shown from the fixed-wing flight over the SCK. In the orange 1-second-spectrum are no clear peaks visible due to the short measurement time. However, by combining several spectra, as is done in the blue summed spectrum, a small peak can be discerned at roughly 1294 keV (black arrow), this energy corresponds to the gamma energy originating from Ar-41.

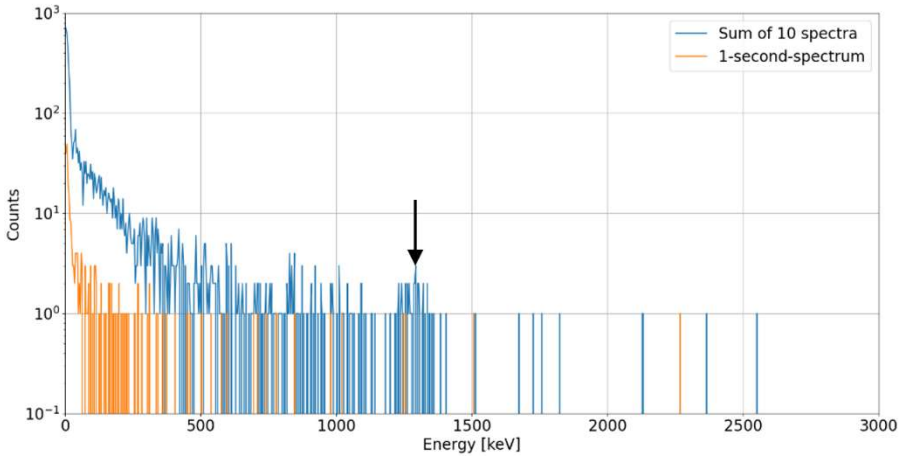

Figure 56: 1-second-spectrum and summed spectrum of 10 spectra from the fixed-wing flight over the SCK CEN. The black arrow shows the increase in count rate for the summed spectrum.

3.2.3 Discussion

When comparing the Telerad detector with the fixed-wing detector system three things can be noticed. Firstly, the number of net counts and count rate is significantly lower for the Telerad detector. This is mainly due to the difference between the volume of the fixed-wing detector, 285 cm^3, and the volume of the Telerad detector, 43.4 cm^3, which is a factor 6.5 smaller. However, the difference between the net counts and count rate is even larger, namely a factor of 7.9. This is due to the optimal shape of the fixed-wing detector that was designed specifically for these types of measurements with energies in the range of the gamma peak of Ar-41 (1293.6 keV). Secondly, a downside of the fixed-wing detector made from CsI, is the energy resolution. As is visible in Table 10, FWHM of the Telerad detector is significantly better than the FWHM of the fixed-wing detector.

3.2.4 Conclusion

The results from the flight over the SCK CEN show how the detector system can be used in a real scenario. The added complexity of stationary sources, like the Belgoprocess site and the Solarium, mixed with the radiological plume created an opportunity to show the differentiation capabilities of the detector system. It can measure both ground contaminations at height differences of 200 m and radiological plumes at approximately 140 m in vertical distance. This can be of great use in situations where large areas are contaminated and are in need of a radiological survey. The fixed-wing detector system can easily cover several km^2 in hours without the need of endangering operators. However, the spatial resolution of the fixed-wing system might not suffice as it is strongly dependent on the flight height, therefore, smaller drone-detector systems could be used as

supplementary systems to increase the spatial resolution at specific areas of interest. The smaller systems typically have a lower flight height which improves the spatial resolution. Alternatively, operators or UGV can be used to survey these areas to improve the spatial resolution even further. The fixed-wing detector system should not be viewed as a replacement of the systems that are currently used, but rather as an additional tool in radiological monitoring. It can provide additional data for gaussian plume modelling or aid in decision making in case of an emergency. Future research should be focussed on deconvolution of the obtained data and spectroscopy with low counting statistics, as is visible in Figure 56. Both subjects would greatly improve the spatial resolution and uncertainty of the fixed-wing detector system.

3.3 Conclusions on Objective 2

Objective 2 was split into sub-objective 2a, optimization of a detector system for a specific UAV and source, and sub-objective 2b, test and verify the optimized system in realistic scenarios for radiological or nuclear emergencies. An optimal detector system for the Penguin C UAV was found by simulation using Monte Carlo simulations, verified by point source experiments and proven to work in two scenarios. These scenarios represented a ground contamination and a more complex scenario in an industrial environment with permanent sources and a temporary source, i.e. a radiological release of Ar-41.

Sub-objective 2a was reached by using the Monte Carlo code Penelope. With Penelope several detector materials and geometries were simulated. The limits of the simulation were set based on the maximum data from the UAV. For the Penguin C the weight limit was set to 2 kg of payload of which 1 kg was set to be the detector crystals weight. Through the Monte Carlo simulations, the optimal detector geometry and material was found to be a cylindrical CsI scintillation detector with a diameter of 5 cm and a thickness of 3 cm. As final design the detector dimensions were set to a diameter of 5.5 cm and a thickness of 3 cm as the rest of the payload ended up weighing less than expected. Additional simulations with a more correct source to detector distance might change the detector geometry of the optimal detector. However, the material, CsI, has a significantly higher efficiency as the other simulated materials. Simulations with additional detector materials, different weight limits or different gamma ray energies will certainly be interesting and might provide different optimal configurations for those parameters.

Sub-objective 2b was achieved by performing two measurement campaigns. A first campaign was done over the fields surrounding Droneport in Sint-Truiden, Belgium with the Penguin C, a fixed-wing UAV. The K-40 concentrations on the fields were measured by flying over them with the detector system mentioned in the paragraph above. The spectra from the measurement were then converted to concentrations using the theoretical framework described in chapter 3.1.2.8. Hereafter, samples were taken from surrounding fields. From the samples, K-40 concentrations were measured through HPGe measurements in the laboratory of the SCK CEN. Although the UAV results do not agree completely with the

concentrations measured from the samples, the UAV measurements give a good estimate of the K-40 concentrations. Improving the accuracy of the concentrations measured by the UAV detector system might be accomplished by flying lower and at lower speeds. However, the Penguin C fixed-wing UAV does not have the capability to do this safely.

Additional measurements for the angular dependence and full energy peak efficiency will improve the detectors capabilities in scanning large areas and calculating the concentrations. Incorporation of the tilt angle of the drone in the concentration calculations will also aid in the improvement of the detector system. Furthermore, it is advised to improve the detector system to be independent of the Penguin C by incorporating a separate power supply and a separate tool for communication. Doing so, will make the detector system more flexible and allow it to work for different UAVs or even UGVs. Lastly, future research should focus on using deconvolution techniques, as is shown by Billings et al. [99], these techniques will certainly improve the spatial resolution of the system.

The second measurement campaign, over the site of the SCK CEN and the surrounding industrial areas, was used to test a more complex scenario. The surrounding areas have several permanent radiological sources. An additional source, the Ar-41 plume from the BR1 stack, was present during the measurements. This source would disperse and vanish when the BR1 was turned off, while the stationary sources remain present.

4 Drone-Detector System for Detailed Investigations

For detailed investigations, some aspects of the flight can be adapted. The UAV can hoover in place to obtain better spectra which allows us to better identify the source. Lowering the altitude of the UAV will improve the spatial resolution and improve the efficiency of the measurements. Aside from the flight parameters, the detector system can also be adapted. Increasing the size of the detector system will improve its efficiency when done correctly. Alternatively, the directionality can be improved by either detector placement or collimation.

In this chapter we will first investigate the feasibility of a directional detector system mounted underneath a drone. This also covers sub-objective 3a, by proving the chosen method works without using shielding or collimation. The tests done to prove the feasibility of this method can be found in chapter 4.1. Chapter 4.2 will provide experimental results that were achieved by using an algorithm specific for the directional detector configuration.

4.1 Proof of Concept

4.1.1 Introduction

A multicopter drone or UAV is more agile and steady as its fixed-wing counterpart. They can hover in place or move freely in three dimensions. Fixed-wing UAVs have the advantage of speed and flight time. Multicopter drones can be used to scan smaller areas that have been marked as points of interest by the fixed-wing drones to identify and specify the origin of the measured radiation. However, since the multicopter drones have a limited flight time and payload, it is of interest to optimize the scanning patterns. Whether it is for a surface contamination or a lost source, the detector configuration and flight path can be optimized to achieve a fast and accurate scan of the region of interest. In this chapter we will focus on the detector configuration. We have built a detector system consisting of three identical cylindrical CsI scintillator detectors. The three detectors were placed in a triangular shape causing them to shield each other. Reading out the detectors in this specific orientation means that we could identify the direction the radiation was coming from.

Chen et al. [70] proved that a directional detector mounted underneath an unmanned helicopter could aid in localisation of radioactive sources. Their system, ARDUO, uses eight identical CsI(Tl) scintillation detectors of 2.8 cm by 2.8 cm by 5.6 cm placed in a 2x2x2 matrix. Each detector has a SiPM for detecting the light pulses. The detectors shield each other making it possible to derive directional information from their responses. Other papers like Willis et al. or Schemm et al. [72], [73] provided us with calibration methods for our detector configuration.

Carr et al. [71] used a different setup, their system uses a single Sigma 50 detector from Kromek or a GR1 detector from Kromek, both with a tungsten collimator with an opening pointing upwards. The CsI detector is 1 by 1 by 2 inches and uses a SiPM to read out the light pulses. The CdZnTe detector is 1 by 1 by 1 cm and is a semiconductor detector with a better resolution as the Sigma 50. The system is meant to be placed on top of a multicopter UAV to measure radiation coming from a radioactive plume. They tested their system using the Ar-41 plume originating from the BR1 stack.

4.1.2 Methods and Materials

The Zubax GNSS 2.0, the Raspberry Pi 3B+ and the Topaz SiPM multichannel analyser were used in a similar fashion as with the fixed-wing detector system. However, since three separate detectors require a read out, two additional Topaz SiPM multichannel analysers were added. A more detailed explanation of these materials can be found in chapter 3.1.2.4.

4.1.2.1 X8

Due to the proprietary nature of this application, we are not able to disclose detailed specifications on the X8 drone owned by SABCA. However, the following details are publicly available. The X8 Phoenix is a coaxial octocopter drone. Coaxial refers to the two rotors on each of the four arms spinning in opposite directions. The counter rotating of the rotors brings more stability and manoeuvrability. The MTOW is 22.3 kg bringing the maximum payload weight to approximately 6 kg. Empirically we can set the maximum flight time at approximately 15 minutes with a payload of 6 kg. For further information and details we must refer to the drone division of SABCA. Figure 57 shows the X8 with the multicopter payload mounted underneath.

Figure 57: X8 coaxial octocopter owned by SABCA with the multicopter detector system underneath.

4.1.2.2 Multicopter Detector System

The multicopter detector system was made for a multicopter drone with the objective to localize, find and identify radiation sources. The detector system exists out of three identical cylindrical CsI scintillator detectors with SiPMs. Each detector crystal is 7.0 cm in diameter and 7.0 cm in height with an entrance window of 0.5 mm and a housing of 0.8 mm. Figure 58 is the technical drawing of one of the detectors. The three detectors are placed in an equilateral triangle as shown in the schematic in Figure 59. This geometry causes the detectors to shield each other from one side and creates a directional detector system. Similar setups have already been shown to work as can be seen in Chen et al. [70]. The three detectors are calibrated in this configuration and can now be used to define the direction from which radiation is coming.

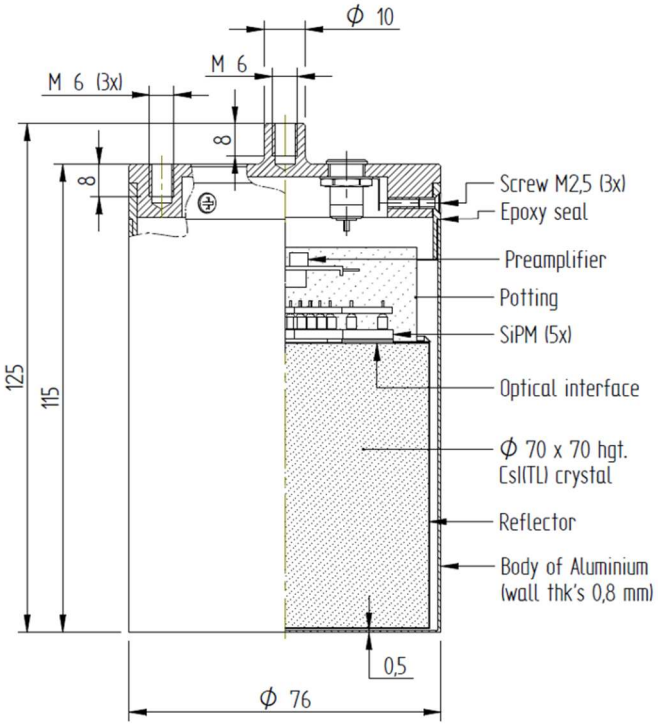

Figure 58: Technical drawing of one of the three identical CsI detectors made by Scionix Holland B.V. (mm when no unit is given).

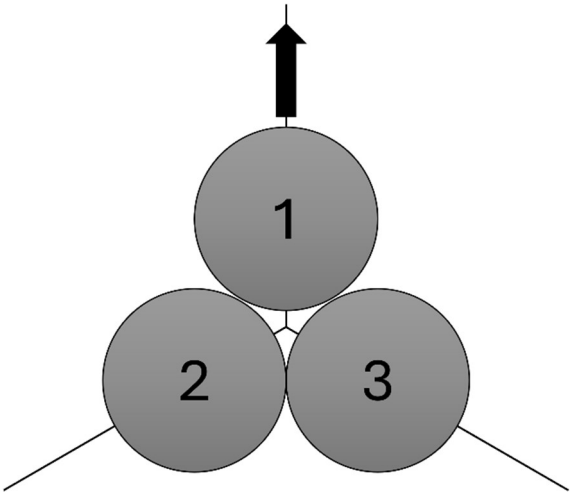

Figure 59: Multicopter detector system configuration placed in an equilateral triangle with detector 1 facing forward and numbering the other detectors counterclockwise with detector 2 on the left and detector 3 on the right as seen from above.

The three CsI detectors each have a separate Topaz SiPM MCA connected to the Raspberry PI 3B+, the settings of each MCA can be seen in Table 11, the different parameters are explained in chapter 1.3. The system also has the Zubax GNSS 2.0 GPS-module. The two key differences between the fixed-wing, section 3.1.2.1, and multicopter system, from a detector system point of view, are the power source and the communication. For the fixed-wing detector system, the drone itself provides 24 V that is converted with a DC-DC converter to 5.1V. The multicopter detector system has a separate power bank to provide the necessary voltage and current. The communication of the fixed-wing detector system goes through the communication channel of the drone and the ground control system. This is not possible for the multicopter. Therefore, SABCA provided a solution using the 4G cellular network and the Botlink XRD2.

Table 11: MCA settings for the three identical detectors in the Multicopter Detector System. The MCA is the Topaz SiPM MCA made by Brightspec.

Detector	1	2	3
Serial number detector	S3AA2825	S3AA2826	S3AA2827
Serial number MCA	13201011	13201013	13201014
Coarse gain	2	2	2
Fine gain	1.100	1.100	1.070
LLD	0	0	0
ULD	1024	1024	1024
Threshold	8	8	8
Rise time	5.60	5.60	5.60
Flat top	2.20	2.20	2.20
Pole-Zeros	2.48	2.48	2.48
BUR enabled	Yes	Yes	Yes
PUR enabled	Yes	Yes	Yes
Digital Gain	32	32	32
LT fine tune	125	125	125
PUR guard	0.12	0.12	0.12
662 keV channel (Cs-137)	244	245	246

The complete detector system is visible in Figure 60 a and b. The schematic in Figure 61 shows the connections and layout. Similar as with the fixed-wing detector system, the script to record, save and send the text file is started on start-up. It can be reset by doing a power cycle. The spectra of the three detectors are saved with their date and time stamp, GPS-coordinates, live time, real time, compass heading, altitude above mean sea level, atmospheric pressure and the complete spectra separated per line and detector in a text file. The size of a text file is approximately 10 kB.

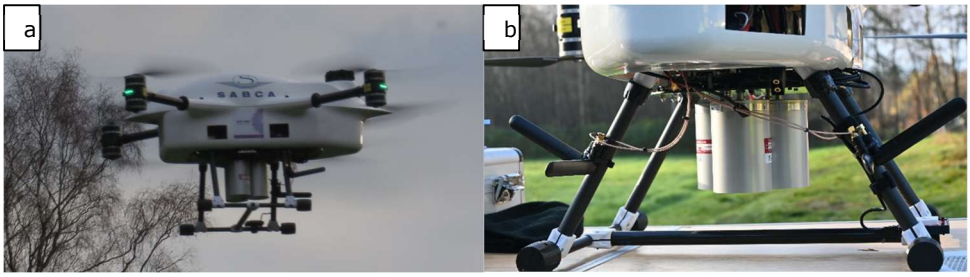

Figure 60: a) (left) The airborne X8 drone with the directional detector system underneath. b) (right) The directional detector system with the Botlink XRD2 antennas fixed onto the carbon legs.

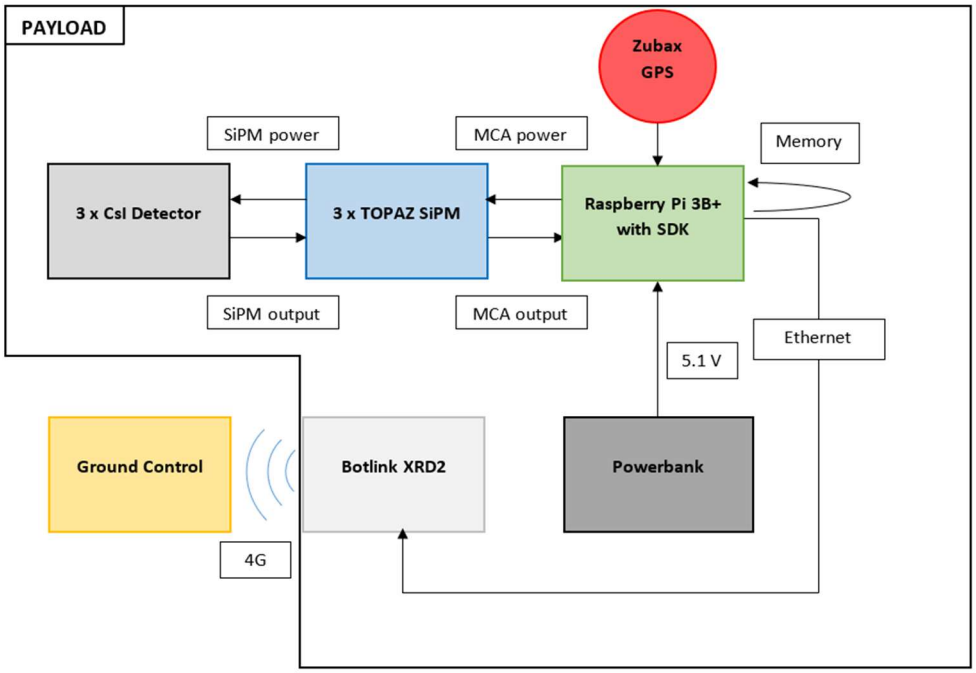

Figure 61: Schematic of the multicopter detector system. It shows the connections and layout of the system.

4.1.2.3 Botlink XRD2

The Botlink XRD2 [118] is a cellular modem that uses one or multiple sim-cards to provide communication and control of a UAV over the cellular network. Since the cellular network has good coverage in Belgium, this system can be used to communicate and control the drone beyond the visual line of sight. The Raspberry PI 3B+ is connected to the Botlink XRD2 through an ethernet connection.

4.1.3 Results and Discussion

4.1.3.1 Angular Dependence

The three identical detectors are placed in a triangular setup to get the angular dependence of the system. A Na-22 point source, with a gamma peak at 1274 keV, was placed at angles with an increment of 5°. The three detectors shield each other depending on the source placement. Similarly, as in Schemm et al. [72], we obtain Figure 62, which we can use as reference for directional measurements. We can see that the counts follow a nearly identical curve for each detector with a shift of approximately 120 degrees. Their maximum and minimum values correspond to the source placement being respectively in front of the detector or shielded by the two other detectors. The small increase between two minima is due to the reduced amount of shielding detector material when the source is placed between the two shielding detectors.

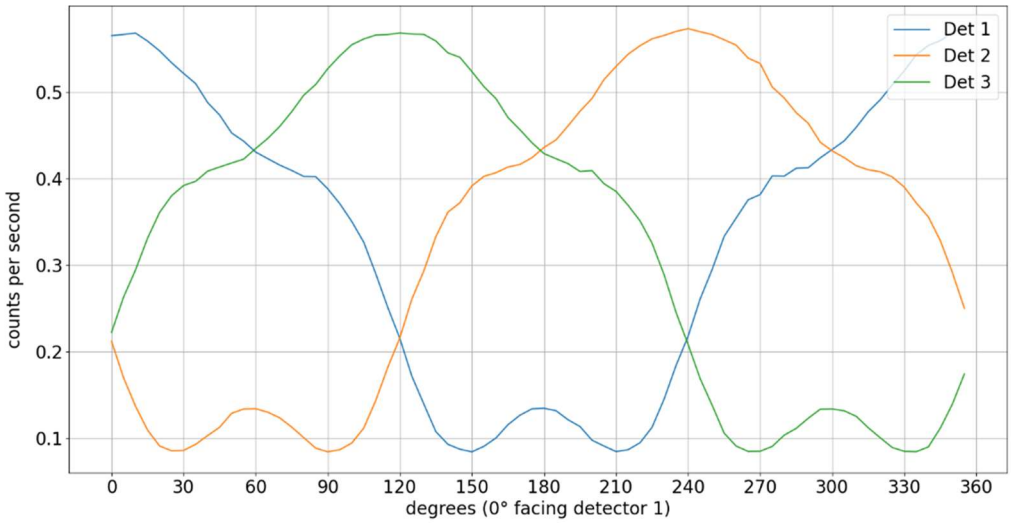

Figure 62: Angular dependence of the three-detector system. The y-axis shows the number of counts per seconds in the 1274 keV peak of Na-22.

4.2 Multicopter Detector System in the Field

4.2.1 Introduction

The multicopter detector system requires extensive in field testing before it can be used in an emergency scenario. Therefore, several scenarios were constructed with point sources and radiological releases from the BR1. There are other experimental systems by different researchers, that are either tested in controlled circumstances like Willis et al. and Schemm et al. [72], [73] or systems that have been tested in-field like the ARDUO system of Chen et al. [70] or the MURS system by Curtis et al. [74].

An alternative for the directional detector systems mounted underneath a UAV, are the portable gamma cameras. As is shown by Mochizuki et al. and Shikaze et al. [88], [119], portable gamma cameras could be used in conjunction with a UAV. However, the required stability and weight do pose an issue for most UAV systems. The gamma camera has to remain stable for long periods of time to acquire enough gamma interactions it needs to pinpoint the origin of the radiation. Mochizuki et al. [119] give an example of how the battery of a UAV is the limiting factor as it can handle flight times of roughly 15 minutes per charged battery pack. The short flight time is mainly due to the 1.9 kg gamma camera the UAV needs to carry. However, in weather that does not allow for stable flights to occur, gamma cameras cannot be used.

Curtis et al. [74] uses six 2x4x16 inch NaI(Tl) detectors that are transported by car. They also incorporated a ^{6}LiF panel to detect neutrons and infra-red cameras for situational awareness. As this system is not used in combination with a UAV

we will not go further in depth on its specifications. However, its concept and the lessons learned from the project were applicable to our system.

Chen et al. [70] uses eight CsI(Tl) scintillation detectors for their system by placing them in a 2 by 2 by 2 matrix. This makes the directional resolution better as our system, as it is easier to differentiate between the four detectors as it is with the three detectors we use. However, the amount of detector material is only 0.35L, which is less than half of our detector system which is 0.8 L. The increase in detector material should result in a higher count rate which makes calculating the direction more accurate. The ARDUO system is further advanced than the current directional system we explain in this chapter, but this work is the first step in creating a similar or even improved directional detector system for UAVs.

4.2.2 Methods and Materials

The sources used in these test scenarios were a Cs-137 point source and the Ar-41 plume originating from the BR1 stack. As flightpath parallel lines were used with varying widths depending on the scenario. Detailed information on the detector system can be found in chapter 4.1.2.2.

4.2.2.1 BR1

On March 30th 2022 a stationary measurement was done downwind from the BR1 stack. The multicopter detector system was placed on a tripod at 400 m distance from the stack with the detectors pointing upwards. The LIDAR (Laser Imaging Detection And Ranging) was used to measure the wind speed and direction at 69 m above ground level which is close to the height of the BR1 stack, 70 m. The detector system was positioned with the front towards the south as is shown by the arrow in Figure 63. The LIDAR, from the brand windcube, is a device that uses the reflection of a laser to calculate the speed and direction of the wind at multiple altitudes. The positional situation with the BR1 and the detector location is shown in Figure 63.

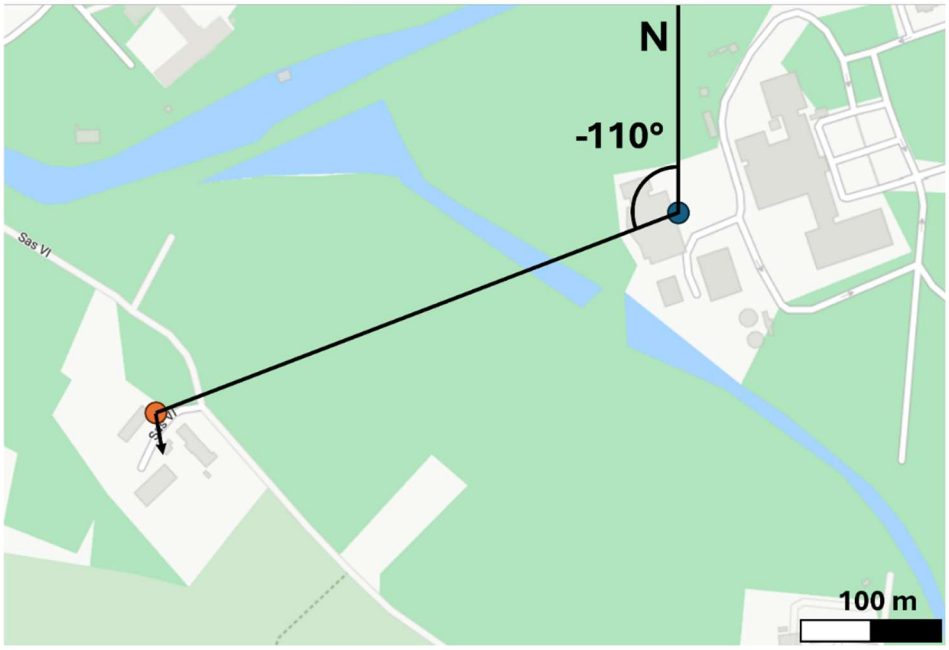

Figure 63: Map of the area around the BR1 stack, blue dot. The location of the detector system is represented by the orange dot. The arrow at the orange dot represents the orientation of the detector system.

4.2.2.2 Cs-137 Point Source

A first live test, using a drone, was done at the SCK CEN farm. We used a Cs-137 source positioned on the roof of one of the storage buildings at a height of approximately 2 m, the source is visible in Figure 64. The lines were flown at multiple altitudes starting from 1 m height with a flight speed of 1 m/s and a detector measurement time of 1 second. During the flight, the compass direction of the drone remained the same.

Figure 64: Cs-137 source placed on the roof of a storage building located at the SCK CEN farm. The height was approximately 2 m.

4.2.2.3 Directional Algorithm

With the output from the three detectors, shown in Figure 62, we are able to easily distinguish six separate directions, three where only one detector is at its maximum and another three where two of the detectors have a similar count rate. However, to achieve a more exact directional algorithm we can combine the three detector values at their relative locations. When the counts are assigned to the z-axis and the detector-locations are placed on the xy-plane, it is possible to create a plane from the three points of the detector system. A vector that is perpendicular to the created plane can then be used to derive the direction of the incoming radiation. As there are two possible perpendicular vectors it is important to choose the vector that is pointing to the negative side of the z-axis. The projection of the vector to the xy-plane gives the direction and an indication of the intensity of the radiation measured by the detector system. Figure 65 and the equations underneath show how this would work. A point of attention has to be made to the angle we retrieve from this process. The angle from a mathematical point of view is taken relative to the positive x-axis. The detectors are positioned so that detector 1 is facing the GPS's north and in the 3D representation it is placed on the y-axis. Therefore, we have to add 90 degrees to account for the mathematical definition of the angle.

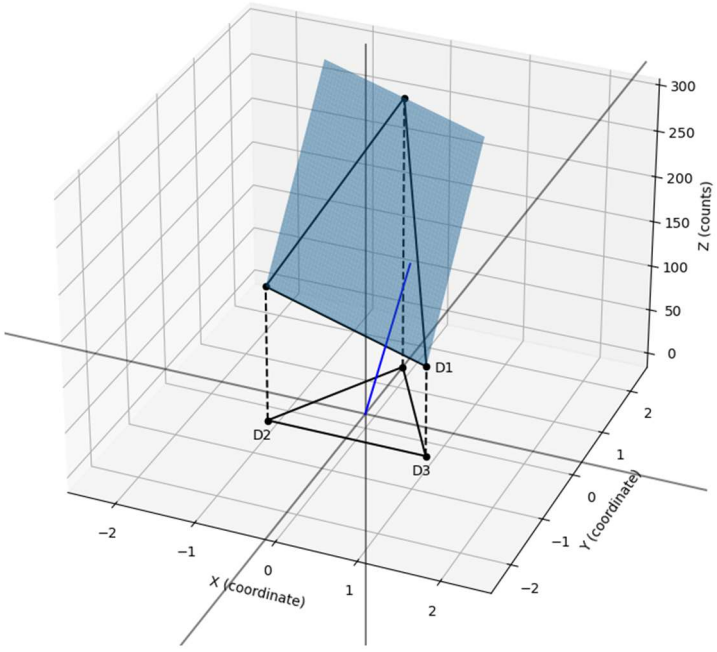

Figure 65: 3D plot of the directional algorithm. The dark blue line represents the projection of the normal vector on the xy-plane. The three detectors D1, D2 and D3 are placed on the xy-plane. The dashed lines represent their respective number of counts (300,150,100).

$$P_1(x_1, y_1, z_1) \quad P_2(x_2, y_2, z_2) \quad P_3(x_3, y_3, z_3) \qquad (12)$$

$$\vec{v} = \langle x_1 - x_2, y_1 - y_2, z_1 - z_2 \rangle \quad \vec{w} = \langle x_1 - x_3, y_1 - y_3, z_1 - z_3 \rangle \qquad (13)$$

$$\vec{n} = \vec{v} \times \vec{w} \qquad (14)$$

$$\vec{n} = (v_y w_z - v_z w_y)\vec{\imath} + (v_z w_x - v_x w_z)\vec{\jmath} + (v_x w_y - v_y w_x)\vec{k} \qquad (15)$$

$$\vec{n} = a\vec{\imath} + b\vec{\jmath} + c\vec{k} \qquad (16)$$

$$R = \sqrt{a^2 + b^2} \quad \theta = \tan^{-1}\left(\frac{b}{a}\right) \qquad (17 \text{ and } 18)$$

In Equation 12, the three points $P1$, $P2$ and $P3$ represent the position (x,y) and the number of counts (z) for each detector. From these 3 points, two vectors v and w can be created as is shown in Equation 13. The cross product, Equation 14 and 15, gives us the normal vector n, perpendicular to the plane in which v and w lie. The normal vector n, Equation 16, can then be used to calculate the angle θ and the length R from its projection to the xy-plane, Equations 17 and 18.

4.2.3 Results

4.2.3.1 Ar-41 release from the BR1

The results in Figure 66 show the wind vector in degrees in the upper graph and the total counts in the Ar-41 gamma energy range (1294 keV) every 60 seconds for each individual detector in the lower graph. The counts are shown in a logarithmic scale to show the difference between each detector more clearly. With the wind, we can now also verify whether the detector response aligns with the shielding that should reduce the counts in one detector. The black line in the wind vector graph represents the angle, -110°, between the detector position relative to the north with the BR1 stack as centre point. A visualisation of the angle is also visible in Figure 63.

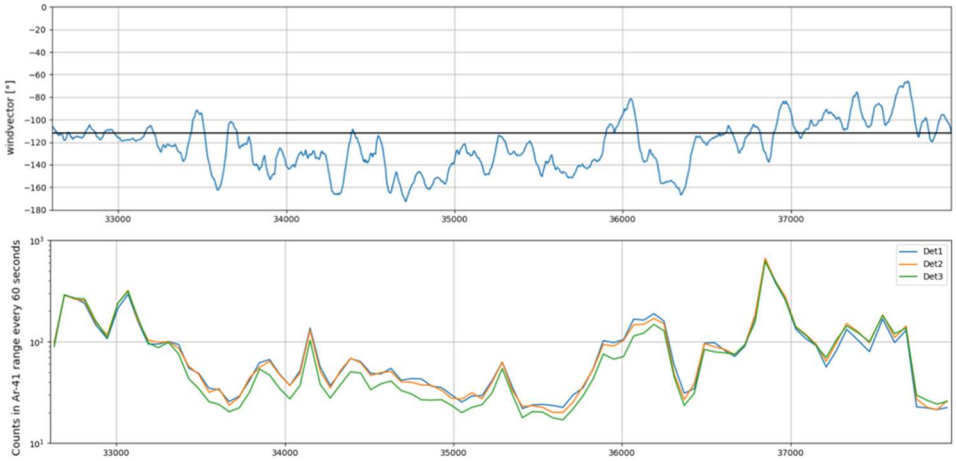

Figure 66: The two graphs show the wind vector in degrees and the counts per 60 seconds in the Ar-41 energy range (1294 keV) for each detector. The black line in the wind vector graph represents the angle between the North and the line between the BR1 stack and the position of the detector system.

4.2.3.2 Point Source Localisation

Figure 67 shows the total number of counts per second for each individual detector. When the different detector responses are compared, we can see a pattern in the delay of response for each detector. The two lower peak responses are shifted which we can use as a directional differentiator together with the difference in peak height due to shielding. The source was placed at roughly 2 m in height and the UAV's height was increasing with 1 m with each passing ranging from 1 to 6 m. The drone kept the same orientation during the measurements. The directional algorithm mentioned in chapter 4.2.2.3 allows the creation of Figure 68. Here the arrows represent the direction from which the radiation is coming according to the algorithm. The length of the arrows are a representation of the strength of the directionality of the measured radiation.

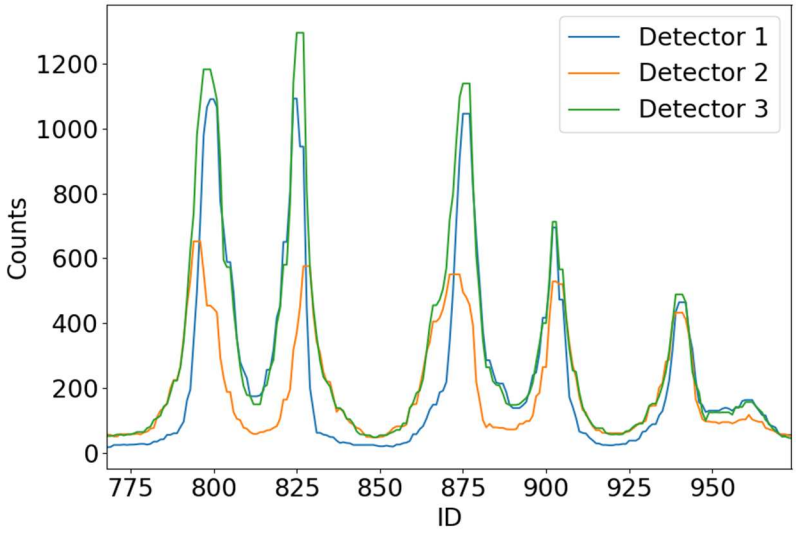

Figure 67: The detector systems response in counts per second from a Cs-137 point source located at roughly 2 m. The flight speed was approximately 1 m/s and the height ranged from roughly 1 to 6 m.

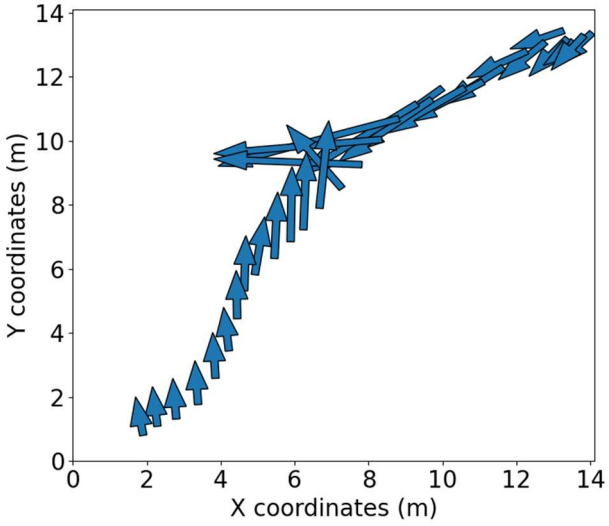

Figure 68: Map created by the directional algorithm. The flight speed was 1 m/s and the height was approximately 3 m.

4.2.4 Discussion

The Ar-41 release of the BR1, was visible in the spectra of the directional detector, and could even distinguish the side the plume was on relative to the detector system. Figure 66 shows how the detector reacts to the plume and how the

response of the three detectors changes as the plume changes direction. The centre and right side of the bottom graph clearly show a lower count rate for detector 3 (green) and detector 1 (blue). This corresponds well with the wind direction shown on the top graph. Measuring with a shorter live time would introduce too much noise in the spectra, rendering the results unreliable. Longer live times might solve the low statistics but will reduce the accuracy of the directionality of the system as it will integrate over a larger time.

In Figure 67 the count rate in the Cs-137 region of interest is plotted in function of the time. The UAV with the directional detector system mounted underneath, passed several times next to the Cs-137 source at increasing altitudes ranging from 1 to 6 m. The increase in distance to the source is also visible in the peak height. Figure 67 shows how the different detectors react to the source. Detector 2 (orange) was furthest away from the source and was shielded by the two other detectors.

Figure 68 gives a view of the output from the directional algorithm. Like the ARDUO system of Chen et al. [70], the arrows represent a measured spectrum on each of the three detectors. The direction in which the arrow points is retrieved from the algorithm described in chapter 4.2.2.3. A longer arrow represents a larger difference between the detectors meaning that the source is closer. Some of the arrows seem to have a slight derivation in direction compared to the others. There are two reasons for this error. Firstly, the GPS coordinates retrieved from the Zubax GNSS 2.0 can have an error, which causes a translation of the arrow causing it to point to a slightly different point. Secondly, the Zubax GNSS 2.0 was not demagnetized at the moment of the measurement. Therefore, it is possible the compass heading of the GPS-module was giving slight deviations causing the angle of the arrow to be slightly off target.

4.3 Conclusions on Objective 3

Objective 3 was split into two sub-objectives, 3a and 3b. 3a was finding and creating a directional detector that does not use shielding or collimators. The directional detector system that was developed does not use a collimator and the shielded gamma rays are still recorded in the three detector configuration. Chapter 4.1 shows how the detector system works in a controlled environment. However, the directionality of the directional detector system in a practical scenario is significantly more complex than the controlled laboratory measurements. With a UAV, the measurements could follow the plume itself, making it act as a mobile measurement station which is of great interest in emergency situations.

The movement of the complete detector system makes the shielding of the individual detectors less straightforward. The integration of the signals over the detector movement is an important factor, hence we advise to reduce the flight speed during the flight as this might increase the clarity in the directional response of the detector system. To have a robust way of retrieving the directional response of the detector, a directional algorithm was developed, originating out of sub-

objective 3b. The directional algorithm proved to be an important tool in source localization. The measurements at elevated heights provided adequate positioning. Future research might improve the stability of the system and look into multiple point sources and surface or ground contaminations. These source geometries are more challenging and it will be interesting how the directional algorithm handles these sources. A key parameter in the directional algorithm is the compass heading of the GPS module. Flying close to buildings or metal structures will influence the registered heading. Therefore, we advise to maintain the same heading over the entire flight or use GPS modules that are less prone to these interferences. The first option was used in this test to specifically test the directional algorithm and to avoid interference.

5 Conclusion

The target of this thesis was to improve radiological monitoring using drones. We have attempted to do this through three main research questions and their respective objectives.

5.1 Short Conclusion

- The standard 6150AD-b dose rate detector can be used as a payload for a UAV.
    - Bluetooth or a different form of communication should be available.
    - The streaking effect due to the time constant should be kept as low as possible by decreasing the flight speed and altitude.
- Most spectroscopy detector outputs can be converted to dose rate by means of stripping and thus be used together with a UAV to perform aerial dose rate measurements.
    - A good calibration of the weighing factors is mandatory.
    - The recorded spectra can also be used to identify the radionuclides being measured.
- The optimal detector geometry and material for a 1 kg detector for UAV measurements is a cylindrical CsI(Na) scintillator with a height of 3 cm and a radius of 5 cm.
    - This is the optimum from the materials and geometries researched in this thesis simulated with the Monte Carlo code Penelope.
    - The final detector geometry for the fixed-wing detector system was changed to 3.5 cm height and 5.5 cm radius.
- Two successful measurement campaigns were conducted using the fixed-wing detector system in combination with the Penguin C fixed-wing.
    - The first measurement campaign tested the ability of the system to measure K-40 ground concentrations over the fields surrounding Droneport Sint-Truiden.
    - The second measurement campaign was done over the SCK CEN and its surroundings. The complex and varying sources (Ar-41 plume from the BR1 stack, the Solarium and Belgoprocess) are a great data set for further analysis and research.
- A directional detector system was developed with three identical CsI(Na) scintillator detectors positioned in an equilateral triangle. The three detectors shield each other allowing the system to obtain directional data from the measurements.
    - The detectors are 7 cm in diameter and 7 cm in height.
    - The system is closely related to the direction of the drone, which adds difficulty in creating an algorithm for determining the direction of the incoming radiation.

- A robust directional algorithm was created based on the count rate of each individual detector and the projection of the plane created by the three count rates.
    - The algorithm incorporates the direction of the drone by using the detector systems own compass heading obtained from the GPS.

5.2 Main Conclusion

1. **How to assess the dose rate distribution of an environment in case of a nuclear or radiological scenario at a safe distance using UAVs to assist first responders in delineating unsafe areas?**
    - **What type of dose rate should be evaluated?**
    - **Which types of detector systems can be used for assessing the dose rate distribution?**
    - **What are the advantages and disadvantages of each detector system?**

In chapter 2 we have found at least two systems that can help first responders in case of radiological and nuclear scenarios. The first one, mounting a reference dose rate detector underneath a multicopter drone, has proven its use for cases in delineating dose rate zones around a point source. However, the streaking effect caused by the time constant does cause deformation of the contours at high speeds, so this should be kept in mind. The type of dose rate can vary depending on the detector, so it is adamant that not only the units but also the definition and name of the dose rate is mentioned when reviewing the results.

The second system, a relatively small scintillator detector, proved to be an equally useful tool. The dose rate readings using the stripping method are quite cumbersome with the monoenergetic sources and the reduced sensitivity due to the size of the detector is not ideal. However, the system allows for both identification and dose rate monitoring which are both important tasks in emergency scenarios. Additionally, the stripping method can be used to convert the measured spectra in any dose rate definition that is required for the emergency at hand.

2. **How can we achieve identification and quantification of radioactive sources in case of a nuclear or radiological event using a UAV?**
    - **What would be a good drone-detector combination for these purposes?**
    - **How can we optimize the detection system?**
    - **What considerations or methods should be followed when interpreting the results of measurements done with such a system?**
    - **How can we demonstrate such systems in non-emergency situations?**

In chapter 2.2 we already mentioned the use of a scintillator detector to identify the radiological sources using spectroscopy. However, the size of the detector and the material also play an important part in this task. The efficiency of detecting the gamma rays originating from the radiological sources is strongly dependent on the volume, density, geometry and detector characteristics of the detector. To optimize and choose a detector material and geometry we performed several Monte Carlo simulations using the Monte Carlo code Penelope with efficiency and limited weight being our main requirements. The results showed CsI as optimal detector material for our requirements. The selection of the optimal detector material and geometry will differ depending on the requirements (e.g. resolution, price).

Nuclear or radiological events are very rare but if they happen, it is on a relatively larger scale (e.g. Fukushima, Chernobyl). To identify and quantify larger areas we would require a UAV that can fly over several kilometres without requiring much assistance. This does eliminate commercial multicopter detectors as possible candidates, as they are known for their shorter flight times and limited action radius. Multicopter detectors can still be used in these situations but the region under investigation should be limited. Either fixed-wing UAVs or unmanned helicopters are best equipped for these types of flights. We opted for a fixed-wing UAV, since it has a significantly longer flight time and can fly over significantly larger distances. Unmanned helicopters would certainly be beneficial for certain scenarios, as they can hoover over a single point and are more agile.

As we demonstrated with the fixed-wing detector system, we are able to quantify concentrations on ground level and even detect and follow radiological plumes. These demonstrations are an important step in verifying the capabilities of the system as a whole. Therefore, we advise any other researchers to find similar locations where there are routine releases of radiological material, fields with a historic contamination or regions with naturally occurring radiologic material. Those sites allow their detector systems to be calibrated and verified. In most cases their concentrations or activities are well known and easily comparable with experimental results. However, in case of UAV flights over nuclear sites it is

advised to consult with groups and companies that have experience in such flights as they require significant planning, documentation and approvals from government instances.

3. **How can we achieve robust directional measurements using a UAV keeping high sensitivity for typical gamma ray energies?**
    - **What detector configuration can be used to achieve directional measurements while remaining within the limitations of the UAV?**
    - **What considerations, procedures and methods should be followed when interpreting the results of measurements done with such a system?**

The creation of a directional detector system to be mounted underneath a drone gave us several options regarding shielding and geometry. Because the drone has a maximum take-off weight, collimators might pose an issue. Therefore, we chose three identical detectors placed in an equilateral triangle. This geometry shields one detector but does not use any payload weight for collimation. The shielding material is detector material and allows us to have additional directionality due to its symmetry.

However, the multicopter system also added a layer of complexity. The system's relative angle became a significant parameter and will require a more robust GPS system to work well in industrial environments. These environments often have bad GPS coverage because of the amount of steel and concrete.

An important step for interpreting the results from a directional detector, is the calibration. Without adequate knowledge of detector responses in known environments and configurations it is impossible to retrieve any meaningful information regarding directionality. Further, does there have to be a known relation between the detector system's direction and the UAV's direction. Additionally, a good system for representing the recorded data is mandatory. The use of multiple detectors creates significantly more data that has to be represented in an understandable and comparable manner. How this is done is strongly dependent on the number of detectors and their geometry.

5.3 Lessons Learned

This thesis provided two finished detector prototypes, the fixed-wing detector system and the multicopter directional detector system. The creation of these two systems taught us several important lessons in remote detector system design.

A first lesson came with the use of a raspberry pi in our detector system. An issue that was discovered was the interference between the GPS of the fixed-wing UAV and the USB 3.0 chipset of the raspberry pi 4. Therefore, it is advisable to avoid using the USB 3.0 chipset from the raspberry pi 4 by downgrading to the raspberry pi 3 A, B or B+. However, the interference between the chipset and the on-board

GPS might not be present on all UAV systems or there might be other points of interference that cause fault modes on the UAV. Therefore, it is recommended to perform thorough testing on the ground to catch these types of interference before take-off.

A second lesson to take into consideration in future detector systems is to create a stand-alone system. This means that the system should be operationally independent from the UAV. Properties such as power supply and communication should not depend on the UAV such that the system can work autonomously with any UAV, UGV or crewed vehicle available. For communication it is important that there is a wide and stable coverage, for example the 4G cellular network or long-range radio waves. An added value to a self-sustaining system is the ability to change which UAV to use depending on the situation and safety concerns. This would simplify the regulatory certification process as the detector can be considered as a standalone payload.

A third lesson is the use of a remote reset. A remote reset allows the system to restart in flight without operator intervention. Both developed systems in this thesis have this feature. The reset happens by executing a power cycle by the drone pilot. The systems restart automatically when receiving power making the remote reset possible. The downside of this feature is that it is dependent on the connection with the UAV, making it less self-reliant. However, the benefit of a remote reset is invaluable for the fixed-wing system as landings with the aim to relaunch are very time consuming: once landed, a next launch is postponed with several hours due to the repacking of the parachute and airbag, safety checks and possibly repositioning of the catapult due to changes in wind direction. For the multicopter system a short pause causes no issue as it can be done while switching the battery packs.

UAVs remain an innovative tool as aid in performing radiological measurements and this thesis has attempted to improve some of the challenges that come with using UAVs for radiological monitoring.

6 Outlook

A first subject for future research is the use of an alpha or beta detector, PIPS (Passivated Implanted Planar Silicon) detectors for example. Since alpha and beta radiation have a limited reach in air of a few centimetres and a few meters respectively, the evaluation of the extent of a contamination or plume would become significantly simpler as was the case with gamma radiation. The possible range from which the radiation is coming is significantly smaller. However, the air displacement by the drone might cause difficulties with the interpretation of these measurements and should be investigated thoroughly. Additionally, there is also the risk of possible contamination of the UAV and the detector system.

Incorporation of deconvolution algorithms should also be a target for further research. Deconvolution could improve the spatial resolution of the UAV measurements. This would be especially helpful when flying over larger areas with the fixed-wing detector system as the spatial resolution is also dependent on the flight speed which is significantly higher for fixed-wing UAVs compared to multicopter UAVs. Additionally, this can also work for dose rate to distinguish multiple sources or hotspots. Besides deconvolution, future research should also try to incorporate other algorithms to further improve the system. Examples of these algorithms are the Maximum-Likelihood, Expectation–Maximization or NASVD (Noise Adjusted Singular Value Decomposition).

Future detector systems should aim on being self-sustaining so they can be used with any UAV without being dependent on the UAV's power supply or communication channels. Doing so, will make the detector system more flexible and allow it to work with different UAVs, UGVs or even crewed vehicles. However, in certain cases it might be advantageous to incorporate the detector system inside the drone to reduce weight, interference or even protection against contamination.

Aside from the payload, UAVs can be improved too, especially in the regulatory and safety framework. Obtaining a SORA permit for flights over critical infrastructures was a great challenge, which would not have been accomplished without the skill and experience from the people at SABCA. Therefore, future projects should not just aim to improve the scientific value of their flight but also improve the technical features that raise the safety of the UAV. Technologies such as obstacle recognition and avoidance will be needed to switch UAVs in radiological monitoring from research prototypes to standardized tools.

Improving the automatic data processing and integration with the monitoring network is a future goal that could be attempted. However, integration with the monitoring network should be done with care. The data obtained from the detector system mounted under a UAV is heavily dependent on the flight parameters while the monitoring network is stationary and more stable.

The data from the fixed-wing detector when flying over the SCK CEN site should be investigated further. The concentration of the plume could be calculated in a

similar way as was done for the K-40 concentration over Droneport. However, adaptation should be made to account for the source distribution in air instead of in the ground. Additionally radiological plume modelling is required to check the variation in width and height as the plume travels further from the stack, this will be used to estimate the source distribution which thereafter can be used to estimate the concentration. These adaptations would be an interesting subject for further research and analysis.

It is interesting to develop the directional multicopter system further to eventually let the UAV fly autonomously for source or hotspot localisation. This would mean that the UAV would be piloted by the directional detector system to localise the source. However, this causes several issues regarding safety and responsibility in case of a crash or collision. Therefore, the system should incorporate additional safety features such as obstacle recognition and avoidance and a differential GPS for a better positional awareness.

7 Bibliography

[1] DJI, “DJI Agriculture.” Accessed: Dec. 20, 2025. [Online]. Available: https://ag.dji.com/

[2] P. Radoglou-Grammatikis, P. Sarigiannidis, T. Lagkas, and I. Moscholios, “A compilation of UAV applications for precision agriculture,” *Computer Networks*, vol. 172, May 2020, doi: 10.1016/j.comnet.2020.107148.

[3] T. Ward, “F-1 Filming Drone.” Accessed: Dec. 20, 2025. [Online]. Available: https://www.redbull.com/int-en/worlds-fastest-filming-drone-build

[4] K. Lu, R. Xu, J. Li, Y. Lv, H. Lin, and Y. Liu, “A Vision-Based Detection and Spatial Localization Scheme for Forest Fire Inspection from UAV,” *Forests*, vol. 13, no. 3, Mar. 2022, doi: 10.3390/f13030383.

[5] DJI, “DJI Infastructure.” Accessed: Dec. 20, 2025. [Online]. Available: https://enterprise.dji.com/inspection

[6] Amazone, “Amazone Drone Delivery.” Accessed: Dec. 20, 2025. [Online]. Available: https://www.amazon.com/gp/help/customer/display.html?nodeId=T3jxhuvPfQ629BOIL4

[7] Helicus BVBA, “Helicus.” Accessed: Dec. 20, 2025. [Online]. Available: https://helicus.com/

[8] FANC, “FANC, SCK CEN en defensie voeren testvlucht uit met helikopter boven kerncentrale Tihange.” Accessed: May 01, 2025. [Online]. Available: https://fanc.fgov.be/nl/nieuws/fanc-sck-cen-en-defensie-voeren-testvlucht-uit-met-helikopter-boven-kerncentrale-tihange

[9] J. Aleotti *et al.*, *Unmanned Aerial Vehicle Equipped with Spectroscopic CdZnTe Detector for Detection and Identification of Radiological and Nuclear Material*. IEEE, 2015.

[10] C. Lee and H. R. Kim, “Optimizing UAV-based radiation sensor systems for aerial surveys,” *J. Environ. Radioact.*, vol. 204, pp. 76–85, Aug. 2019, doi: 10.1016/j.jenvrad.2019.04.002.

[11] D. Connor, P. G. Martin, and T. B. Scott, “Airborne radiation mapping: overview and application of current and future aerial systems,” *Int. J. Remote Sens.*, vol. 37, no. 24, pp. 5953–5987, Dec. 2016, doi: 10.1080/01431161.2016.1252474.

[12] C. F. Liew, D. DeLatte, N. Takeishi, and T. Yairi, “Recent Developments in Aerial Robotics: A Survey and Prototypes Overview,” Nov. 2017, [Online]. Available: http://arxiv.org/abs/1711.10085

[13] IAEA, “Technical Reports Series 323: Airborne Gamma Ray Spectrometer Surveying,” Vienna, 1991.

[14] Y. Sanada and T. Torii, “Aerial radiation monitoring around the Fukushima Dai-ichi nuclear power plant using an unmanned helicopter,” *J. Environ. Radioact.*, vol. 139, pp. 294–299, Jan. 2015, doi: 10.1016/j.jenvrad.2014.06.027.

[15] S. van der Veeke, J. Limburg, R. L. Koomans, M. Söderström, and E. R. van der Graaf, “Optimizing gamma-ray spectrometers for UAV-borne surveys with geophysical applications,” *J. Environ. Radioact.*, vol. 237, Oct. 2021, doi: 10.1016/j.jenvrad.2021.106717.

[16] S. van der Veeke, J. Limburg, R. L. Koomans, M. Söderström, S. N. de Waal, and E. R. van der Graaf, "Footprint and height corrections for UAV-borne gamma-ray spectrometry studies," *J. Environ. Radioact.*, vol. 231, May 2021, doi: 10.1016/j.jenvrad.2021.106545.

[17] D. T. Connor *et al.*, "Corrigendum: Radiological Mapping of Post-Disaster Nuclear Environments Using Fixed-Wing Unmanned Aerial Systems: A Study From Chornobyl (Frontiers in Robotics and AI, (2020), 6, (149), 10.3389/frobt.2019.00149)," Feb. 28, 2020, *Frontiers Media S.A.* doi: 10.3389/frobt.2020.00030.

[18] D. T. Connor *et al.*, "Radiological Mapping of Post-Disaster Nuclear Environments Using Fixed-Wing Unmanned Aerial Systems: A Study From Chornobyl," *Front. Robot. AI*, vol. 6, Jan. 2020, doi: 10.3389/frobt.2019.00149.

[19] Federale Overheidsdienst Mobiliteit en Vervoer, "drone legislation mobilit.belgium.be," https://mobilit.belgium.be/nl/luchtvaart/vliegen-met/drones-uas/stappenplan/veelgestelde-vragen#:~:text=Vanaf%2031%20december%202020%20wordt,Noorwegen%2C%20Verenigd%20Koninkrijk%20en%20Zwitserland. Accessed: Apr. 21, 2025. [Online]. Available: https://mobilit.belgium.be/nl/luchtvaart/vliegen-met/drones-uas/stappenplan/veelgestelde-vragen#:~:text=Vanaf%2031%20december%202020%20wordt,Noorwegen%2C%20Verenigd%20Koninkrijk%20en%20Zwitserland.

[20] Drone Class, "dronelicense.eu," https://www.dronelicense.eu/blogs/popular/drone-rules-in-2024. Accessed: Apr. 21, 2025. [Online]. Available: https://www.dronelicense.eu/blogs/popular/drone-rules-in-2024

[21] Skeyes, "Skeyes Droneguide Viewer." Accessed: Jan. 13, 2025. [Online]. Available: https://map.droneguide.be/

[22] G. R. Gilmore, *Practical Gamma-ray Spectrometry*, 2nd ed. Wiley, 2008.

[23] S. Naeem Ahmed, *Physics and Engineering of Radiation Detection*, 2nd ed. Elsevier, 2015.

[24] J. E. Martin, *Physics for Radiation Protection*, 3rd ed. Weinheim: Wiley-VCH, 2013.

[25] J. H. Hubbell and S. M. Seltzer, "NIST x-ray mass attenuation coefficients database." Accessed: Mar. 28, 2024. [Online]. Available: https://www.nist.gov/pml/x-ray-mass-attenuation-coefficients

[26] F. A. Attix, "Charged-Particle and Radiation Equilibria."

[27] N. Petoussi-Henss *et al.*, "Annals of the ICRP 116: Conversion Coefficients for Radiological Protection Quantities for External Radiation Exposures," SAGE Publications Ltd, 2010. doi: 10.1016/j.icrp.2011.10.001.

[28] D. Beninson *et al.*, *Annals of the ICRP 74: Conversion Coefficients for use in Radiological Protection against External Radiation*, 1st ed., vol. 26. Pergamon, 1996.

[29] A. Endo, "Operational quantities and new approach by ICRU," Tokai-mura, 2015.

[30] "SCINTILLATOR PROBE 6150AD-b (/H, /E) Plastic Scintillator Probe for the Dose Rate Meter 6150AD ® for measuring photon radiation (gamma and X-radiation)." [Online]. Available: www.automess.de

[31] "Operating Manual for the Dose Rate Meter 6150AD," Mar. 2004. [Online]. Available: http://www.automess.de

[32] "6150AD Universal Radiation Meter for Measuring Photon Radiation (Gamma and X-radiation), and for Detecting Alpha and Beta Radiation if Operated with External Probes."

[33] R. L. Grasty, B. R. B. Walters, J. Hovgaard, and J. R. Lamarre, "CALIBRATION OF A 7.6 CM 7.6 CM (3 INCH 3 INCH) SODIUM IODIDE GAMMA RAY SPECTROMETER FOR AIR KERMA RATE," *Radiat. Prot. Dosimetry*, vol. 94, no. 4, pp. 309–316, 2001, [Online]. Available: http://rpd.oxfordjournals.org/

[34] A. Camp and A. Vargas, "Ambient dose estimation h *(10) from laBr3(Ce) spectra," *Radiat. Prot. Dosimetry*, vol. 160, no. 4, 2014, doi: 10.1093/rpd/nct342.

[35] S. Tsuda and K. Saito, "Spectrum–dose conversion operator of NaI(Tl) and CsI(Tl) scintillation detectors for air dose rate measurement in contaminated environments," *J. Environ. Radioact.*, vol. 166, Jan. 2017, doi: 10.1016/j.jenvrad.2016.02.008.

[36] H. Dombrowski, "Area dose rate values derived from NaI or LaBr3 spectra," *Radiat. Prot. Dosimetry*, vol. 160, no. 4, pp. 269–276, 2014, doi: 10.1093/rpd/nct349.

[37] R. Casanovas, E. Prieto, and M. Salvadó, "Calculation of the ambient dose equivalent H*(10) from gamma-ray spectra obtained with scintillation detectors," *Applied Radiation and Isotopes*, vol. 118, pp. 154–159, Dec. 2016, doi: 10.1016/j.apradiso.2016.09.001.

[38] A. Dr. Richardt, B. Dr. Hülseweh, B. Prof. Dr. Ing. Niemeyer, and F. Dr. Ing. Sabath, Eds., *CBRN Protection: Managing the Threat of Chemical, Biological, Radioactive and Nuclear Weapons*, 1st ed. Wiley, 2013. doi: 10.1002/9783527650163.

[39] C. Rojas-Palma *et al.*, "Triage, Monitoring and Treatment of people exposed to ionising radiation following a malevolent act," 2009. [Online]. Available: www.tmthandbook.org

[40] IAEA, "The Fukushima Daiichi Accident : report by the Director General," International Atomic Energy Agency, Vienna, 2015.

[41] FOD Mobiliteit en Vervoer, "Federale Overheid Mobiliteit en Vervoer." Accessed: Oct. 26, 2025. [Online]. Available: https://mobilit.belgium.be/nl/luchtvaart/luchtruim/aanvragen

[42] Federaal Overheidsdienst Mobiliteit en Vervoer, "Luchtvaartveiligheidsinformatiefolder (ASIL): besturen van een drone," 2017.

[43] V. Šmídl and R. Hofman, "Tracking of atmospheric release of pollution using unmanned aerial vehicles," *Atmos. Environ.*, vol. 67, pp. 425–436, Mar. 2013, doi: 10.1016/j.atmosenv.2012.10.054.

[44] D. T. Connor *et al.*, “Radiological comparison of a FDNPP waste storage site during and after construction,” *Environmental Pollution*, vol. 243, pp. 582–590, Dec. 2018, doi: 10.1016/j.envpol.2018.08.099.

[45] D. T. Connor *et al.*, “Application of airborne photogrammetry for the visualisation and assessment of contamination migration arising from a Fukushima waste storage facility,” *Environmental Pollution*, vol. 234, pp. 610–619, Mar. 2018, doi: 10.1016/j.envpol.2017.10.098.

[46] P. G. Martin, O. D. Payton, J. S. Fardoulis, D. A. Richards, Y. Yamashiki, and T. B. Scott, “Low altitude unmanned aerial vehicle for characterising remediation effectiveness following the FDNPP accident,” *J. Environ. Radioact.*, vol. 151, pp. 58–63, Jan. 2016, doi: 10.1016/j.jenvrad.2015.09.007.

[47] A. J. Cresswell, H. Kato, Y. Onda, and K. Nanba, “Evaluation of forest decontamination using radiometric measurements,” *J. Environ. Radioact.*, vol. 164, pp. 133–144, Nov. 2016, doi: 10.1016/j.jenvrad.2016.07.024.

[48] E. Buchanan, A. J. Cresswell, B. Seitz, and D. C. W. Sanderson, “Operator related attenuation effects in radiometric surveys,” *Radiat. Meas.*, vol. 86, pp. 24–31, Mar. 2016, doi: 10.1016/j.radmeas.2015.12.029.

[49] P. G. Martin *et al.*, “Validation of a novel radiation mapping platform for the reduction of operator-induced shielding effects,” *Journal of Radiological Protection*, vol. 38, no. 3, Sep. 2018, doi: 10.1088/1361-6498/aad5f2.

[50] W. Khan, C. He, Y. Cao, R. Khan, and W. Yang, “A detector system for searching lost γ-ray source,” *Nuclear Engineering and Technology*, vol. 52, no. 7, pp. 1524–1531, Jul. 2020, doi: 10.1016/j.net.2019.12.021.

[51] G. Olyslaegers, J. Paridaens, S. Geelen, K. Vandersteen, and J. Camps, “Celmes drill Drones D1-Olen Overview of the measurement results,” Mol, Sep. 2021. [Online]. Available: www.sckcen.be

[52] H. Katreiner, Á. Horváth, F. Vörös, and M. Pál, “MAPPING GAMMA DOSE RATES OF AN AREA WITH ELEVATED NATURAL RADIOACTIVITY USING A DRONE-MOUNTED SAFECAST SENSOR,” 2022. [Online]. Available: https://www.researchgate.net/publication/362904013

[53] G. F. Knoll, *Radiation Detection and Measurement*, 4th ed. Wiley, 2010.

[54] A. N. Otte and D. Garcia, “A very brief review of recent SiPM developments PoS(PhotoDet2015)001,” 2015. [Online]. Available: http://pos.sissa.it/

[55] S. Gundacker and A. Heering, “The silicon photomultiplier: Fundamentals and applications of a modern solid-state photon detector,” Sep. 07, 2020, *Institute of Physics Publishing*. doi: 10.1088/1361-6560/ab7b2d.

[56] M. Grodzicka-Kobylka, T. Szczesniak, M. Moszyński, L. Swiderski, and M. Szawłowski, “Silicon photomultipliers in scintillation detectors used for gamma ray energies up to 6.1 MeV,” *Nucl. Instrum. Methods Phys. Res. A*, vol. 874, Dec. 2017, doi: 10.1016/j.nima.2017.08.031.

[57] S. Piatek, “Silicon Photomultiplier: Operation, Performance & Possible Applications,” 2018.

[58] S. J. Bell, P. Aitken-Smith, S. Beeke, S. M. Collins, P. H. Regan, and R. Shearman, “A comparison of emerging gamma detector technologies for airborne radiation monitoring,” in *Journal of Physics: Conference Series*, Institute of Physics Publishing, Oct. 2016. doi: 10.1088/1742-6596/763/1/012010.

[59] A. Vargas *et al.*, “Comparison of airborne radiation detectors carried by rotary-wing unmanned aerial systems,” *Radiat. Meas.*, vol. 145, Jul. 2021, doi: 10.1016/j.radmeas.2021.106595.

[60] M. Lowdon *et al.*, “Evaluation of scintillator detection materials for application within airborne environmental radiation monitoring,” *Sensors (Switzerland)*, vol. 19, no. 18, Sep. 2019, doi: 10.3390/s19183828.

[61] “Laboratoire National Henri Becquerel: Lara on the web.” Accessed: Mar. 28, 2024. [Online]. Available: http://www.nucleide.org/Laraweb/index.php

[62] IAEA, “IAEA Nuclidechart.” Accessed: Jan. 13, 2025. [Online]. Available: https://www-nds.iaea.org/relnsd/vcharthtml/VChartHTML.html

[63] J. S. Duval, B. Cook, and J. A. S. Adams, “Circle of investigation of an air-borne gamma-ray spectrometer,” *J. Geophys. Res.*, vol. 76, no. 35, pp. 8466–8470, Dec. 1971, doi: 10.1029/jb076i035p08466.

[64] J. A. Pitkin and J. S. Duvai, “Design parameters for aerial gamma-ray surveys,” 1980. [Online]. Available: http://library.seg.org/

[65] H. L. Beck, J. Decampo, and C. Gogolak, “IN SITU Ge(Li) AND Nal(Tl) GAMMA-RAY SPECTROMETRY,” New York, Sep. 1972.

[66] IAEA, *Guidelines for radioelement mapping using gamma ray spectrometry data (IAEA-TECDOC-1363)*. Vienna: International Atomic Energy Agency, 2003.

[67] IAEA, “IAEA TECDOC 1092: Generic procedures for monitoring in a nuclear or radiological emergency,” Vienna, Jun. 1999.

[68] A. Ishizaki, Y. Sanada, M. Ishida, and M. Munakata, “Application of topographical source model for air dose rates conversions in aerial radiation monitoring,” *J. Environ. Radioact.*, vol. 180, pp. 82–89, Dec. 2017, doi: 10.1016/j.jenvrad.2017.09.028.

[69] G. W. Phillips, “Gamma-ray imaging with Compton cameras,” 1995.

[70] C. M. Chen, L. E. Sinclair, R. Fortin, M. Coyle, and C. Samson, “In-flight performance of the Advanced Radiation Detector for UAV Operations (ARDUO),” Feb. 21, 2020, *Elsevier B.V.* doi: 10.1016/j.nima.2018.11.068.

[71] J. P. Carr *et al.*, “RPAS Plume Measurements for Reconstructing Radiological Source Terms,” Nov. 2025. doi: 10.1016/j.jenvrad.2025.107811.

[72] N. Schemm, S. Balkir, M. W. Hoffman, and M. Bauer, “A directional gamma ray detector using a single chip computational sensor,” in *Proceedings of IEEE Sensors*, 2011, pp. 1760–1763. doi: 10.1109/ICSENS.2011.6127024.

[73] M. J. Willis, S. E. Skutnik, and H. L. Hall, “Detection and positioning of radioactive sources using a four-detector response algorithm,” *Nucl. Instrum. Methods Phys. Res. A*, vol. 767, pp. 445–452, Dec. 2014, doi: 10.1016/j.nima.2014.08.033.

[74] J. C. Curtis *et al.*, “Simulation and validation of the Mobile Urban Radiation Search (MURS) gamma-ray detector response,” Feb. 21, 2020, *Elsevier B.V.* doi: 10.1016/j.nima.2018.08.087.

[75] F. Salvat and J. M. Fernández-Varea, “Overview of physical interaction models for photon and electron transport used in Monte Carlo codes,” *Metrologia*, vol. 46, no. 2, 2009, doi: 10.1088/0026-1394/46/2/S08.

[76] F. Salvat, *PENELOPE-2014: A Code System for Monte Carlo Simulation of Electron and Photon Transport*. Barcelona: NEA/OECD, 2014. [Online]. Available: www.oecd-nea.org

[77] J. Sempau, J. M. Fernández-Varea, E. Acosta, and F. Salvat, “Experimental benchmarks of the Monte Carlo code PENELOPE,” *Nucl. Instrum. Methods Phys. Res. B*, vol. 207, no. 2, pp. 107–123, Jun. 2003, doi: 10.1016/S0168-583X(03)00453-1.

[78] J. Baro, J. Sempau, J. M. Ferntidez-Varea, and F. Salvat, “PENELOPE: An algorithm for Monte Carlo simulation of the penetration and energy loss of electrons and positrons in matter,” *Nuclear Instruments and Methods in Physics Research B*, vol. 100, pp. 31–46, 1995.

[79] A. Steurer, A. Leitner, and F. J. Maringer, “DIFFERENT VALUES FOR DOSE RATE CONSTANTS IN RADIATION PROTECTION LITERATURE-REASONS AND CONSEQUENCES IN PRACTICE.”

[80] S. Geelen, J. Camps, G. Olyslaegers, and W. Schroeyers, “Drone-borne dosimetry in a radiological or nuclear scenario,” *Radiat. Meas.*, vol. 170, Jan. 2024, doi: 10.1016/j.radmeas.2023.107042.

[81] J. Paridaens, “Radiation Detection & Transmission In Flight : RadDetecTIF Experimental autonomous CsI radiation detector based setup for use on small rotary unmanned aerial vehicles,” Mol, Apr. 2020. [Online]. Available: www.sckcen.be

[82] D. H. Stolfi, M. R. Brust, G. Danoy, and P. Bouvry, “CONSOLE: intruder detection using a UAV swarm and security rings,” *Swarm Intelligence*, vol. 15, no. 3, pp. 205–235, Sep. 2021, doi: 10.1007/s11721-021-00193-7.

[83] S. Chowdhury, A. Emelogu, M. Marufuzzaman, S. G. Nurre, and L. Bian, “Drones for disaster response and relief operations: A continuous approximation model,” *Int. J. Prod. Econ.*, vol. 188, Jun. 2017, doi: 10.1016/j.ijpe.2017.03.024.

[84] S. Geelen, J. Camps, G. Olyslaegers, G. Ilegems, and W. Schroeyers, “Radiological Surveillance Using a Fixed-Wing UAV Platform,” *Remote Sens. (Basel).*, vol. 14, no. 16, Aug. 2022, doi: 10.3390/rs14163908.

[85] P. Royo, E. Pastor, M. Macias, R. Cuadrado, C. Barrado, and A. Vargas, “An Unmanned Aircraft System to detect a radiological point source using RIMA software architecture,” *Remote Sens. (Basel).*, vol. 10, no. 11, Nov. 2018, doi: 10.3390/rs10111712.

[86] S. Zhang, R. Liu, and T. Zhao, “Mapping radiation distribution on ground based on the measurement using an unmanned aerial vehicle,” *J. Environ. Radioact.*, vol. 193–194, Oct. 2018, doi: 10.1016/j.jenvrad.2018.08.016.

[87] Y. Sanada, T. Orita, and T. Torii, “Temporal variation of dose rate distribution around the Fukushima Daiichi nuclear power station using unmanned helicopter,” *Applied Radiation and Isotopes*, vol. 118, pp. 308–316, Dec. 2016, doi: 10.1016/j.apradiso.2016.09.008.

[88] Y. Shikaze *et al.*, “Field test around Fukushima Daiichi nuclear power plant site using improved Ce:Gd3(Al,Ga)5O12 scintillator Compton camera mounted on an unmanned helicopter,” *J. Nucl. Sci. Technol.*, vol. 53, no. 12, Dec. 2016, doi: 10.1080/00223131.2016.1185980.

[89] A. Varley, A. Tyler, Y. Bondar, A. Hosseini, V. Zabrotski, and M. Dowdall, “Reconstructing the deposition environment and long-term fate of Chernobyl 137Cs at the floodplain scale through mobile gamma spectrometry,” *Environmental Pollution*, vol. 240, Sep. 2018, doi: 10.1016/j.envpol.2018.04.112.

[90] H. Al Kanti, O. El Hajjaji, T. El Bardouni, H. Boukhal, and M. Mohammed, “Conversion coefficients calculation of mono-energetic photons from air-kerma using Monte Carlo and analytical methods,” *J. King Saud Univ. Sci.*, vol. 32, no. 1, pp. 288–293, Jan. 2020, doi: 10.1016/j.jksus.2018.05.007.

[91] P. G. Martin, O. D. Payton, J. S. Fardoulis, D. A. Richards, and T. B. Scott, “The use of unmanned aerial systems for the mapping of legacy uranium mines,” *J. Environ. Radioact.*, vol. 143, pp. 135–140, May 2015, doi: 10.1016/j.jenvrad.2015.02.004.

[92] P. Gabrlik and T. Lazna, “Simulation of Gamma Radiation Mapping Using an Unmanned Aerial System,” Elsevier B.V., 2018, pp. 256–262. doi: 10.1016/j.ifacol.2018.07.163.

[93] DJI, “DJI M600 Pro.” Accessed: Jun. 30, 2024. [Online]. Available: https://www.dji.com/be/support/product/matrice600

[94] “DJI MATRICE 600 Release Notes,” Apr. 2019. [Online]. Available: http://www.dji.com/matrice600

[95] E. Cottens *et al.*, “Onderzoek naar de verspreiding van Radium-226 in het leefmilieu te Sint-Jozef-Olen en omgeving en de daaruit voortvloeiende dosisbelasting voor de bevolking.,” Mol, 1995.

[96] H. Vanmarcke, “Sanering van de Omgevingsbesmetting met Radium-226 te Olen en Geel.,” Mol, Jun. 1997.

[97] J. G. Proakis and D. G. Manolakis, *DIGITAL SIGNAL PROCESSING Principles, Algorithms and Applications*, 3rd ed. New Jersey: Prentice-Hall International, Inc., 1996.

[98] “Geopunt Vlaanderen.” Accessed: May 01, 2024. [Online]. Available: https://www.geopunt.be/

[99] S. D. Billings, B. R. Minty, and G. N. Newsam, “Deconvolution and spatial resolution of airborne gamma-ray surveys,” *Geophysics*, vol. 68, no. 4, pp. 1257–1266, Aug. 2003, doi: 10.1190/1.598118.

[100] B. Minty and R. Brodie, “The 3D inversion of airborne gamma-ray spectrometric data,” Perth, Feb. 2015, pp. 1–4. [Online]. Available: http://www.mcs.anl.gov/petsc.

[101] “PenguinC_Datasheet,” Oregon.

[102] Collins Aerospace, “Piccolo flight management software.” Accessed: Jul. 01, 2024. [Online]. Available: https://www.collinsaerospace.com/what-we-do/industries/military-and-defense/avionics/autopilot/piccolo-flight-management-systems

[103] J. Kim *et al.*, “Efficient design of a Ø2×2 inch NaI(Tl)scintillation detector coupled with a SiPM in an aquatic environment,” *Nuclear Engineering and Technology*, vol. 51, no. 4, Jul. 2019, doi: 10.1016/j.net.2019.01.017.

[104] A. Ghassemi, K. Sato, and K. Kobayashi, “MPPC,” Mar. 2017.

[105] Scionix, “Can Silicon Photomultipliers replace vacuum PMTs? A practical approach.”

[106] “BrightSpec Software Development Kit SDK Reference Manual,” Niel, Sep. 2017.

[107] “TOPAZ-SiPM-a miniature digital MCA,” Niel, Jan. 2020.

[108] Zubax Robotics, “Zubax GNSS Datasheet,” Tallinn, Jan. 2019. [Online]. Available: https://device.zubax.com/device_info.

[109] J.-P. Laedermann, F. Byrde, and C. Murith, “In-Situ Gamma-ray Spectrometry: the Influence of Topography on the Accuracy of Activity Determination,” *Journal off Environmental Radioactivity*, vol. 38, no. 1, pp. 1–16, 1998.

[110] “Droneport.” Accessed: Jul. 01, 2024. [Online]. Available: https://droneport.eu/

[111] FANC, “Verslagen van het radiologisch toezicht België.” Accessed: May 28, 2025. [Online]. Available: https://fanc.fgov.be/nl/publicaties/verslagen-van-het-radiologisch-toezicht-belgie

[112] World Nuclear association, “Fukushima accident.” Accessed: Jul. 01, 2024. [Online]. Available: https://world-nuclear.org/information-library/safety-and-security/safety-of-plants/fukushima-daiichi-accident

[113] FANC, “NINTH MEETING OF THE CONTRACTING PARTIES TO THE CONVENTION ON NUCLEAR SAFETY,” Aug. 2022.

[114] C. Rojas-Palma *et al.*, “Experimental evaluation of gamma fluence-rate predictions from argon-41 releases to the atmosphere over a nuclear research reactor site,” *Radiat. Prot. Dosimetry*, vol. 108, no. 2, 2004, doi: 10.1093/rpd/nch020.

[115] FANC, “The TELERAD network: continuous radiological monitoring of the territory,” 2020.

[116] J. P. K. W. Frankemölle *et al.*, “Near-range atmospheric dispersion of an anomalous selenium-75 emission,” *J. Environ. Radioact.*, vol. 255, Dec. 2022, doi: 10.1016/j.jenvrad.2022.107012.

[117] J. P. Frankemölle, J. Camps, P. De Meutter, and J. Meyers, “Near-Range Gaussian Plume Modelling for Gamma Dose Rate Reconstruction,” Aveiro, Feb. 2023. [Online]. Available: https://geoportail.wallonie.be

[118] “Botlink XRD2 Datasheet,” Fargo, Mar. 2022. [Online]. Available: www.botlink.com/xrd2

[119] S. Mochizuki *et al.*, “First demonstration of aerial gamma-ray imaging using drone for prompt radiation survey in Fukushima,” *Journal of Instrumentation*, vol. 12, no. 11, Nov. 2017, doi: 10.1088/1748-0221/12/11/P11014.

[120] “National Institute of Standards and Technology.” Accessed: May 01, 2024. [Online]. Available: https://www.nist.gov/

8 Annex

8.1 Curve Fit of the Cs-137 Point Source Measurements

Table 12: X-shift (m) retrieved from the curve fit of the Cs-137 point source using Equation 2. The columns represent the different speeds and the rows the different AGL heights.

X-shift (m)	1 m/s	2 m/s	5 m/s
2 m	-1.8 (0.2)	-1.6 (0.3)	-4.7 (0.9)
5 m	-1.6 (0.6)	-5.3 (0.6)	-4.7 (1.3)
10 m	1.0 (6.4)	-1.1 (7.8)	10.0 (4.4)

Table 13: Y-shift (m) retrieved from the curve fit of the Cs-137 point source using Equation 2. The columns represent the different speeds and the rows the different AGL heights.

Y-shift (m)	1 m/s	2 m/s	5 m/s
2 m	0.8 (0.1)	2.6 (0.2)	5.3 (0.6)
5 m	0.7 (0.2)	3.1 (0.4)	6.9 (0.7)
10 m	0.7 (1.5)	-2.3 (2.0)	-2.6 (2.0)

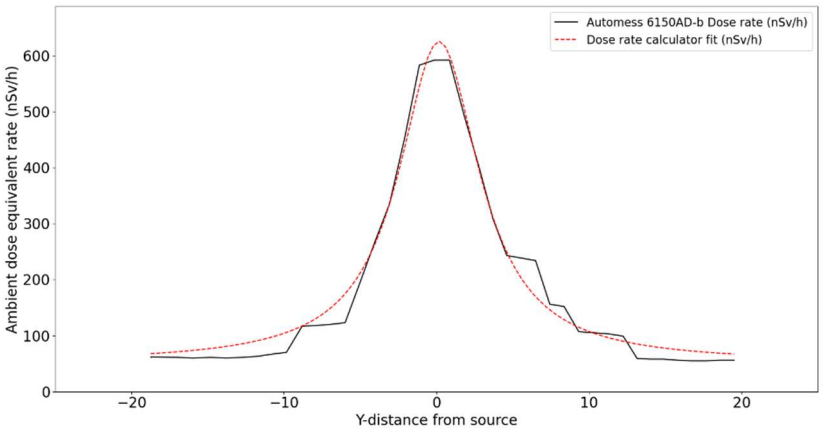

Figure 69: Single flight line of the Cs-137 point source measurement at 1 m/s at 2 m AGL height. The red dotted line represents the curve fit using Equation 2. (R^2 = 0.98)

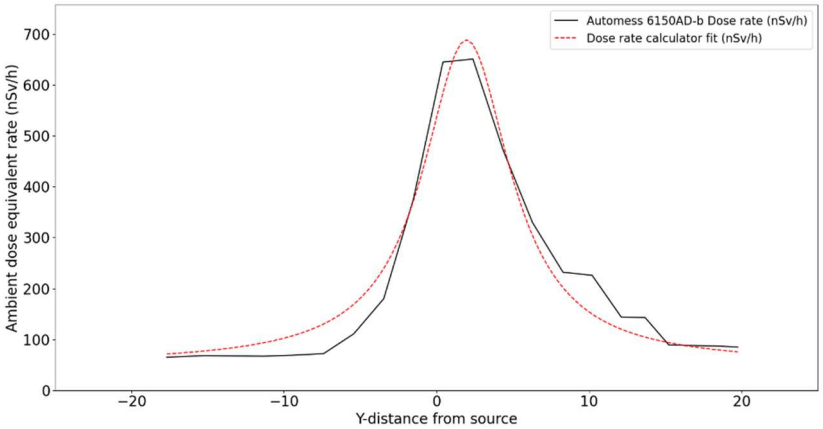

Figure 70: Single flight line of the Cs-137 point source measurement at 2 m/s at 2 m AGL height. The red dotted line represents the curve fit using Equation 2. (R^2 = 0.96)

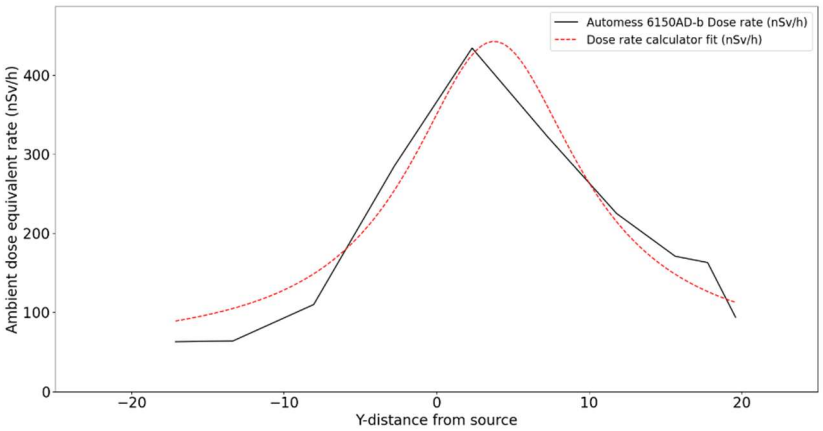

Figure 71: Single flight line of the Cs-137 point source measurement at 5 m/s at 2 m AGL height. The red dotted line represents the curve fit using Equation 2. (R^2 = 0.94)

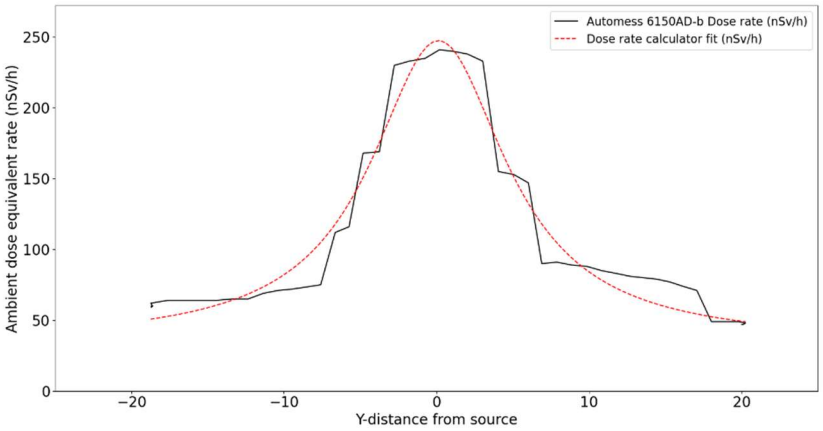

Figure 72: Single flight line of the Cs-137 point source measurement at 1 m/s at 5 m AGL height. The red dotted line represents the curve fit using Equation 2. (R^2 = 0.96)

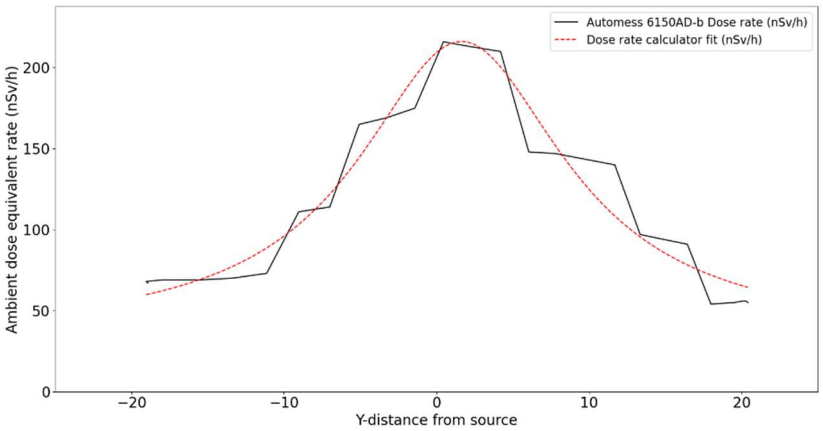

Figure 73: Single flight line of the Cs-137 point source measurement at 2 m/s at 5 m AGL height. The red dotted line represents the curve fit using Equation 2. (R^2 = 0.94)

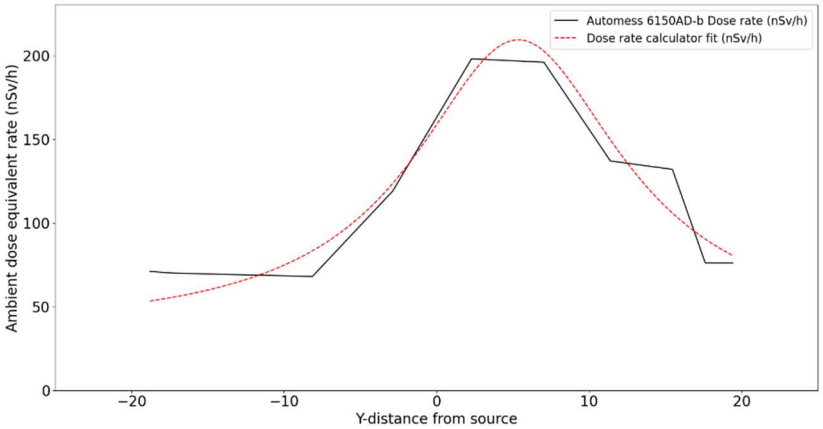

Figure 74: Single flight line of the Cs-137 point source measurement at 5 m/s at 5 m AGL height. The red dotted line represents the curve fit using Equation 2. (R^2 = 0.92)

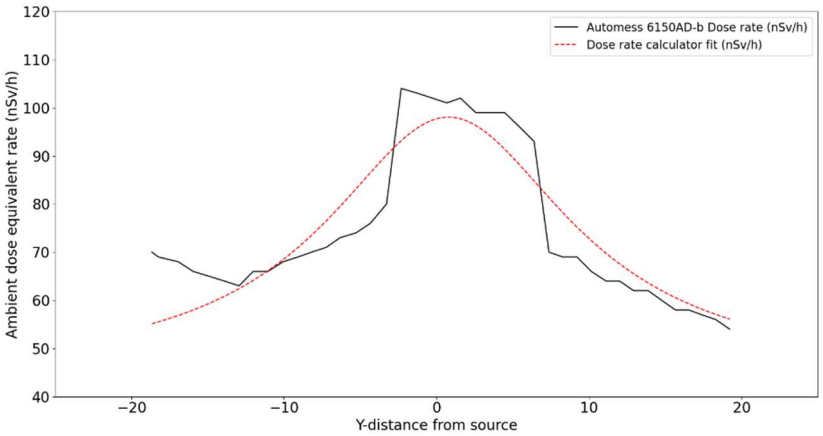

Figure 75: Single flight line of the Cs-137 point source measurement at 1 m/s at 10 m AGL height. The red dotted line represents the curve fit using Equation 2. (R^2 = 0.80)

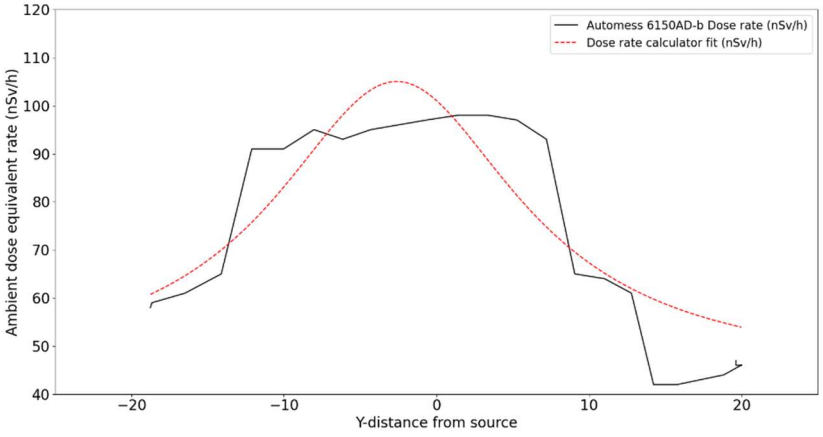

Figure 76: Single flight line of the Cs-137 point source measurement at 2 m/s at 10 m AGL height. The red dotted line represents the curve fit using Equation 2. (R^2 = 0.81)

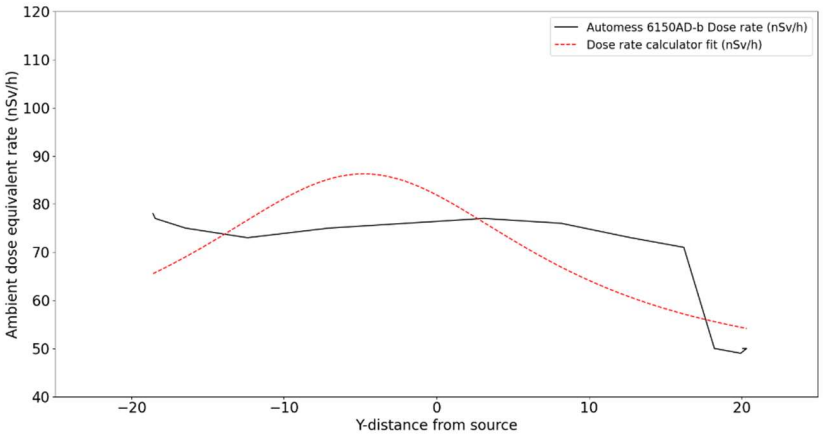

Figure 77: Single flight line of the Cs-137 point source measurement at 5 m/s at 10 m AGL height. The red dotted line represents the curve fit using Equation 2. (R^2 = 0.50)

8.2 Frequency Plots D1 Site

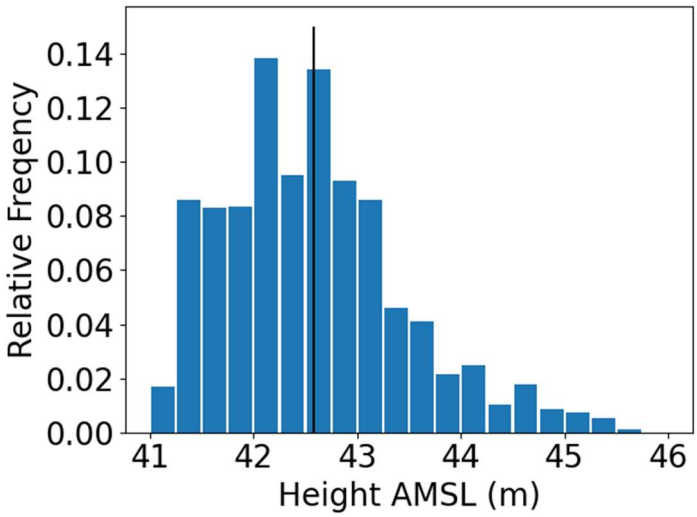

Figure 78: Histogram of the AMSL height from the D1 flights done with the AD6510-b detector. The black line shows the average at 42.6 m. The terrain has an AMSL height of roughly 17 m making the AGL height of the drone approximately 25 m. The data is coming from the flightpaths above the D1 site.

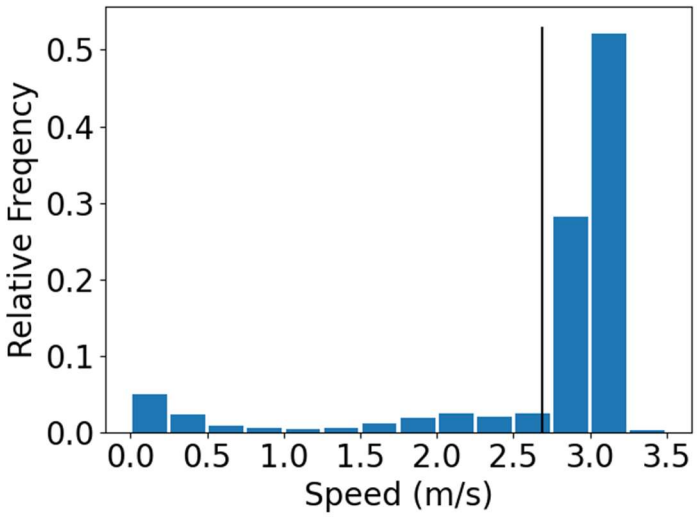

Figure 79: Histogram of the flight speed from the D1 flights done with the AD6510-b detector. The black line shows the average at 2.7 m/s. The data is coming from the flightpaths above the D1 site.

8.3 Fixed-wing Detector System by Car

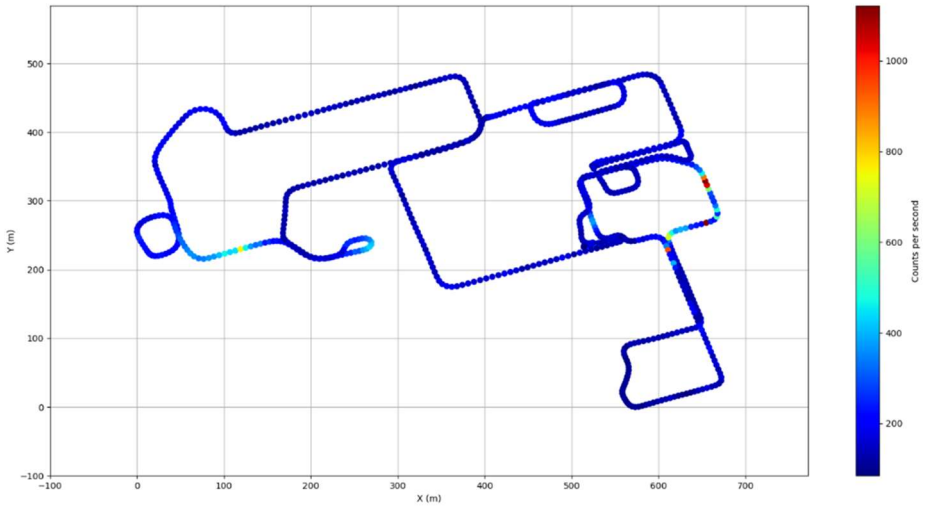

Figure 80: Counts per second measured while driving around a nuclear site using the fixed-wing detector system standing upright facing the passenger door.

8.4 Sources

Table 14: List of the sources that were used in this thesis. All data comes from 'Lara on the web' [61] and the gamma energies are cut off at an intensity of 5% for clarity.

Nuclide	**Decay-type**	**Half-life**	**Main gamma energies (keV) (intensity (%))**
Na-22	Beta-plus	2.6 y	511 (180.7), 1274.5 (99.9)
Ar-41	Beta-min	1.8 h	1293.6 (99.2)
Co-60	Beta-min	5.3 y	1173.2 (99.9), 1332.5 (100)
Cs-137	Beta-min	30.0 y	661.7 (85.0)
Eu-152	Beta-min (27.9%) Beta-plus (72.1%)	13.5 y	6.4 (13.0), 39.5 (20.8), 40.1 (37.7), 45.5 (11.8), 121.8 (28.4), 244.7 (7.6), 344.3 (26.6), 778.9 (13.0), 964.1 (14.5), 1085.8 (10.1), 1112.1 (13.4), 1408.0 (20.9)
K-40	Beta-min (89.2%) Beta-plus (10.8%)	1.23E+9 y	1460.8 (10.55)
Ra-226 (gammas from Pb-214 and Bi-214)	Alpha (Ra-226) Beta-min (Pb-214) Beta-min (Bi-214)	1.6E+3 y 26.9 min 19.8 min	242.0 (7.3), 295.2 (18.4), 351.9 (35.6), 609.3 (45.5), 1120.3 (14.9), 1238.1 (5.8), 1764.5 (15.3)

8.4.1 Radium-226

Radium-226 decays through alpha decay and creates a decay chain as shown in Figure 75. In its decay scheme there are no significant (intensity above 5 %) gamma rays. However, two of its daughters Pb-214 and Bi-214 both have several gamma ray emissions. The energies and intensities of these gamma rays can be found in Table 11. The first daughter of Ra-226 is Rn-222, a radioactive noble gas. This information is important since the gas itself can easily escape from most enclosures and might cause problems when defining source geometries [95], [96].

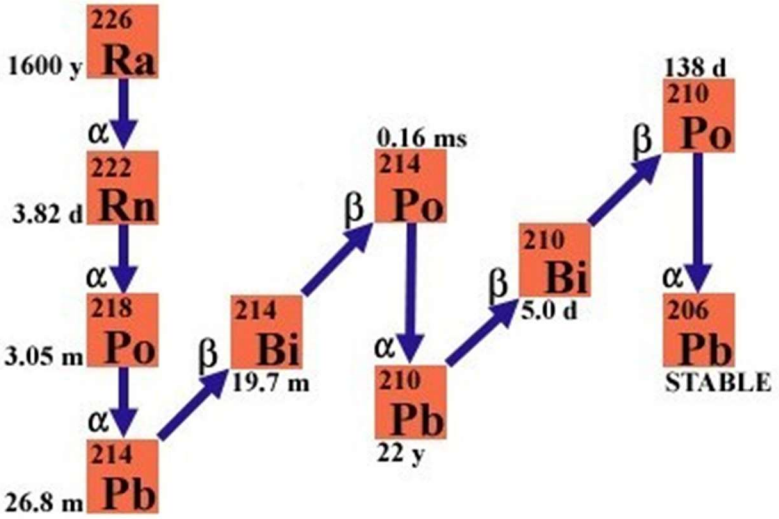

Figure 81: Radium-226 decay chain taken from the National Institute of Standards and Technology [120]. Figure 82: Radium-226 decay chain taken from the National Institute of Standards and Technology [120].

8.5 Aerial Concentration Measurement Equation

Figure 76 shows a drawing of the situation when a part of a soil contamination is measured by a detector at an AGL height of h. The part of the soil is located at a depth z and a direct distance r. The angle between the height normal to the soil and the direct distance is called θ. The following steps will explain how we can retrieve the fluence rate φ of the soil contamination using the basic fluence rate formula. Firstly, we use the fluence rate formula. It is situated in a Cartesian coordinate system with x, y and z. The first term represents the source activity S_0 divided by $4\pi r^2$ due to the influence of the inverse-square law. The next term is due to the exponentially distributed soil in function of its depth. With α being the reciprocal of the relaxation length of the assumed exponentially distributed source activity with depth, expressed in cm^{-1}. ρ stands for the soil density in g/cm^3. The third term is for the self-absorption of the soil with μ_s as the attenuation coefficient for soil and ω as the cos(θ). The fourth term is needed for the attenuation due to the air with μ_a as the attenuation coefficient for air.

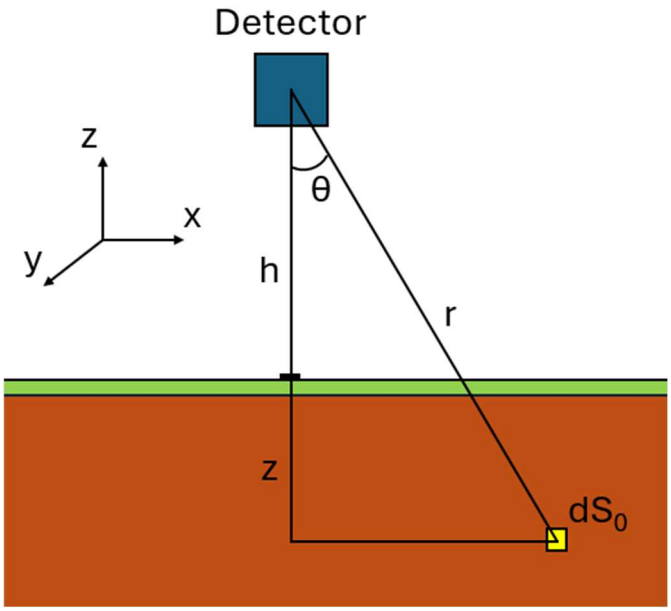

Figure 83: Schematic of a detector measuring a part dS_0 from a contaminated soil.

$$\varphi(x,y,z) = \int_0^{\infty}\int_0^{\infty}\int_{-\infty}^{h/\omega} \frac{S_0}{4\pi r^2}\left[-\left(\frac{\alpha}{\rho}\right)\rho z\right] exp\, exp\left[-\mu_s \frac{z}{\omega}\right] exp\, exp\left[-\mu_a \frac{h}{\omega}\right] dxdydz$$

The first step in deriving the fluence rate from the formula above is converting the cartesian coordinates in polar coordinates using $dxdydz = r^2.sin\ sin\ \theta\ drd\theta d\varphi$. To remove our z dependency we also converted z using $z = \omega(r - \frac{h}{\omega})$.

$$\varphi(r,\theta,\varphi) = \int_0^{2\pi}\int_0^{\pi/2}\int_{h/\omega}^{\infty} \frac{S_0}{4\pi r^2}\left[-\left(\frac{\alpha}{\rho}\right)\omega(r-\frac{h}{\omega})\right] exp\ exp\ \left[-\mu_s(r-\frac{h}{\omega})\right] exp\ exp\ \left[-\mu_a\frac{h}{\omega}\right]\ r^2 \\ sin\ sin\ \theta\ drd\theta d\varphi$$

The next step solves the dφ part of the integral resulting in an additional term of 2π.

$$\varphi(r,\theta) = 2\pi.\int_0^{\pi/2}\int_{h/\omega}^{\infty} \frac{S_0}{4\pi r^2}\left[-\left(\frac{\alpha}{\rho}\right)\rho\omega(r-\frac{h}{\omega})\right] exp\ exp\ \left[-\mu_s(r-\frac{h}{\omega})\right] \\ exp\ exp\ \left[-\mu_a\frac{h}{\omega}\right]\ r^2\ sin\ sin\ \theta\ drd\theta$$

The 2π and r² can be resolved with the 4πr² in the denominator.

$$\varphi(r,\theta) = \int_0^{\pi/2}\int_{h/\omega}^{\infty} \frac{S_0}{2}\left[-\left(\frac{\alpha}{\rho}\right)\rho\omega(r-\frac{h}{\omega}\right] exp\ exp\ \left[-\mu_s(r-\frac{h}{\omega})\right] \\ exp\ exp\ \left[-\mu_a\frac{h}{\omega}\right] sin\ sin\ \theta\ drd\theta$$

The next step substitutes r using a new definition r'= r-h/ω giving r= r'+h/ω.

$$\varphi(r,\theta) = \int_0^{\pi/2}\int_{h/\omega}^{\infty} \frac{S_0}{2}\left[-\left(\frac{\alpha}{\rho}\right)\rho r\omega\right] exp\ exp\ [-\mu_s r].exp\ exp\ \left[-\mu_a\frac{h}{\omega}\right] \\ sin\ sin\ \theta\ drd\theta$$

The following step uses the definition of ω=cos(θ) meaning that:

dω/dθ= -sin(θ) or dω= -sin(θ).dθ

The latter is substituted and the integral limits are adapted to their respective new values.

$$\varphi(r,\theta) = -\int_1^0\int_0^{\infty} \frac{S_0}{2}\left[-\frac{\alpha}{\rho}\rho\omega r - \mu_s r\right] exp\ exp\ \left[-\mu_a\frac{h}{\omega}\right] drd\omega$$

The minus symbol is used to inverse the first integral.

$$\varphi(r,\theta) = \int_0^1 \int_0^\infty \frac{S_0}{2}\left[-\left(\frac{\alpha}{\rho}\rho\omega + \mu_s\right)r\right] exp\, exp\left[-\mu_a \frac{h}{\omega}\right] dr d\omega$$

Integrating over r gives us the final formula.

$$\varphi(\theta) = \int_0^1 \frac{S_0}{2}\frac{1}{\frac{\alpha}{\rho}\rho\omega + \mu_s}\left[-\mu_a \frac{h}{\omega}\right] d\omega$$

www.uhasselt.be
Hasselt University
Martelarenlaan 42 | BE-3500 Hasselt